

## Commercializable Power Source from Forming New States of Hydrogen

R. L. Mills, G. Zhao, K. Akhtar, Z. Chang, J. He, Y. Lu, W. Good, G. Chu  
BlackLight Power, Inc., 493 Old Trenton Road, Cranbury, NJ 08512

### ABSTRACT

The data from a broad spectrum of investigational techniques strongly and consistently indicates that hydrogen can exist in lower-energy states than previously thought possible. The predicted reaction involves a resonant, nonradiative energy transfer from otherwise stable atomic hydrogen to a catalyst capable of accepting the energy. The product is  $H(1/p)$ , fractional Rydberg states of atomic hydrogen called “hydrino atoms” wherein  $n = \frac{1}{2}, \frac{1}{3}, \frac{1}{4}, \dots, \frac{1}{p}$  ( $p \leq 137$  is an integer) replaces the well-known parameter  $n = \text{integer}$  in the Rydberg equation for hydrogen excited states. Atomic lithium and molecular  $NaH$  served as catalysts since they meet the catalyst criterion—a chemical or physical process with an enthalpy change equal to an integer multiple  $m$  of the potential energy of atomic hydrogen, 27.2 eV (e.g.  $m = 3$  for  $Li$  and  $m = 2$  for  $NaH$ ). Specific predictions based on closed-form equations for energy levels of the corresponding hydrino hydride ions  $H^-(1/4)$  of novel alkali halido hydrino hydride compounds ( $MH * X$ ;  $M = Li \text{ or } Na, X = \text{halide}$ ) and molecular hydrino  $H_2(1/4)$  were tested using chemically generated catalysis reactants.

First,  $Li$  catalyst was tested.  $Li$  and  $LiNH_2$  were used as a source of atomic lithium and hydrogen atoms. Using water-flow, batch calorimetry, the measured power from 1g  $Li$ , 0.5g  $LiNH_2$ , 10g  $LiBr$ , and 15g  $Pd/Al_2O_3$  was about 160W with an energy balance of  $\Delta H = -19.1 \text{ kJ}$ . The observed energy balance was 4.4 times the maximum theoretical energy based on known chemistry. Next, Raney nickel (R-Ni) served as a dissociator when the power reaction mixture was used in chemical synthesis wherein  $LiBr$  acted as a getter of the catalysis product  $H(1/4)$  to form  $LiH * X$  as well as to trap  $H_2(1/4)$  in the crystal. The ToF-SIMS showed  $LiH * X$  peaks. The  $^1H$  MAS NMR  $LiH * Br$  and  $LiH * I$  showed a large distinct upfield resonance at about -2.5 ppm that matched  $H^-(1/4)$  in a  $LiX$  matrix. An NMR peak at 1.13 ppm matched interstitial  $H_2(1/4)$ , and the rotation frequency of  $H_2(1/4)$  of  $4^2$  times that of ordinary  $H_2$  was observed at  $1989 \text{ cm}^{-1}$  in the FTIR spectrum. The XPS spectrum recorded on the  $LiH * Br$  crystals showed peaks at about 9.5 eV and 12.3 eV that could not be assigned to any known elements based on the absence of any other primary element peaks, but matched the binding energy of  $H^-(1/4)$  in two chemical environments. A further signature of the energetic process was the observation of the formation of a plasma called a resonant transfer- or rt-plasma at low temperatures (e.g.  $\approx 10^3 \text{ K}$ ) and very low field strengths of about 1-2 V/cm when atomic  $Li$  was present with atomic hydrogen. Time-dependent line broadening of the H Balmer  $\alpha$  line was observed corresponding to extraordinarily fast H (>40 eV).

$NaH$  uniquely achieves high kinetics since the catalyst reaction relies on the release of the intrinsic  $H$ , which concomitantly undergoes the transition to form  $H(1/3)$  that further

reacts to form  $H(1/4)$ . High-temperature differential scanning calorimetry (DSC) was performed on ionic  $NaH$  under a helium atmosphere at an extremely slow temperature ramp rate ( $0.1^\circ\text{C}/\text{min}$ ) to increase the amount of molecular  $NaH$  formation. A novel exothermic effect of  $-177 \text{ kJ}/\text{moleNaH}$  was observed in the temperature range of  $640^\circ\text{C}$  to  $825^\circ\text{C}$ . To achieve high power, R-Ni having a surface area of about  $100 \text{ m}^2/\text{g}$  was surface-coated with  $NaOH$  and reacted with  $Na$  metal to form  $NaH$ . Using water-flow, batch calorimetry, the measured power from 15g of R-Ni was about 0.5 kW with an energy balance of  $\Delta H = -36 \text{ kJ}$  compared to  $\Delta H \approx 0 \text{ kJ}$  from the R-Ni starting material, R-NiAl alloy, when reacted with  $Na$  metal. The observed energy balance of the  $NaH$  reaction was  $-1.6 \times 10^4 \text{ kJ}/\text{mole } H_2$ , over 66 times the  $-241.8 \text{ kJ}/\text{mole } H_2$  enthalpy of combustion. With an increase in  $NaOH$  doping to 0.5 wt%, the  $Al$  of the R-Ni intermetallic served to replace  $Na$  metal as a reductant to generate the  $NaH$  catalyst. When heated to  $60^\circ\text{C}$ , 15g of the composite catalyst material required no additive to release 11.7 kJ of excess energy and develop a power of 0.25 kW. The energy scaled linearly and the power increased nonlinearly wherein the reaction of 1 kg 0.5 wt%  $NaOH$ -doped R-Ni liberated 753.1 kJ of energy to develop a power in excess of 50 kW. Solution NMR on product gases dissolved in DMF-d7 showed  $H_2(1/4)$  at 1.2 ppm.

The ToF-SIMS showed sodium hydrido hydride,  $NaH_x$ , peaks. The  $^1H$  MAS NMR spectra of  $NaH * Br$  and  $NaH * Cl$  showed large distinct upfield resonance at  $-3.6$  ppm and  $-4$  ppm, respectively, that matched  $H^-(1/4)$ , and an NMR peak at 1.1 ppm matched  $H_2(1/4)$ .  $NaH * Cl$  from reaction of  $NaCl$  and the solid acid  $KHSO_4$  as the only source of hydrogen comprised two fractional hydrogen states. The  $H^-(1/4)$  NMR peak was observed at  $-3.97$  ppm, and the  $H^-(1/3)$  peak was also present at  $-3.15$  ppm. The corresponding  $H_2(1/4)$  and  $H_2(1/3)$  peaks were observed at 1.15 ppm and 1.7 ppm, respectively.  $^1H$  NMR of  $NaH * F$  dissolved in DMF-d7 showed isolated  $H_2(1/4)$  and  $H^-(1/4)$  at 1.2 ppm and  $-3.86$  ppm, respectively, wherein the absence of any solid matrix effect or the possibility of alternative assignments confirmed the solid NMR assignments. The XPS spectrum recorded on  $NaH * Br$  showed the  $H^-(1/4)$  peaks at about 9.5 eV and 12.3 eV that matched the results from  $LiH * Br$  and  $KH * I$ ; whereas, sodium hydrido hydride showed two fractional hydrogen states additionally having the  $H^-(1/3)$  XPS peak at 6 eV in the absence of a halide peak. The predicted rotational transitions having energies of  $4^2$  times those of ordinary  $H_2$  were also observed from  $H_2(1/4)$  which was excited using a 12.5 keV electron beam.

Keywords: fractional-principal-quantum-level hydride ion and molecular hydrogen, XPS, NMR, ToF-SIMS, vibration-rotational spectroscopy, exothermic catalysis reaction

## I. Introduction

Mills [1-12] solved the structure of the bound electron using classical laws and subsequently developed a unification theory based on those laws called the Grand Unified Theory of Classical Physics (GUTCP) with results that match observations for the basic phenomena of physics and chemistry from the scale of the quarks to cosmos. This paper is the first in a series of three that covers two specific predictions of GUTCP, two involving the existence of lower-energy states of the hydrogen atom, which represents a powerful new energy source, and the third involving the existence of a fifth force [2] beyond the electromagnetic, strong and weak-nuclear, and gravitational forces.

GUTCP predicts a reaction involving a resonant, nonradiative energy transfer from otherwise stable atomic hydrogen to a catalyst capable of accepting the energy to form hydrogen in lower-energy states than previously thought possible. Specifically, the product is  $H(1/p)$ ,

fractional Rydberg states of atomic hydrogen wherein  $n = \frac{1}{2}, \frac{1}{3}, \frac{1}{4}, \dots, \frac{1}{p}$  ( $p \leq 137$  is an integer)

replaces the well known parameter  $n = \text{integer}$  in the Rydberg equation for hydrogen excited states.  $He^+$ ,  $Ar^+$ ,  $Sr^+$ ,  $Li$ ,  $K$ , and  $NaH$  are predicted to serve as catalysts since they meet the catalyst criterion—a chemical or physical process with an enthalpy change equal to an integer multiple of the potential energy of atomic hydrogen,  $27.2 \text{ eV}$ . The data from a broad spectrum of investigational techniques strongly and consistently support the existence of these states called hydrino, for “small hydrogen,” and the corresponding diatomic molecular hydrino. Some of these prior related studies supporting the possibility of a novel reaction of atomic hydrogen, which produces hydrogen in fractional quantum states that are at lower energies than the traditional “ground” ( $n = 1$ ) state, include extreme ultraviolet (EUV) spectroscopy, characteristic emission from catalysts and the hydride ion products, lower-energy hydrogen emission, chemically-formed plasmas, Balmer  $\alpha$  line broadening, population inversion of H lines, elevated electron temperature, anomalous plasma afterglow duration, power generation, and analysis of novel chemical compounds [13-40].

Recently, there has been the announcement of some unexpected astrophysical results that support the existence of hydrinos. In 1995, Mills published the GUTCP prediction [41] that the expansion of the universe was accelerating from the same equations that correctly predicted the mass of the top quark before it was measured. To the astonishment of cosmologists, this was confirmed by 2000. Mills made another prediction about the nature of dark matter based on GUTCP that may be close to being confirmed. Based on recent evidence, Bournaud et al. [42-43] suggest that dark matter is hydrogen in dense molecular form that somehow behaves differently in terms of being unobservable except by its gravitational effects. Theoretical models predict that dwarf galaxies formed from collisional debris of massive galaxies should be free of nonbaryonic dark matter. So, their gravity should tally with the stars and gas within them. By analyzing the observed gas kinematics of such recycled galaxies, Bournaud et al. [42-43] have measured the gravitational masses of a series of dwarf galaxies lying in a ring around a massive galaxy that has recently experienced a collision. Contrary to the predictions of Cold-Dark-Matter (CDM) theories, their results demonstrate that they contain a massive dark component amounting to about twice the visible matter. This baryonic dark matter is argued to be cold molecular hydrogen, but it is distinguished from ordinary molecular hydrogen in that it is not traced at all by traditional methods, such as emission of CO lines. These results match predictions of the dark matter being molecular hydrino.

Emission lines recorded on cold interstellar regions containing dark matter matched  $H(1/p)$ , fractional Rydberg states of atomic hydrogen given by Eqs. (2a) and (2c) [29]. Such emission lines with energies of  $q \cdot 13.6 \text{ eV}$ , where  $q = 1, 2, 3, 4, 6, 7, 8, 9, \text{ or } 11$  were also observed by extreme ultraviolet (EUV) spectroscopy recorded on microwave discharges of helium with 2% hydrogen [27-29].  $He^+$  fulfills the catalyst criterion—a chemical or physical process with an enthalpy change equal to an integer multiple of  $27.2 \text{ eV}$  since it ionizes at  $54.417 \text{ eV}$ , which is  $2 \cdot 27.2 \text{ eV}$ . The product of the catalysis reaction of  $He^+$ ,  $H(1/3)$ , may further serve as a catalyst to lead to transitions to other states  $H(1/p)$ . Characteristic EUV continua with a cutoff at 22.8 nm and 30.4 nm and extending to longer wavelengths were recently reported that also have implications for the resolution of many celestial mysteries such as the paradox of the identity of dark matter and the identity of the radiation source behind the observation that diffuse  $H\alpha$  emission is ubiquitous throughout the Galaxy and widespread sources of flux shortward of  $912 \text{ \AA}$  are required [44].

J. R. Rydberg showed that all of the spectral lines of atomic hydrogen were given by a completely empirical relationship:

$$1/\lambda = R \left( \frac{1}{n_f^2} - \frac{1}{n_i^2} \right) \quad (1)$$

where  $R = 109,677 \text{ cm}^{-1}$ ,  $n_f = 1, 2, 3, \dots$ ,  $n_i = 2, 3, 4, \dots$  and  $n_i > n_f$ . Bohr, Schrödinger, and Heisenberg, each developed a theory for atomic hydrogen that gave the energy levels in agreement with Rydberg's equation.

$$E_n = -\frac{e^2}{n^2 8\pi\epsilon_0 a_H} = -\frac{13.598 \text{ eV}}{n^2} \quad (2a)$$

$$n = 1, 2, 3, \dots \quad (2b)$$

where  $e$  is the elementary charge,  $\epsilon_0$  is the permittivity of vacuum, and  $a_H$  is the radius of the hydrogen atom. The excited energy states of atomic hydrogen are given by Eq. (2a) for  $n > 1$  in Eq. (2b). The  $n = 1$  state is the “ground” state for “pure” photon transitions (i.e. the  $n = 1$  state can absorb a photon and go to an excited electronic state, but it cannot release a photon and go to a lower-energy electronic state). However, an electron transition from the ground state to a lower-energy state may be possible by a resonant nonradiative energy transfer such as multipole coupling or a resonant collision mechanism. Processes such as hydrogen molecular bond formation that occur without photons and that require collisions are common [45]. Also, some commercial phosphors are based on resonant nonradiative energy transfer involving multipole coupling [46].

The theory reported previously [1, 13-40] predicts that atomic hydrogen may undergo a catalytic reaction with certain atoms, excimers, ions, and diatomic hydrides which provide a reaction with a net enthalpy of an integer multiple of the potential energy of atomic hydrogen,  $E_n = 27.2 \text{ eV}$  where  $E_n$  is one Hartree. Specific species (e.g.  $He^+$ ,  $Ar^+$ ,  $Sr^+$ ,  $K$ ,  $Li$ ,  $HCl$ , and  $NaH$ ) identifiable on the basis of their known electron energy levels are required to be present with atomic hydrogen to catalyze the process. The reaction involves a nonradiative energy transfer followed by  $q \cdot 13.6 \text{ eV}$  emission or  $q \cdot 13.6 \text{ eV}$  transfer to H to form extraordinarily hot, excited-state H [13-17, 19-20, 32-39] and a hydrogen atom that is lower in

energy than unreacted atomic hydrogen that corresponds to a fractional principal quantum number. That is

$$n = 1, \frac{1}{2}, \frac{1}{3}, \frac{1}{4}, \dots, \frac{1}{p}; \quad p \leq 137 \text{ is an integer} \quad (2c)$$

replaces the well known parameter  $n = \text{integer}$  in the Rydberg equation for hydrogen excited states. The  $n = 1$  state of hydrogen and the  $n = \frac{1}{\text{integer}}$  states of hydrogen are nonradiative, but

a transition between two nonradiative states, say  $n = 1$  to  $n = 1/2$ , is possible via a nonradiative energy transfer. Thus, a catalyst provides a net positive enthalpy of reaction of  $m \cdot 27.2 \text{ eV}$  (i.e. it resonantly accepts the nonradiative energy transfer from hydrogen atoms and releases the energy to the surroundings to affect electronic transitions to fractional quantum energy levels). As a consequence of the nonradiative energy transfer, the hydrogen atom becomes unstable and emits further energy until it achieves a lower-energy nonradiative state having a principal energy level given by Eqs. (2a) and (2c).

The catalyst product,  $H(1/p)$ , may also react with an electron to form a novel hydride ion  $H^-(1/p)$  with a binding energy  $E_B$  [1, 13-14, 18, 30]:

$$E_B = \frac{\hbar^2 \sqrt{s(s+1)}}{8\mu_e a_0^2 \left[ \frac{1 + \sqrt{s(s+1)}}{p} \right]^2} - \frac{\pi\mu_0 e^2 \hbar^2}{m_e^2} \left( \frac{1}{a_H^3} + \frac{2^2}{a_0^3 \left[ \frac{1 + \sqrt{s(s+1)}}{p} \right]^3} \right) \quad (3)$$

where  $p = \text{integer} > 1$ ,  $s = 1/2$ ,  $\hbar$  is Planck's constant bar,  $\mu_0$  is the permeability of vacuum,

$m_e$  is the mass of the electron,  $\mu_e$  is the reduced electron mass given by  $\mu_e = \frac{m_e m_p}{\frac{m_e}{\sqrt{3}} + m_p}$  where

$m_p$  is the mass of the proton,  $a_0$  is the Bohr radius, and the ionic radius is  $r_1 = \frac{a_0}{p} \left( 1 + \sqrt{s(s+1)} \right)$ .

From Eq. (3), the calculated ionization energy of the hydride ion is  $0.75418 \text{ eV}$ , and the experimental value given by Lykke [47] is  $6082.99 \pm 0.15 \text{ cm}^{-1}$  ( $0.75418 \text{ eV}$ ).

Upfield-shifted NMR peaks are direct evidence of the existence of lower-energy state hydrogen with a reduced radius relative to ordinary hydride ion and having an increase in diamagnetic shielding of the proton. The shift is given by the sum of that of an ordinary hydride ion  $H^-$  and a component due to the lower -energy state [1, 15]:

$$\frac{\Delta B_T}{B} = -\mu_0 \frac{e^2}{12m_e a_0 \left( 1 + \sqrt{s(s+1)} \right)} (1 + \alpha 2\pi p) = -(29.9 + 1.37p) \text{ ppm} \quad (4)$$

where for  $H^-$   $p = 0$  and  $p = \text{integer} > 1$  for  $H^-(1/p)$  and  $\alpha$  is the fine structure constant.

$H(1/p)$  may react with a proton and two  $H(1/p)$  may react to form  $H_2(1/p)^+$  and  $H_2(1/p)$ , respectively. The hydrogen molecular ion and molecular charge and current density

functions, bond distances, and energies were solved previously [1, 6] from the Laplacian in ellipsoidal coordinates with the constraint of nonradiation.

$$(\eta - \zeta)R_\xi \frac{\partial}{\partial \xi} (R_\xi \frac{\partial \phi}{\partial \xi}) + (\zeta - \xi)R_\eta \frac{\partial}{\partial \eta} (R_\eta \frac{\partial \phi}{\partial \eta}) + (\xi - \eta)R_\zeta \frac{\partial}{\partial \zeta} (R_\zeta \frac{\partial \phi}{\partial \zeta}) = 0 \quad (5)$$

The total energy  $E_T$  of the hydrogen molecular ion having a central field of  $+pe$  at each focus of the prolate spheroid molecular orbital is

$$E_T = -p^2 \left\{ \frac{e^2}{8\pi\epsilon_0 a_H} (4 \ln 3 - 1 - 2 \ln 3) \left[ 1 + p \sqrt{\frac{2\hbar \sqrt{\frac{2e^2}{4\pi\epsilon_0 (2a_H)^3}}}{m_e}}}{m_e c^2} \right] - \frac{1}{2} \hbar \sqrt{\frac{k}{\mu}} \right\} \quad (6)$$

$$= -p^2 16.13392 \text{ eV} - p^3 0.118755 \text{ eV}$$

where  $p$  is an integer,  $c$  is the speed of light in vacuum,  $\mu$  is the reduced nuclear mass, and  $k$  is the harmonic force constant solved previously in a closed-form equation with fundamental constants only [1, 6]. The total energy of the hydrogen molecule having a central field of  $+pe$  at each focus of the prolate spheroid molecular orbital is

$$E_T = -p^2 \left\{ \frac{e^2}{8\pi\epsilon_0 a_0} \left[ \left( 2\sqrt{2} - \sqrt{2} + \frac{\sqrt{2}}{2} \right) \ln \frac{\sqrt{2}+1}{\sqrt{2}-1} - \sqrt{2} \right] \left[ 1 + p \sqrt{\frac{2\hbar \sqrt{\frac{e^2}{4\pi\epsilon_0 a_0^3}}}{m_e}}}{m_e c^2} \right] - \frac{1}{2} \hbar \sqrt{\frac{k}{\mu}} \right\} \quad (7)$$

$$= -p^2 31.351 \text{ eV} - p^3 0.326469 \text{ eV}$$

The bond dissociation energy,  $E_D$ , of the hydrogen molecule  $H_2(1/p)$  is the difference between the total energy of the corresponding hydrogen atoms and  $E_T$

$$E_D = E(2H(1/p)) - E_T \quad (8)$$

where [48]

$$E(2H(1/p)) = -p^2 27.20 \text{ eV} \quad (9)$$

$E_D$  is given by Eqs. (8-9) and (7):

$$\begin{aligned} E_D &= -p^2 27.20 \text{ eV} - E_T \\ &= -p^2 27.20 \text{ eV} - (-p^2 31.351 \text{ eV} - p^3 0.326469 \text{ eV}) \\ &= p^2 4.151 \text{ eV} + p^3 0.326469 \text{ eV} \end{aligned} \quad (10)$$

The calculated and experimental parameters of  $H_2$ ,  $D_2$ ,  $H_2^+$ , and  $D_2^+$  from Ref. [1, 6] are given in Table 1.

The  $^1H$  NMR resonance of  $H_2(1/p)$  is predicted to be upfield from that of  $H_2$  due to the fractional radius in elliptic coordinates [1, 6] wherein the electrons are significantly closer to the nuclei. The predicted shift,  $\frac{\Delta B_T}{B}$ , for  $H_2(1/p)$  derived previously [1, 6] is given by the sum of that of  $H_2$  and a term that depends on  $p = \text{integer} > 1$  for  $H_2(1/p)$ :

$$\frac{\Delta B_T}{B} = -\mu_0 \left( 4 - \sqrt{2} \ln \frac{\sqrt{2} + 1}{\sqrt{2} - 1} \right) \frac{e^2}{36a_0 m_e} (1 + \pi \alpha p) \quad (11)$$

$$\frac{\Delta B_T}{B} = -(28.01 + 0.64 p) ppm \quad (12)$$

where for  $H_2$   $p = 0$ .

The vibrational energies,  $E_{vib}$ , for the  $\nu = 0$  to  $\nu = 1$  transition of hydrogen-type molecules  $H_2(1/p)$  are [1, 6]

$$E_{vib} = p^2 0.515902 eV \quad (13)$$

where  $p$  is an integer and the experimental vibrational energy for the  $\nu = 0$  to  $\nu = 1$  transition of  $H_2$ ,  $E_{H_2(\nu=0 \rightarrow \nu=1)}$ , is given by Beutler [49] and Herzberg [50].

The rotational energies,  $E_{rot}$ , for the  $J$  to  $J+1$  transition of hydrogen-type molecules  $H_2(1/p)$  are [1, 6]

$$E_{rot} = E_{J+1} - E_J = \frac{\hbar^2}{I} [J+1] = p^2 (J+1) 0.01509 eV \quad (14)$$

where  $p$  is an integer,  $I$  is the moment of inertia, and the experimental rotational energy for the  $J = 0$  to  $J = 1$  transition of  $H_2$  is given by Atkins [51].

The  $p^2$  dependence of the rotational energies results from an inverse  $p$  dependence of the internuclear distance and the corresponding impact on the moment of inertia  $I$ . The predicted internuclear distance  $2c'$  for  $H_2(1/p)$  is

$$2c' = \frac{a_0 \sqrt{2}}{p} \quad (15)$$

The formation of new states of hydrogen is very energetic. A new chemically generated or assisted plasma source based on the resonant energy transfer mechanism (rt-plasma) has been developed that may be a new power source. One such source operates by incandescently heating a hydrogen dissociator and a catalyst to provide atomic hydrogen and gaseous catalyst, respectively, such that the catalyst reacts with the atomic hydrogen to produce a plasma. It was extraordinary that intense EUV emission was observed by Mills et al. [13-21, 38-39] at low temperatures (e.g.  $\approx 10^3 K$ ), as well as an extraordinary low field strength of about 1-2 V/cm from atomic hydrogen and certain atomized elements or certain gaseous ions, which singly or multiply ionize at integer multiples of the potential energy of atomic hydrogen, 27.2 eV.

$K$  to  $K^{3+}$  provides a reaction with a net enthalpy equal to three times the potential energy of atomic hydrogen. It was reported previously [13-21, 38-39] that the presence of these gaseous atoms with thermally dissociated hydrogen formed an rt-plasma having strong EUV emission with a stationary inverted Lyman population. Other noncatalyst metals such as  $Mg$  produced no plasma. Significant line broadening of the Balmer  $\alpha$ ,  $\beta$ , and  $\gamma$  lines of 18 eV was observed. Emission from rt-plasmas occurred even when the electric field applied to the plasma was zero. Since a conventional discharge power source was not present, the formation of a plasma would require an energetic reaction. The origin of Doppler broadening is the relative thermal motion of the emitter with respect to the observer. Line broadening is a measure of the atom temperature, and a significant increase was expected and observed for catalysts,  $K$  as well as  $Sr^+$  or  $Ar^+$

[13-21, 38-39], with hydrogen. The observation of a high hydrogen temperature with no conventional explanation would indicate that an rt-plasma must have a source of free energy. An energetic chemical reaction was further implicated since it was found that the broadening is time dependent [13-14, 20]. Therefore, the thermal power balance was measured calorimetrically. The reaction was exothermic since excess power of  $20 \text{ mW} \cdot \text{cm}^{-3}$  was measured by Calvet calorimetry [20]. In further experiments,  $\text{KNO}_3$  and Raney nickel were used as a source of the  $\text{K}$  catalyst and atomic hydrogen, respectively, to produce the corresponding exothermic reaction. The energy balance was  $\Delta H = -17,925 \text{ kcal/mole KNO}_3$ , about 300 times that expected for the most energetic known chemistry of  $\text{KNO}_3$ , and  $-3585 \text{ kcal/mole H}_2$ , over 60 times the hypothetical maximum enthalpy of  $-57.8 \text{ kcal/mole H}_2$  due to combustion of hydrogen with atmospheric oxygen, assuming the maximum possible  $\text{H}_2$  inventory [14]. Additional substantial evidence of an energetic catalytic reaction was previously reported [13-15, 24-26, 30-31] involving a resonant energy transfer between hydrogen atoms and  $\text{K}$  to form very stable novel hydride ions and molecules  $\text{H}^-(1/4)$  and  $\text{H}_2(1/4)$ , respectively. Characteristic emission was observed from  $\text{K}^{3+}$  that confirmed the resonant nonradiative energy transfer of  $3 \cdot 27.2 \text{ eV}$  from atomic hydrogen to  $\text{K}$  that served as a predicted catalyst. From Eq. (3), the binding energy  $E_B$  of  $\text{H}^-(1/4)$  is

$$E_B = 11.232 \text{ eV} (\lambda_{\text{vac}} = 110.38 \text{ nm}) \quad (16)$$

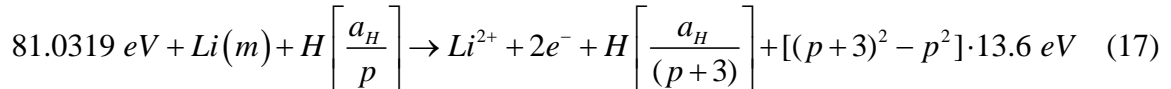
The product hydride ion  $\text{H}^-(1/4)$  was observed by EUV spectroscopy at  $110 \text{ nm}$  corresponding to its predicted binding energy of  $11.2 \text{ eV}$  [13-15, 24-26, 30-31]. The identification of  $\text{H}^-(1/4)$  was confirmed previously by the XPS measurement of its binding energy. The XPS spectrum of  $\text{KH}^* \text{I}$  differed from that of  $\text{KI}$  by having additional features at  $8.9 \text{ eV}$  and  $10.8 \text{ eV}$  that did not correspond to any other primary element peaks but did match the  $\text{H}^-(1/4) E_b = 11.2 \text{ eV}$  hydride ion (Eq. (3)) in two different chemical environments. The  $^1\text{H}$  MAS NMR spectrum of novel compound  $\text{KH}^* \text{Cl}$  relative to external tetramethylsilane (TMS) showed a large distinct upfield resonance at  $-4.4 \text{ ppm}$  corresponding to an absolute resonance shift of  $-35.9 \text{ ppm}$  that matched the theoretical prediction of  $p = 4$  [13-15, 25-26, 30-31]. Elemental analysis identified [13-15, 25-26, 30-31] these compounds as only containing the alkaline metal, halogen, and hydrogen, and no known hydride compound of this composition could be found in the literature that had an upfield-shifted hydride NMR peak. Ordinary alkali hydrides alone or mixed with alkali halides show down-field shifted peaks [13-15, 25-26, 30-31]. From the literature, the list of alternatives to  $\text{H}^-(1/p)$  as a possible source of the upfield NMR peaks was limited to U centered H. This was eliminated by the absence of the intense and characteristic infrared vibration band at  $503 \text{ cm}^{-1}$  due to the substitution of  $\text{H}^-$  for  $\text{Cl}^-$  in  $\text{KCl}$  [52].

As a further characterization, FTIR analysis of  $\text{KH}^* \text{I}$  crystals with  $\text{H}^-(1/4)$  was performed and interstitial  $\text{H}_2(1/4)$  having a predicted rotational energy given by Eq. (14) was observed. Rotational lines were observed previously [13-14] in the  $145\text{-}300 \text{ nm}$  region from atmospheric pressure electron beam-excited argon-hydrogen plasmas. The unprecedented energy spacing of  $4^2$  times that of hydrogen established the internuclear distance as  $1/4$  that of  $\text{H}_2$  and identified  $\text{H}_2(1/4)$  (Eqs. (13-15)). The spectrum was asymmetric with the P branch dominant corresponding to the population of higher-energy rotational states during the transition

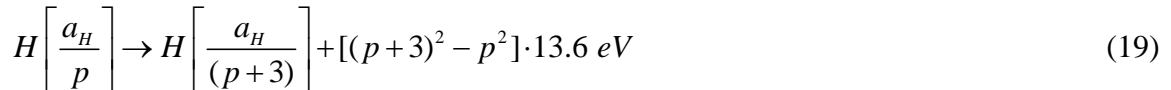
from the excited  $\nu' = 1$  vibrational state to  $\nu'' = 0$  ground state. Typically, the P and R branches have equal intensity since a molecule is in thermal equilibrium with the ambient gas and upward or downward conversion of the vibrational energy by the coupled rotational-transition energy occurs with equal probability. This, in turn, occurs because vibrational emission involves the creation of an electromagnetic field wherein the near field can couple with any rotational dipole present, and the transition coefficient  $A_{ki}$  is symmetrical with respect to excitation or decay of rotational states. In contrast, thermal equilibrium is not possible for  $H_2(1/4)$  due to the high rotational energy (10 times the thermal energy), and a competing internal energy coupling mechanism becomes dominant that is akin to an Auger cascade, excimer-atomic resonant energy transfer (e.g.  $Ne_2^*/H$ ), intersystem crossing, and intramolecular energy transfer between linked fluorescent species wherein the absorption spectrum of an acceptor species matches the fluorescent emission spectrum of an excited species of a linked pair. Based on an adaptation of Förster's theory shown in Chp. 6 of Ref. [1], the much smaller dimensions of  $H_2(1/4)$  together with the internal transfer rate having a  $1/r^6$  separation dependency cause internal energy transfer to be more probable than the conventional emission process during the vibrational dipole transition. Thus, only higher upper states are populated significantly with an increase of  $J''$  by one during the  $\nu' = 1$  to  $\nu'' = 0$  transition following e-beam excitation.

$KH^*Cl$  having  $H^-(1/4)$  by NMR was incident to the 12.5 keV electron beam, which excited similar emission of interstitial  $H_2(1/4)$  as observed in the argon-hydrogen plasma [13-14]. Specifically,  $H_2(1/4)$  trapped in the lattice of  $KH^*Cl$  was investigated by windowless EUV spectroscopy on electron-beam excitation of the crystals using the 12.5 keV electron gun at pressures below which any gas could produce detectable emission ( $<10^{-5}$  Torr). The rotational energy of  $H_2(1/4)$  was confirmed by this technique as well. These results confirmed the previous observations from the plasmas formed by the energetic hydrino-forming reaction having intense hydrogen Lyman emission, a stationary inverted Lyman population, excessive afterglow duration, highly energetic hydrogen atoms, characteristic alkali-ion emission due to catalysis, predicted novel spectral lines, and the measurement of a power beyond any conventional chemistry [13-40] that matched predictions for a catalytic reaction of atomic hydrogen to form more stable hydride ions designated  $H^-(1/p)$ . Since the comparison of theory and experimental energies is direct evidence of lower-energy hydrogen with an implicit large exotherm during its formation, we report in this paper the results when these experiments were repeated with additionally predicted catalysts  $Li$  and  $NaH$ .

A catalytic system used to make and analyze predicted hydride compounds involves lithium atoms. The first and second ionization energies of lithium are 5.39172 eV and 75.64018 eV, respectively [53]. The double ionization ( $t = 2$ ) reaction of  $Li$  to  $Li^{2+}$  then, has a net enthalpy of reaction of 81.0319 eV, which is equivalent to  $3 \cdot 27.2$  eV.



And, the overall reaction is



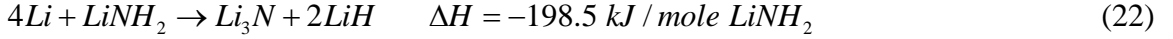
Lithium is a metal in the solid and liquid states, and the gas comprises covalent  $Li_2$  molecules [54], each having a bond energy of 110.4 kJ/mole [55]. In order to generate atomic lithium,  $LiNH_2$  was added to the reaction mixture.  $LiNH_2$  generates atomic hydrogen as well, according to the reversible reactions [56-65]:



and

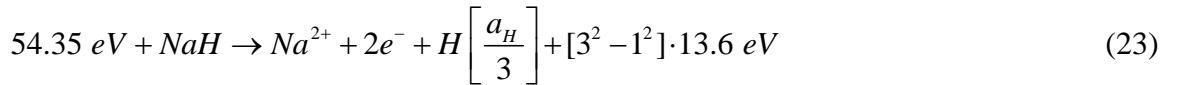


The energy for the reaction of lithium amide to lithium nitride and lithium hydride is exothermic [66-67]:



Thus, it should occur to a significant extent. The specific predictions of the energetic reaction given by Eqs. (17-19) were tested by rt-plasma formation and  $H$  line broadening. The power developed was measured using water-flow, batch calorimetry. Then, the predicted products of  $H^-(1/4)$  and  $H_2(1/4)$  having the energies given by Eqs. (3) and (5-15), respectively, were tested by magic angle solid proton nuclear magnetic resonance spectroscopy ( $^1H$  MAS NMR), X-ray photoelectron spectroscopy (XPS), time of flight secondary ion mass spectroscopy (ToF-SIMS), and Fourier transform infrared spectroscopy (FTIR).

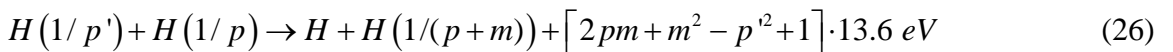
A compound comprising hydrogen such as  $MH$ , where  $M$  is an element other than hydrogen, serves as a source of hydrogen and a source of catalyst. A catalytic reaction is provided by the breakage of the  $M-H$  bond plus the ionization of  $t$  electrons from the atom  $M$  each to a continuum energy level such that the sum of the bond energy and ionization energies of the  $t$  electrons is approximately  $m \cdot 27.2 \text{ eV}$ , where  $m$  is an integer. One such catalytic system involves sodium. The bond energy of  $NaH$  is 1.9245 eV [55], and the first and second ionization energies of  $Na$  are 5.13908 eV and 47.2864 eV, respectively [53]. Based on these energies  $NaH$  molecule can serve as a catalyst and  $H$  source, since the bond energy of  $NaH$  plus the double ionization ( $t=2$ ) of  $Na$  to  $Na^{2+}$  is 54.35 eV ( $2 \cdot 27.2 \text{ eV}$ ). The catalytic reactions are given by



And, the overall reaction is



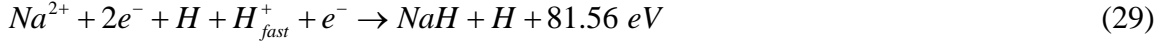
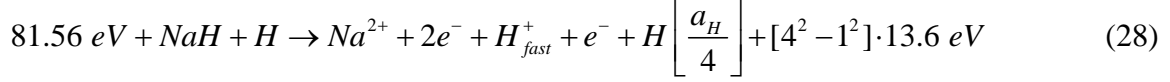
As given in Chp. 5 of Ref [1], and Ref. [29], hydrogen atoms  $H(1/p)$   $p=1,2,3,\dots,137$  can undergo further transitions to lower-energy states given by Eqs. (2a) and (2c) wherein the transition of one atom is catalyzed by a second that resonantly and nonradiatively accepts  $m \cdot 27.2 \text{ eV}$  with a concomitant opposite change in its potential energy. The overall general equation for the transition of  $H(1/p)$  to  $H(1/(p+m))$  induced by a resonance transfer of  $m \cdot 27.2 \text{ eV}$  to  $H(1/p')$  is represented by



In the case of a high hydrogen atom concentration, the transition of  $H(1/3)$  ( $p = 3$ ) to  $H(1/4)$  ( $p + m = 4$ ) with  $H$  as the catalyst ( $p' = 1$ ;  $m = 1$ ) can be fast:



The  $NaH$  catalyst reactions may be concerted since the sum of the bond energy of  $NaH$ , the double ionization ( $t = 2$ ) of  $Na$  to  $Na^{2+}$ , and the potential energy of  $H$  is  $81.56 \text{ eV}$  ( $3 \cdot 27.2 \text{ eV}$ ). The catalyst reactions are given by

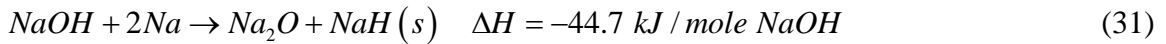


And, the overall reaction is

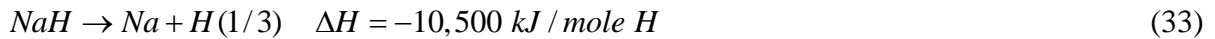
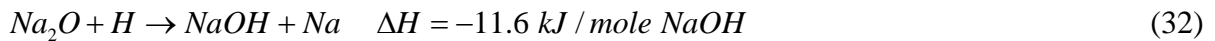


where  $H_{fast}^+$  is a fast hydrogen atom having at least  $13.6 \text{ eV}$  of kinetic energy.  $H^-(1/4)$  forms stable halidohydrides and is a favored product together with the corresponding molecule formed by the reactions  $2H(1/4) \rightarrow H_2(1/4)$  and  $H^-(1/4) + H^+ \rightarrow H_2(1/4)$  [13-15, 24-26, 30-31]. The corresponding hydride atom  $H(1/4)$  is a preferred final product consistent with observation since the  $p = 4$  quantum state has a multipolarity greater than that of a quadrupole giving it a long theoretical lifetime.  $H(1/4)$  may be formed directly from  $H$  (e.g. Eqs. (36-38)) or via multiple transitions (e.g. Eqs. (23-27)). In the latter case, the higher-energy  $H(1/p)$  states with quantum numbers  $p = 2$ ;  $\ell = 0, 1$  and  $p = 3$ ;  $\ell = 0, 1, 2$  corresponding to dipole and quadrupole transitions, respectively, have theoretically allowed, fast transitions.

Sodium hydride is typically in the form of an ionic crystalline compound formed by the reaction of gaseous hydrogen with metallic sodium. And, in the gaseous state, sodium comprises covalent  $Na_2$  molecules [54] with a bond energy of  $74.8048 \text{ kJ/mole}$  [55]. It was found that when  $NaH(s)$  was heated at a very slow temperature ramp rate ( $0.1^\circ\text{C/min}$ ) under a helium atmosphere to form  $NaH(g)$ , the predicted exothermic reaction given by Eqs. (23-25) was observed at high temperature by differential scanning calorimetry (DSC). To achieve high power, a chemical system was designed to greatly increase the amount and rate of formation of  $NaH(g)$ . The reaction of  $NaOH$  and  $Na$  to  $Na_2O$  and  $NaH(s)$  calculated from the heats of formation [55, 66] releases  $\Delta H = -44.7 \text{ kJ/mole NaOH}$ :



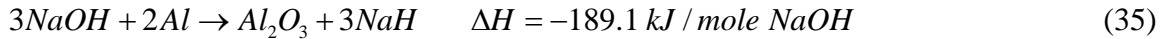
This exothermic reaction can drive the formation of  $NaH(g)$  and was exploited to drive the very exothermic reaction given by Eqs. (23-25). The regenerative reaction in the presence of atomic hydrogen is



and



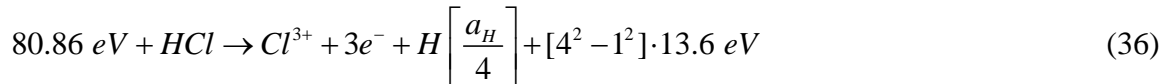
Thus, a small amount of  $NaOH$ ,  $Na$ , and atomic hydrogen serves as a catalytic source of the  $NaH$  catalyst that in turn forms a large yield of hydrinos via multiple cycles of regenerative reactions such as those given by Eqs. (31-34). R-Ni having a high surface area of about  $100\text{ m}^2/\text{g}$  and containing  $H$  was surface coated with  $NaOH$  and reacted with  $Na$  metal to form  $NaH(g)$ . Since the energy balance in the formation of  $NaH(g)$  was negligible due to the small amounts involved, the energy and power due to the hydrino reactions given by Eqs. (23-25) were specifically measured using water-flow, batch calorimetry. Next, R-Ni 2400 was prepared such that it comprised about 0.5 wt%  $NaOH$ , and the  $Al$  of the intermetallic served as the reductant to form  $NaH$  catalyst during calorimetry measurement. The reaction of  $NaOH + Al$  to  $Al_2O_3 + NaH$  calculated from the heats of formation [66] is exothermic by  $\Delta H = -189.1\text{ kJ/mole } NaOH$ . The balanced reaction is given by



This exothermic reaction can drive the formation of  $NaH(g)$  and was exploited to drive the very exothermic reaction given by Eqs. (23-25) wherein the regeneration of  $NaH$  occurred from  $Na$  in the presence of atomic hydrogen. For 0.5wt%  $NaOH$ , the exothermic reaction given by Eq. (35) gave a negligible  $\Delta H = -0.024\text{ kJ}$  background heat during measurement.

It was reported previously [28-29] that the reaction products  $H(1/p)$  may undergo further reaction to lower-energy states. For example, the catalyst reaction of  $Ar^+$  to  $Ar^{2+}$  forms  $H(1/2)$ , which may further serve as both a catalyst and a reactant to form  $H(1/4)$  [1, 13-14, 28-29] and the corresponding favored molecule  $H_2(1/4)$ , observed using different catalysts [13-14]. Thus, predicted products of  $NaH$  catalyst from Eqs. (23-25) and Table 1 of Ref. [29] are  $H^-(1/3)$  and  $H_2(1/4)$  having the energies given by Eqs. (3) and (5-15), respectively. They were tested by MAS and solution  $^1H$  NMR, ToF-SIMS, and XPS.

Another catalytic system of the type  $MH$  involves chlorine. The bond energy of  $HCl$  is 4.4703 eV [55]. The first, second, and third ionization energies of  $Cl$  are 12.96764 eV, 23.814 eV, and 39.61 eV, respectively [53]. Based on these energies,  $HCl$  can serve as a catalyst and  $H$  source, since the bond energy of  $HCl$  plus the triple ionization ( $t=3$ ) of  $Cl$  to  $Cl^{3+}$  is 80.86 eV ( $3 \cdot 27.2\text{ eV}$ ). The catalyst reactions are given by



And, the overall reaction is



The anticipated product then is  $H_2(1/4)$ .

Alkali chlorides contain both  $Cl$  and  $H$ , typically from  $H_2$  and  $H_2O$ . Thus, some  $HCl$  can form interstitially in the crystalline matrix. Since  $H^+$  can most easily substitute for  $Li^+$ , and the substitution is least likely in the case of  $Cs^+$ , it was anticipated that alkali chlorides may form  $HCl$  that undergoes catalysis to form  $H_2(1/4)$  with the trend of the rate of formation increasing in the order of the Group I elements. Another factor favoring this trend is that the

lattice spacing increases to accommodate the interstitial catalyst and  $H_2(1/4)$ . Due to the difference in lattice structure,  $MgCl_2$  may not form  $HCl$  catalyst; thus, it serves as a chlorine control. This condition applies to other alkaline earth halides and transition metal halides such as those of copper that can serve as controls for the formation of  $H_2(1/4)$ . One exception from this set is  $Mg^{2+}$  in a suitable lattice, since the ionization of  $Mg^{2+}$  to  $Mg^{3+}$  is 80.1437 eV [53] which is close to  $3 \cdot 27.2$  eV. These hypotheses were tested by electron beam-excitation emission spectroscopy on alkali halides,  $MgX_2$  ( $X = F, Cl, Br, I$ ), and  $CuX_2$  ( $X = F, Cl, Br$ ) with the goal of determining whether the predicted emission of  $H_2(1/4)$  is selectively observed when a catalyst reaction is possible and not otherwise. NMR was recorded on these compounds to search for the corresponding predicted  $H_2(1/4)$  peak to be compared with the emission results.

## II. Experimental

**Rt-plasma and Line Broadening Measurements.**  $LiNH_2$  argon-hydrogen (95/5%) and  $LiNH_2$  hydrogen rt-plasmas were generated in the experimental set up described previously [15-21] (Figure 1) comprising a thermally insulated stainless steel cell with a cap that incorporated ports for gas inlet and outlet. A tungsten filament (55 cm long, 0.5 mm diameter) that served as a heater and hydrogen dissociator was in the cell. 1 g of  $LiNH_2$  (Alfa Aesar 99.95%) was placed in the center of the cell under 1 atm of dry argon in a glove box. The cell was sealed and removed from the glove box. The cell was maintained at 50 °C for 4 hours with helium flowing at 30 sccm at a pressure of 1 Torr. The filament power was increased to 200 W in 20 W increments every 20 minutes. At 120 W, the filament temperature was estimated to be in the range 800 to 1000 °C. The external cell wall temperature was about 700 °C. The cell was then operated with and without an argon-hydrogen (95/5%) flow rate of 5.5 sccm maintained at 1 Torr. Additionally, the cell was operated with hydrogen gas flow replacing argon-hydrogen (95/5%). The  $LiNH_2$  was vaporized by the filament heater as evidenced by the presence of  $Li$  lines. The presence of an argon-hydrogen or hydrogen plasma was determined by recording the visible spectrum over the Balmer region. The plasma emission was fiber-optically coupled to a Jobin Yvon Horiba 1250 M spectrometer through a high-quality UV (200-800 nm) fiber-optic bundle and a 220F matching fiber adapter with an aperture of 0.12 and a corresponding acceptance angle of 12°. The spectrometer had a 1250 mm focal length with a 2400 g/mm grating and a detector comprising a Symphony model, liquid-nitrogen cooled, back illuminated 2048×512 CCD array with an element size of 13.5  $\mu\text{m}$  × 13.5  $\mu\text{m}$ , 16 bit ADC, and 20 KHz and 1 MHz read outs. Using the 546 nm Hg I line from NIST calibrated mercury lamp with the entrance and exit slits set to 20  $\mu\text{m}$  the measured CCD resolution due to the finite-pixel-spectral width was very high,  $\pm 0.006$  nm. The spectrometer accuracy was  $\pm 0.05$  nm, and its repeatability was  $\pm 0.005$  nm. The width of the 656.3 nm Balmer  $\alpha$  line emitted from the argon-hydrogen (95/5%)- $LiNH_2$  or hydrogen- $LiNH_2$  rt-plasma having a tungsten filament was measured initially and periodically during operation. As further controls, the experiment was run with each of the flowing gases in the absence of  $LiNH_2$ . In each case, the spectrometer was scanned through the emission profile of the Balmer line with a step size of 0.01 nm and a 3 second integration time.

**Differential Scanning Calorimetry (DSC) Measurements.** Differential scanning calorimeter (DSC) measurements were performed using the DSC mode of a Setaram HT-1000 calorimeter (Setaram, France). Two matched alumina glove fingers were used as the sample compartment and the reference compartment. The fingers permitted the control of the reaction atmosphere. 0.067 g  $NaH$  was placed in a flat-base Al-23 crucible (Alfa-Aesar, 15 mm high x 10 mm OD x 8 mm ID). The crucible was then placed in the bottom of the sample alumina glove finger cell. As a reference, an aluminum oxide sample (Alfa-Aesar, -400 Mesh powder, 99.9%) with matching weight of the sample was placed in a matched Al-23 crucible. All samples were handled in a glove box. Each alumina glove finger cell was sealed in the glove box, removed from the glove box, and then quickly attached to the Setaram calorimeter. The system was immediately evacuated to a pressure of 1 mTorr or less. The cell was back filled with 1 atm of helium, evacuated again, and then refilled with helium to 760 Torr. The cells were then inserted into the oven, and secured to their positions in the DSC instrument. The oven temperature was brought to the desired starting temperature of 100 °C. The oven temperature was scanned from 100 °C to 750 °C at a ramp rate of 0.1 degree/minute. As a control,  $MgH_2$  replaced  $NaH$ . A 0.050 g  $MgH_2$  sample (Alfa-Aesar, 90%, remainder  $Mg$ ) was added to the sample cell, while a similar weight of aluminum oxide (Alfa-Aesar) was added to the reference cell. Both samples were also handled in a glove box.

**Water-Flow, Batch Calorimetry.** The cylindrical stainless steel reactor of approximately 60  $cm^3$  volume (1.0" outside diameter (OD), 5.0" length, and 0.065" wall thickness) is shown in Figure 2. The cell further comprised a welded-in 2.5" long, cylindrical thermocouple well with a wall thickness of 0.035" along the centerline that held a Type K thermocouple (Omega) read by a meter (DAS). For the cell sealed with a high temperature valve, a 3/8" OD, 0.065" thick SS tube welded at the end of the cell 1/4" off-center served as a port to introduce combinations of the reagents comprising the group of (i) 1g  $Li$ , 0.5g  $LiNH_2$ , 10g  $LiBr$ , and 15g  $Pd/Al_2O_3$ , (ii) 1g  $Li$ , 0.5g  $LiNH_2$ , (iii) 3.28 g  $Na$ , 15g Raney (R-)  $Ni/Al$  alloy, (iv) 15g R- $Ni$  doped with  $NaOH$ , and (v) 3 wt%  $Al(OH)_3$  doped  $Ni/Al$  alloy. In the case that this port was spot-weld sealed, the SS tube had a 1/4" OD and a 0.02" wall-thickness. The reactants were loaded in a glove box, and a valve was attached to the port tube to seal the cell before it was removed from the glove box and connected to a vacuum pump. The cell was evacuated to a pressure of 10 mTorr and crimped. The cell was then sealed with the valve or hermetically sealed by spot-welding 1/2" from the cell with the remaining tube cut off.

The reactor was installed inside a cylindrical calorimeter chamber shown in Figure 3. The stainless steel chamber had 15.2 cm ID, 0.305 cm wall thickness, and 40.4 cm length. The chamber was sealed at both ends by removable stainless steel plates and Viton o-rings. The space between the reactor and the inside surface of the cylindrical chamber was filled with high temperature insulation. The gas composition and pressure in the chamber was controlled to modulate the thermal conductance between the reactor and the chamber. The interior of the chamber was first filled with 1000 Torr helium to allow the cell to reach ambient temperature, the chamber was then evacuated during the calorimetric run to increase the cell temperature. Afterwards, 1000 Torr helium was added to increase the heat transfer rate from the hot cell to the coolant and balance any heat associated with P-V work. The relative dimensions of the reactor and the chamber were such that heat flow from the reactor to the chamber was primarily radial. Heat was removed from the chamber by cooling water which flowed turbulently through 6.35 mm OD copper tubing, which was wound tightly (63 turns) onto the outer cylindrical surface of

the chamber. The reactor and chamber system were designed to safely absorb a thermal power pulse of 50 kW with a one minute duration. The absorbed energy was subsequently released to the cooling water stream in a controlled manner for calorimetric measurement. The temperature rise of the cooling water was measured by precision thermistor probes (Omega, OL-703-PP, 0.01°C) at the cooling coil inlet and exit. The inlet water temperature was controlled by a Cole Palmer (digital Polystat, model 12101-41) circulating bath with 0.01°C temperature stability and 900 W cooling capacity at 20°C. A well insulated eight-liter damping tank was installed just downstream of the bath in order to reduce temperature fluctuations caused by cycling of the bath. Coolant flow through the system was maintained by an FMI model QD variable flow rate positive displacement lab pump. Cooling water flow rate was set by a variable area flow meter with a high-resolution control valve. The flow meter was calibrated directly by water collection in situ. A secondary flow rate measurement was performed by a turbine flow meter (McMillan Co., G111 Flometer, ± 1 %) which continuously output the flow rate to the data acquisition system. The calorimeter chamber was installed in a covered HDPE tank which was filled with melamine foam insulation to minimize heat loss from the system. Careful measurement of the thermal power release to the coolant and comparison with the measured input power indicated that thermal losses were less than 2-3 %.

The calorimeter was calibrated with a precision heater applied for a set time period to determine the percentage recovery of the total energy applied by the heater. The energy recovery was determined by integrating the total output power  $P_T$  over time. The power was given by

$$P_T = \dot{m}C_p\Delta T \quad (39)$$

where  $\dot{m}$  was the mass flow rate,  $C_p$  was the specific heat of water, and  $\Delta T$  was the absolute change in temperature between the inlet and outlet where the two thermistors were matched to correct any offset using a constant flow with no input power. In the first step of the calibration test, an empty reaction cell, that was identical to the latter tested power cell containing the reactants, was evacuated to below 1 Torr and inserted into the calorimeter vacuum chamber. The chamber was evacuated and then filled with helium to 1000 Torr. The unpowered assembly reached equilibrium over an approximately two-hour period at which time the temperature difference between the thermistors became constant. The system was run another hour to confirm the value of the difference due to absolute calibrations of the two sensors. The magnitude of the correction was 0.036 °C, and it was confirmed to be consistent over all of the tests performed over the reported data set.

To increase the temperature of the cell per input power, ten minutes before the end of the ten-hour equilibration period, helium was evacuated from the chamber by the vacuum pump, and the chamber was maintained under dynamic pumping at a pressure below 1 Torr. 100.00 W of power was supplied to the heater (50.23 V and 1.991 A) for a period of 50 minutes. During this period, the cell temperature increased to approximately 650 °C, and the maximum change in water temperature (outlet minus inlet) was approximately 1.2 °C. After 50 minutes, the program directed the power to zero. To increase the rate of heat transfer to the coolant, the chamber was re-pressurized with 1000 Torr of helium and the assembly was allowed to fully reach equilibrium over a 24-hour period as confirmed by the observation of full equilibrium in the flow thermistors.

The hydrino-reaction procedure followed that of the calibration run, but the cell contained the reagents. The equilibration period with 1000 Torr helium in the chamber was 90 minutes. 100.00 W of power was applied to the heater, and after 10 minutes, the helium was evacuated from the chamber. The cell heated at a faster rate post evacuation, and the reagents

reached a hydrido reaction threshold temperature of 190 °C at 57 minutes. The onset of reaction was confirmed by a rapid rise in cell temperature that reached 378 °C at about 58 minutes. After ten minutes, the power was terminated, and helium was reintroduced into the cell slowly over a period of 1 hour at a rate of 150 sccm.

The water-flow calorimeter was scaled-up using the previous design to accommodate a 100-fold increase in power measurement. The method of measure was the same as that of the smaller-scale with appropriate corresponding time intervals. The reagent comprised 1 kg of R-Ni doped with 0.5wt% NaOH.

Quantitative X-ray diffraction (XRD) was performed on the control, 3 wt% Al(OH)<sub>3</sub> doped Ni/Al alloy, reactants, 0.1 wt% NaOH-doped R-Ni 2800 or 0.5 wt% NaOH-doped R-Ni, and the R-Ni reaction products as well as those of the reaction mixture comprising Li (1 g) and LiNH<sub>2</sub> (0.5 g) (Alfa Aesar 99%), LiBr (10g) (Alfa Aesar ACS grade 99+%), and Pd/Al<sub>2</sub>O<sub>3</sub> (15g) (1% Pd, Alfa Aesar) using hermetically sealed sample holders (Bruker Model #A100B37) loaded in a glove box under argon and analyzed with a Siemens D5000 diffractometer using Cu radiation at 40kV/30mA over the range 10° - 70° with a step size of 0.02° and a counting time of eight hours. Elemental analysis of the R-Ni was provided by the manufacturer, W. R. Grace Davidson, and the wt% NaOH was confirmed by elemental analysis (Galbraith) performed on samples handled in an inert atmosphere. In addition, a weighed sample of R-Ni in a 16.5 cm<sup>3</sup> stainless steel cell connected to a vacuum system having a total volume of 291 cm<sup>3</sup> was heated with a temperature ramp from 25°C to 550°C to decompose any physically absorbed or chemisorbed gasses and to identify and quantify the released gasses. The hydrogen content was determined by mass spectroscopy, quantitative gas chromatography (HP 5890 Series II with a ShinCarbon ST 100/120 micropacked column (2 m long, 1/16" OD), N<sub>2</sub> carrier gas with a flow rate of 14 ml/min, an oven temperature of 80 °C, an injector temperature of 100 °C, and thermal-conductivity detector temperature of 100 °C), and by using the ideal gas law and the measured pressure, volume, and temperature. Hydrogen dominated each analysis with trace water only detected by mass spectroscopy, and <2% methane was also quantified by gas chromatography. The trace water of the R-Ni and controls was quantified independently of the hydrogen by liquefying the H<sub>2</sub>O in a liquid nitrogen trap, pumping off the hydrogen, and allowing all the water to vaporize by using a sample size of 0.5 g which is less than that which gives rise to a saturated water-vapor pressure at room temperature in the system having a volume of 285.3 cm<sup>3</sup>.

**Synthesis and Solid <sup>1</sup>H MAS NMR of LiH \* X and NaH \* X.** Lithium halohydridohydrides (LiH \* X and X = halide) were synthesized by reaction of hydrogen with Li (1 g) and LiNH<sub>2</sub> (0.5 g) (Alfa Aesar 99%) as a source of atomic catalyst and additional atomic H with the corresponding alkali halide (10 g, Alfa Aesar ACS grade 99+% or 99.9 %), as an additional reactant. The compounds were prepared in a stainless steel gas cell (Figure 4) further containing Raney Ni (15 g) (W. R. Grace Davidson) as the hydrogen dissociator according to the methods described previously [13-14]. The reactor was run at 500 °C in a kiln for 72 hours with make-up hydrogen addition such that the pressure ranged cyclically between 1 Torr to 760 Torr. Then, the reactor was cooled under helium atmosphere. The sealed reactor was then opened in a glove box under an argon atmosphere. NMR samples were placed in glass ampules, sealed with rubber septa, and transferred out of the glove box to be flame sealed. <sup>1</sup>H MAS NMR was performed on solid samples of LiH \* X (X is a halide) at Spectral Data

Services, Inc., Champaign, Illinois as described previously [13-14]. Chemical shifts were referenced to external TMS. XPS was also performed on crystalline samples that were handled as air-sensitive materials.

Since the synthesis reaction comprised  $LiNH_2$ , and  $Li_2NH$  was a reaction product, both were run as controls alone and in a  $LiBr$  or  $LiI$  matrix. The  $LiNH_2$  was the commercial starting material, and  $Li_2NH$  was synthesized by the reaction of  $LiNH_2$  and  $LiH$  [68] and by decomposition of  $LiNH_2$  [69] with the  $Li_2NH$  product confirmed by X-ray diffraction (XRD). To eliminate the possibility that the alkali halide influenced the local environment of the protons or that any given known species produced an NMR resonance that was shifted upfield relative to the ordinary peak, controls comprising  $LiH$  (Aldrich Chemical Company 99%),  $LiNH_2$ , and  $Li_2NH$  with an equimolar mixture of  $LiX$  were run. The controls were prepared by mixing equimolar amounts of compounds in a glove box under argon. To further eliminate F centers as a possible contributor to the local environment of the protons of any given known species to produce an upfield-shifted NMR resonance, electron spin resonance spectroscopy (ESR) was performed on the  $LiH * Br$  and  $LiH * I$  samples. For the ESR studies, the samples were loaded into 4 mm OD Suprasil quartz tubes and evacuated to a final pressure of  $10^{-4}$  Torr. ESR spectra were recorded with a Bruker ESP 300 X-band spectrometer at room temperature and 77 K. The magnetic field was calibrated with a Varian E-500 gauss meter. The microwave frequency was measured by a HP 5342A frequency counter.

Elemental analysis was performed at Galbraith Laboratories to confirm the product composition and to eliminate the possibility of NMR-detectable amounts of any transition metal hydrides or other exotic hydrides that may give rise to upfield-shifted peaks. Specifically, the abundance of all elements present in the product ( $Li, H, X$ ) and the stainless steel reaction vessel and R-Ni ( $Ni, Fe, Cr, Mo, Mn, Al$ ) were determined.

$NaH * Cl$  and  $NaH * Br$  were synthesized by reaction of hydrogen with  $Na$  (3.28 g) and  $NaH$  (1 g) (Aldrich Chemical Company 99%) as a source of  $NaH$  catalyst and intrinsic atomic  $H$  with the corresponding alkali halide (15 g),  $NaCl$  or  $NaBr$  (Alfa Aesar ACS grade 99+%), as an additional reactant. The compounds were prepared in a stainless steel gas cell (Figure 4) further containing  $Pt/Ti$  ( $Pt$  coated  $Ti$  (15 g); Titan Metal Fabricators, platinum plated titanium mini-expanded anode, 0.089 cm x 0.5 cm x 2.5 cm with 2.54  $\mu m$  of platinum) as the hydrogen dissociator. Each synthesis was run according to the methods described for  $Li$  except that the kiln was maintained at 500 °C, and the  $NaH * Cl$  synthesis was repeated without the addition of hydrogen gas to determine the effect of using  $NaH(s)$  as the sole hydrogen source. XPS was performed on  $NaH * Cl$  since no primary element peaks were possible in the region for  $H^-(1/4)$ , and NMR investigations of both products were performed.

In a second method,  $NaH * Cl$  and  $NaH * Br$  were synthesized from  $Na$  (0.5-1 g) (Alfa Aesar, ACS reagent),  $NH_4Cl$  (0.4 g) or  $NH_4Br$  (0.4-1.6 g) (Alfa Aesar, 99.5% min) as the only source of hydrogen, and  $NaCl$  or  $NaBr$  (10 g) (Alfa Aesar, 99.9% min) with the kiln maintained at 500 °C. NMR was performed.

In a third method,  $NaH * Cl$  was synthesized from  $NaCl$  (10 g) and the solid acid  $KHSO_4$  (1.6 g) as the only source of hydrogen with the kiln maintained at 580 °C. NMR was performed to test whether  $H^-(1/3)$  formed by the reactions of Eqs. (23-25) could be observed

when the rapid reaction to  $H^-$  (1/4) according to Eq. (27) was partially inhibited due to the absence of a high concentration of  $H$  from a dissociator with  $H_2$  or a hydride.

A silicon wafer (2 g, 0.5 x 0.5 x 0.05 cm, Silicon Quest International, silicon (100), boron-doped, cleaned by heating to 700 °C under vacuum) was coated by the product  $NaH * Cl$  and  $NaH *$  by placing it in reactants comprising  $Na$  (1.7 g),  $NaH$  (0.5 g),  $NaCl$  (10 g), and  $Pt/Ti$  (15 g) wherein the  $NaCl$  was initially heated to 400°C under vacuum to remove any  $H_2$ (1/4). The reaction was run at 550°C in the kiln for 19 hours with an initial hydrogen pressure of 760 Torr. XPS was performed on a spot comprising only sodium hydrino hydride coated silicon wafer ( $NaH *$ -coated  $Si$ ). The  $NaH * Cl$ -coated silicon wafer ( $NaH * Cl$ -coated  $Si$ ) was investigated by electron-beam excitation spectroscopy. An emission spectrum of a pressed pellet of the  $NaH * Cl$  crystals was also recorded.

$NaH * F$  was synthesized by reaction of  $Na$  (0.8 g),  $NaH$  (2 g) (Aldrich Chemical Company 99%), and  $NaF$  (10 g) (Alfa Aesar ACS grade 99+%). The compounds were prepared in a stainless steel gas cell (Figure 4) further containing  $\gamma-Al_2O_3$  (10g). Each synthesis was run according to the methods described for  $Li$  except that the kiln was maintained at 550 °C without the addition of hydrogen gas. Solid and liquid NMR were performed on  $NaH * F$ .

**ToF-SIMS Spectra.** The crystalline samples of  $MH * X$ ;  $M = Li$  or  $Na$ ,  $X = halide$  and the corresponding alkali halide controls were sprinkled onto the surface of a double-sided adhesive tape and characterized using a Physical Electronics TFS-2000 ToF-SIMS instrument. The primary ion gun utilized a  $^{69}Ga^+$  liquid metal source. A region on each sample of  $(60\mu m)^2$  was analyzed. In order to remove surface contaminants and expose a fresh surface, the samples were sputter-cleaned for 60 seconds using a  $180\mu m \times 100\mu m$  raster. The aperture setting was 3, and the ion current was 600 pA resulting in a total ion dose of  $10^{15} ions/cm^2$ .

During acquisition, the ion gun was operated using a bunched (pulse width 4 ns bunched to 1 ns) 15 kV beam [70-71]. The total ion dose was  $10^{12} ions/cm^2$ . Charge neutralization was active, and the post accelerating voltage was 8000 V. The positive and negative SIMS spectra were acquired. Representative post sputtering data is reported.

In addition, 0.1g  $Na$ , 0.5g  $NaH$ , and 15g  $Pt/Ti$  were loaded into the water flow calorimetry cell, and water flow calorimetry was performed under the same conditions as described for  $Na$  and  $R-Ni$ . The cell generated 15 kJ of excess energy; whereas, the theoretical energy balance from the decomposition of  $NaH$  is endothermic by +1.2 kJ. Thus, to confirm the presence of hydrino hydrides corresponding to the reactions given by Eqs. (23-25) as the source of the excess heat, a sample of the  $Pt/Ti$  coated with sodium hydrino hydride ( $NaH *$ -coated  $Pt/Ti$ ) was analyzed directly by the same procedure as for the crystalline samples except that the sputtering was for 100s. Unreacted  $Pt/Ti$  coated with the starting materials served as a control. XPS was also performed.

ToF-SIMS of  $R-Ni$  2400 reacted over a 48 hour period at 50°C was also performed by the same procedure as for the crystalline samples. The reactions to form hydrinos are given by Eqs. (32-35). Since the surface was coated with  $NaOH$ , sodium hydrino hydride compounds with  $NaOH$  were predicted.

**Solution NMR.** 50 mg of  $NaH * F$  was added to 1.5 ml of deuterated N,N-dimethylformamide- $d_7$  ( $DCON(CD_3)_2$ ), DMF- $d_7$ , 99.5% Cambridge Isotope Laboratories, Inc.

Cat. #DLM-25-10) in a vial that was sealed with a glass Teflon valve, agitated, and allowed to dissolve over a 12 hour-period in a glove box under an argon atmosphere. The solution was transferred to an NMR tube (5 mm OD, 23 cm length, Wilmad) by a gas-tight connection. The tube was immersed in liquid nitrogen (LN) to freeze the sample, and the sample was pumped to remove nonsoluble gases. The sample was then thawed, refrozen using LN, and pumped again, followed by flame-sealing of the tube. Control NMR samples comprised the starting materials added to DMF with the dissolved portion analyzed. In addition, *NaH* (Aldrich Chemical Company 99%) was mixed with different amounts of DMF that contained water in order to titrate the reaction of *NaH* with water to completion. The NMR spectra were recorded with a 500 MHz Bruker NMR spectrometer that was deuterium locked. The chemical shifts were referenced to the frequency of DMF-d7 at 8.03 ppm.

$^1\text{H}$  solution NMR was also performed on solid *KH\*Cl*, *KH\*I* and *NaOH*-doped R-Ni 2400 product gases. *KH\*Cl* was synthesized at 600 °C using a reaction mixture comprising 1.5 atmospheric-pressure hydrogen, 1.6 g *K* covered with 20 g *KCl*, and 15 g Ni screen as the hydrogen dissociator, and *KH\*I* was synthesized at 500 °C using a reaction mixture comprising 1.5 atmospheric-pressure hydrogen, 1.6 g *K* covered with 20 g *KI*, and 15 g R-Ni screen as the hydrogen dissociator according to the methods described previously [24-26].  $^1\text{H}$  R-Ni product gases were collected and dissolved in DMF-d7 initially under liquid helium.

**XPS Spectra.** A series of XPS analyses were made on the crystalline samples using a Scienta 300 XPS Spectrometer. The fixed analyzer transmission mode and the sweep acquisition mode were used. The step energy in the survey scan was 0.5 eV, and the step energy in the high-resolution scan was 0.15 eV. In the survey scan, the time per step was 0.4 seconds, and the number of sweeps was 4. In the high-resolution scan, the time per step was 0.3 seconds, and the number of sweeps was 30. C 1s at 284.5 eV was used as the internal standard.

**FTIR Spectroscopy.** FTIR analysis was performed on solid-sample-*KBr* pellets of *LiH\*Br* using the transmittance mode at the Department of Chemistry, Princeton University, New Jersey, using a Nicolet 730 FTIR spectrometer with DTGS detector at resolution of 4  $\text{cm}^{-1}$  as described previously [13-14]. The samples were handled under an inert atmosphere. The resolution was 0.5  $\text{cm}^{-1}$ . Controls comprised *LiNH<sub>2</sub>*, *Li<sub>2</sub>NH*, and *Li<sub>3</sub>N* that were commercially available except *Li<sub>2</sub>NH* that was synthesized by the reaction of *LiNH<sub>2</sub>* and *LiH* [68] and by decomposition of *LiNH<sub>2</sub>* [69] with the *Li<sub>2</sub>NH* product confirmed by X-ray diffraction (XRD).

**UV Spectroscopy of Electron-Beam Excited Interstitial  $\text{H}_2(1/4)$ .** Vibration-rotational emission of  $\text{H}_2(1/4)$  trapped in the lattice of alkali halides, *MgCl<sub>2</sub>*, and in a silicon wafer was investigated via electron bombardment of the crystals. Windowless UV spectroscopy of the emission from electron-beam excitation of the crystals was recorded using a 12.5 keV electron gun at a beam current of 10-20  $\mu\text{A}$  in the pressure range of  $<10^{-5}$  Torr. The UV spectrum was recorded with a photomultiplier tube (PMT). The wavelength resolution was about 2 nm (FWHM) with an entrance and exit slit width of 300  $\mu\text{m}$ . The increment was 0.5 nm and the dwell time was 1 second.

### III. Results and Discussion

**A. RT-plasma Emission and Balmer  $\alpha$  Line Widths.** An argon-hydrogen (95/5%)-lithium rt-plasma formed with a low field (1V/cm), at low temperatures (e.g.  $\approx 10^3$  K), from hydrogen and *LiNH<sub>2</sub>* that was dissociated to atomic H and vaporized, respectively, using a tungsten filament.

Lithium and H emission were observed that confirmed  $LiNH_2$  and its decomposition product  $Li$  served as a source of atomic  $Li$  and  $H$ . Argon of the argon-hydrogen mixture increased the amount of atomic H as evidenced by the significantly decreased H emission in the absence of argon.  $H$  Balmer emission corresponding to population of a level with energy  $>12 eV$  was observed, as shown in Figures 5 and 6, which also requires that Lyman emission was present.

No plasma formed with argon/hydrogen alone. No possible chemical reaction of the tungsten filament, the vaporized  $LiNH_2$ , and 0.6 Torr argon-hydrogen mixture at a cell temperature of  $700^\circ C$  could be found to account for the Balmer emission. In fact, no known chemical reaction releases enough energy to excite Balmer and Lyman emission from hydrogen. In addition to known chemical reactions, electron collisional excitation, resonant photon transfer, and the lowering of the ionization and excitation energies by the state of “non ideality” in dense plasmas were also rejected as the source of ionization or excitation to form the hydrogen plasma [21]. The formation of an energetic reaction of atomic hydrogen was consistent with a source of free energy from the catalysis of atomic hydrogen by  $Li$ .

The energetic hydrogen atom energies were calculated from the width of the 656.3 nm Balmer  $\alpha$  line emitted from RF rt-plasmas. Each Balmer  $\alpha$  spectral line was fit using one or two Gaussian curves: one for the “cold” ( $<1 eV$ ) hydrogen and the second for “hot” ( $>10 eV$ ) hydrogen. The full half-width  $\Delta\lambda_G$  of each Gaussian results from the Doppler ( $\Delta\lambda_D$ ) and instrumental ( $\Delta\lambda_I$ ) half-widths:

$$\Delta\lambda_G = \sqrt{\Delta\lambda_D^2 + \Delta\lambda_I^2} \quad (40)$$

The measured half-width  $\Delta\lambda_I$  of  $\pm 0.006 nm$  was negligible. Thus, the temperature was calculated from the Doppler half-width using the formula:

$$\Delta\lambda_D = 7.16 \times 10^{-7} \lambda_0 \left( \frac{T}{\mu} \right)^{1/2} \quad (41)$$

where  $\lambda_0$  is the line wavelength,  $T$  is the temperature in K ( $1 eV = 11,605 K$ ), and  $\mu$  is the molecular weight (=1 for atomic hydrogen). In each case, the average Doppler half-width that was not appreciably changed with pressure, varied by  $\pm 5\%$  corresponding to an error in the energy of  $\pm 10\%$ .

The 656.3 nm Balmer  $\alpha$  line widths recorded on the argon-hydrogen (95/5%)-lithium rt-plasma, initially and after 70 hours of operation, are shown in Figures 5A and 5B, respectively. The Balmer  $\alpha$  line profile of the plasma emission at both time points comprised two distinct Gaussian peaks, an inner, narrower peak corresponding to a slow component of less than 0.5 eV and an outer, significantly broadened peak corresponding to a fast component of  $>40 eV$ . The fast component accounted for 90% of the  $n = 3$  excited-state H population initially and increased to 97% at 70 hours. Only the hydrogen lines were broadened. As shown previously, the source of energy of the fast H cannot be attributed to any applied electric field, but is predicted by the mechanism of the catalysis of hydrogen to lower-states [32-37].

A lithium rt-plasma also formed in the case of pure  $H_2$  gas at a pressure of 1 Torr, except that the line broadening and populations were less, about 6 eV with only a 27% population, at the initial and 70-hour time points as shown in Figures 6A and 6B, respectively. This result was expected, since the excess  $H_2$  can react with  $Li$  to form  $LiH$  that catalyzes the destruction of  $LiNH_2$  by the reaction:



Thus, the reactions to produce atomic  $Li$  and  $H$  are diminished. In addition, argon of the argon-hydrogen mixture can increase the amount of atomic  $H$  by preventing its recombination, and  $Ar^+$  generated by the plasma can participate as a catalyst as well as  $Li$ .

We have assumed that Doppler broadening due to thermal motion was the dominant source to the extent that other sources may be neglected. This assumption was confirmed when each source was considered. In general, the experimental profile is a convolution of two Doppler profiles, an instrumental profile, the natural (lifetime) profile, Stark profiles, van der Waals profiles, a resonance profile, and fine structure. The contribution from each source was determined to be below the limit of detection [13-21, 38-39].

The formation of fast  $H$  can be explained by a resonant energy transfer from hydrogen atoms to  $Li$  atoms, of three times the potential energy of atomic hydrogen, to form a short-lived intermediate  $H^*(1/4)$  having a central field equivalent to four times that of a proton and a radius of the hydrogen atom. The intermediate spontaneously decays by a collisional or through-space energy transfer as the radius decreases to  $a_0/4$  yielding fast  $H(n=1)$ , as well as the emission of  $q \cdot 13.6 eV$  photons reported previously [27-29]. Collisional energy transfer including through-space coupling is common. For example, the exothermic chemical reaction of  $H + H$  to form  $H_2$  does not occur with the emission of a photon. Rather, the reaction requires a collision with a third body,  $M$ , to remove the bond energy- $H + H + M \rightarrow H_2 + M^*$  [45]. The third body distributes the energy from the exothermic reaction, and the end result is the  $H_2$  molecule and an increase in the temperature of the system. In the case of the catalytic reaction with the formation of states given by Eqs. (2a) and (2c), the temperature of  $H$  becomes very high.

**B. Differential Scanning Calorimetry (DSC) Measurements.** The DSC (100-750 °C) of  $NaH$  is shown in Figure 7. A broad endothermic peak was observed at 350°C to 420 °C which corresponded to  $47 kJ/mole$ . Sodium hydride decomposes in this temperature range with a corresponding enthalpy of  $57 kJ/mole$  [72]. A large exotherm was observed in the region 640°C to 825 °C which corresponded to  $-177 kJ/mole$ . The DSC (100-750 °C) of  $MgH_2$  is shown in Figure 8. Two sharp endothermic peaks were observed. A first peak was observed centered at 351.75 °C corresponding to  $68.61 kJ/mole MgH_2$ . The decomposition of  $MgH_2$  is observed at 440°C to 560 °C corresponding to  $74.4 kJ/mole MgH_2$  [72]. In Figure 8, a second peak was observed centered at 647.66 °C corresponding to  $6.65 kJ/mole MgH_2$ . The known melting point of  $Mg(m)$  is 650 °C corresponding to an enthalpy of fusion of  $8.48 kJ/mole Mg(m)$  [73]. Thus, the expected behavior was observed for the decomposition of a control, noncatalyst hydride. In contrast, a novel exothermic effect of  $-177 kJ/mole NaH$  or at least  $-354 kJ/mole H_2$  was observed under conditions that form  $NaH$  catalyst with some portion of the  $H$  undergoing the catalysis reactions given by Eqs. (23-25). The observed enthalpy was greater than that of the most exothermic reaction possible for  $H$ , the  $-241.8 kJ/mole H_2$  enthalpy of combustion of hydrogen.

**C. Water-Flow Calorimetry Power Measurements.** In each test, the energy input and energy output were calculated by integration of the corresponding power. For the input power, the voltage and current measured at the end of each time interval were multiplied by the time interval (typically 10 seconds) to obtain the energy increment in Joules. All energy increments

were summed over the entire experiment after the equilibration period to obtain total energy. For output energy, the thermistor offset was calculated after each test assuming that the final readings of inlet and outlet temperature were identical. This offset was calculated to be 0.036 °C. The thermal energy in the coolant flow in each time increment was calculated using Eq. (39) by multiplying volume flow rate of water by the water density at 19 °C (0.998 kg/liter), the specific heat of water (4.181 kJ/kg °C), the corrected temperature difference, and the time interval. Values were summed over the entire experiment to obtain the total energy output. The total energy from the cell  $E_T$  must equal the energy input  $E_{in}$  and any excess energy  $E_{ex}$ :

$$E_T = E_{in} + E_{ex} \quad (43)$$

From the energy balance, any excess heat was determined.

The calibration test results are shown in Figures 9 and 10. In the plot of Figure 10, there is a time point at which the slope of the coolant power changes almost discontinuously. This point at about one hour corresponds to the helium addition enhancing heat transfer from the cell to the chamber wall. The numerical integration of the input and output power curves yielded an output energy of 292.2 kJ and an input energy of 303.1 kJ corresponding to a coupling of flow of 96.4% of the resistive input to the output coolant.

The cell temperature with time and the coolant power with time for the hydrino reaction with the cell containing the reagents comprising the catalyst material, 1g *Li*, 0.5g *LiNH<sub>2</sub>*, 10g *LiBr*, and 15g *Pd/Al<sub>2</sub>O<sub>3</sub>* are shown in Figures 11 and 12, respectively. The numerical integration of the input and output power curves with the calibration correction applied yielded an output energy of 227.2 kJ and an input energy of 208.1 kJ. Thus, from Eq. (43), the excess energy was 19.1 kJ. In the plot of Figure 12, there is a point at which the slope of the temperature changes almost discontinuously. The slope change occurs just slightly after 1 hour, and this corresponds to the cell temperature rising rapidly with the onset of reaction. Based on the system response to a power pulse, the excess energy of 19.1 kJ occurred in less than 2 minutes which places the power for the reaction at over 160 W.

The quantitative XRD of the composition of the products following the reaction showed that the *LiBr* and *Pd/Al<sub>2</sub>O<sub>3</sub>* were unchanged. Thus, assuming a 100% yield, the maximum theoretical energy released by known chemistry is 4.3 kJ from the formation of lithium nitride and hydride according to Eq. (22); whereas, the observed energy balance was 4.4 times this maximum. The 100% yield is conservative since the output matched the input energy in the case of the control, 1g *Li* and 0.5g *LiNH<sub>2</sub>*. The only exothermic reaction possible to account for the energy balance is that given by Eqs. (17-19). The hydrogen content of the 0.5g *LiNH<sub>2</sub>* was 22 mmoles *H<sub>2</sub>*. Thus, the observed energy balance is  $-870 \text{ kJ/mole } H_2$ , over 3.5 times the  $-241.8 \text{ kJ/mole } H_2$  enthalpy of combustion, the most energetic reaction of hydrogen assuming the maximum possible *H<sub>2</sub>* inventory.

The cell temperature with time and the coolant power with time for the R-Ni control power test with the cell containing the reagents comprising the starting material for R-Ni, 15g R-Ni/Al alloy powder, and 3.28g of Na are shown in Figures 13 and 14, respectively. The temperature and coolant power time profiles curves were very similar to the calibration. The numerical integration of the input and output power curves with the calibration correction applied yielded an output energy of 384 kJ and an input energy of 385 kJ. Energy balance was obtained.

The cell temperature with time and the coolant power with time for the hydrino reaction with the cell containing the reagents comprising the catalyst material, 15g *NaOH*-doped R-Ni, and 3.28g of Na are shown in Figures 15 and 16, respectively. The numerical integration of the input and output power curves with the calibration correction applied yielded an output energy of 185.1 kJ and an input energy of 149.1 kJ. Thus, from Eq. (43), the excess energy was 36 kJ. In the plot of Figure 15, there is a point at which the slope of the temperature changes almost discontinuously. The slope change occurs just slightly before 1 hour, and this corresponds to the cell temperature rising rapidly with the onset of reaction. Based on the system response to a power pulse, the excess energy of 36 kJ occurred in less than 1.5 minutes that places the power for the reaction at over 0.5 kW.

The composition of the reactant *NaOH*-doped R-Ni and the product following the reaction with the alkali metal determined by quantitative XRD was Ni with trace Bayerite and Ni with trace alkali hydroxide, respectively. The formation of a sodium-Ni alloy or the reaction of sodium with  $Al_2O_3$  of R-Ni [74-75] is significantly endothermic ( $\Delta H = +138 \text{ kJ / mole Na}$  [76] and  $\Delta H = +72.18 \text{ kJ / mole Na}$  [66], respectively). Using the heat of formations, the reaction of Bayerite with sodium to form *NaOH* ( $\Delta H = -15.6 \text{ kJ / mole Al(OH)}_3$  [66, 77]) contributes negligibly to the energy balance based on the XRD analysis showing trace Bayerite initially and the corresponding *NaOH* product from reaction with *Na*. Consistent with the literature [75], the  $H_2O$  content from Bayerite decomposition was 47.7  $\mu$  moles  $H_2O$ /g R-Ni corresponding to a negligible contribution due to the formation of *NaOH* ( $\Delta H = -184.0 \text{ kJ / mole H}_2O$  [66]) from the decomposition of  $Al(OH)_3$  ( $2Al(OH)_3 \rightarrow Al_2O_3 + 3H_2O$   $\Delta H = +92.45 \text{ kJ / mole Al}$ ). The overall reaction is the reaction of Bayerite with sodium to form *NaOH* ( $\Delta H = -15.6 \text{ kJ / mole Al(OH)}_3$ ).

The only exothermic reaction possible to account for the energy balance is that given by Eqs. (23-25). The hydrogen content of the R-Ni determined using quantitative GC and by using the ideal gas law on the measured P, V, and T was 150  $\mu$  moles  $H_2$ /g R-Ni. Thus, the observed energy balance is  $-1.6 \times 10^4 \text{ kJ / mole H}_2$ , over 66 times the  $-241.8 \text{ kJ / mole H}_2$  enthalpy of combustion, the most energetic reaction of hydrogen assuming the maximum possible  $H_2$  inventory. The conservative theoretical energy yield for the reaction of Eq. (44) is 259 eV/ $H_2$  or 25 MJ/mole $H_2$  (Eq. (7)).



Among the most energetic known oxidation reactions involving a solid fuel is the reaction  $Be + 1/2O_2 \rightarrow BeO$ , which has a heat of combustion of 24 kJ/g, and there are very few known fuel/oxidizer systems producing greater than 10 kJ/g [66]. As a comparison, even without possibly going to completion, the H content of the recyclable catalyst *NaH* produced energy of over 300 times that of the best known solid fuel per weight.

With increased *NaOH* doping and a switch to R-Ni 2400, the catalytic material generated high power and energy without requiring the addition of *Na*. The cell temperature with time and the coolant power with time for the hydrino reaction with the cell containing the catalyst material, 15g *NaOH*-doped R-Ni 2400, are shown in Figures 17 and 18, respectively. The numerical integration of the input and output power curves with the calibration correction

applied yielded an output energy of 195.7 kJ and an input energy of 184.0 kJ corresponding to an excess energy of 11.7 kJ, and the power was over 0.25 kW.

The composition of the (1) control 3wt%  $Al(OH)_3$  doped  $Ni/Al$  alloy, (2) the reactant  $NaOH$  -doped R-Ni, and (3) the R-Ni product following the reaction determined by quantitative XRD was (1) 47.1 wt%  $NiAl_3$ , 49.91 wt%  $Ni_2Al_3$ , 2.7 wt%  $Al(OH)_3$ , and 0.4 wt%  $Al$ , (2) R-Ni with 3.7wt% Bayerite and (3) 100 wt% R-Ni, respectively. The measured  $H_2O$  content from Bayerite decomposition of the initial R-Ni was 32.8  $\mu$  moles  $H_2O/g$  R-Ni compared to the measured  $H_2O$  content from Bayerite decomposition of 34.0  $\mu$  moles  $H_2O/g$  for 3 wt%  $Al(OH)_3$  doped  $Ni/Al$  alloy. The most exothermic reaction possible was the reaction of  $Al(OH)_3$  to  $Al_2O_3$ . The balanced reaction is given by [66, 76, 78]:



For 3.7wt%  $Al(OH)_3$ , the maximum theoretical energy from the reaction given by Eq. (45) is  $\Delta H = -1.88 \text{ kJ}$ . This was confirmed by the heat measurement of 15g of 3 wt%  $Al(OH)_3$  doped  $Ni/Al$  alloy that showed an average energy of  $\Delta H = -1.1 \text{ kJ}$  compared to the theoretical energy of  $\Delta H = -1.7 \text{ kJ}$  ( $\Delta H = -300 \text{ kJ / mole } Al(OH)_3$  using Eq. (45) with  $\Delta H_f(NiAl_{crystal}) = -96 \text{ kJ/mole}$  [76]). Thus, the observed energy from the  $NaOH$  -doped R-Ni was 4.4 times the theoretical; thus, it was predominantly attributable to the catalysis reaction given by Eqs. (23-25).

The energy scaled linearly and the power increased nonlinearly wherein the reaction of 1 kg 0.5 wt%  $NaOH$  -doped R-Ni liberated 753.1 kJ of energy to develop a system-response-corrected peak power in excess of 50 kW. The scale-up cell calibration test results are shown in Figures 19 and 20. The numerical integration of the input and output power curves yielded an output energy of 3284.1 kJ and an input energy of 3292.1 kJ corresponding to a coupling of flow of 99.76% of the resistive input to the output coolant. The cell temperature with time and the coolant power with time for the hydrino reaction with the scale-up cell containing the catalyst material, 1 kg 0.5wt%  $NaOH$  -doped R-Ni 2400, are shown in Figures 21 and 22, respectively. The numerical integration of the input and output power curves yielded an output energy of 2149.1 kJ and an input energy of 1396 kJ corresponding to an excess energy of 753.1 kJ, and the cell developed a power in excess of 50 kW.

**D. ToF-SIMS Spectra.** The positive ToF-SIMS spectrum obtained from  $LiBr$  and the  $LiH * Br$  crystals are shown in Figures 23 and 24, respectively. The positive ion spectrum of the  $LiH * Br$  crystals and that of the  $LiBr$  control were dominated by the  $Li^+$  ion.  $Li_2^+$ ,  $Na^+$ ,  $Ga^+$ , and  $Li(LiBr)^+$  were also observed.

The negative ion ToF-SIMS of  $LiBr$  and the  $LiH * Br$  crystals are shown in Figures 25 and 26, respectively. The  $LiH * Br$  spectrum was dominated by  $H^-$  and  $Br^-$  peaks with the intensity of  $H^- > Br^-$ . Bromide alone dominated the negative ion ToF-SIMS of the  $LiBr$  control. For both,  $O^-$ ,  $OH^-$ ,  $Cl^-$ , and  $LiBr^-$  were also observed. In addition to the increased

hydride, other unique peaks of the  $LiH * Br$  sample were  $LiHBr^-$  and  $Li_2H_2Br^-$  consistent with the formation of novel lithium bromohydride.

The positive ToF-SIMS spectrum obtained from  $LiI$  and the  $LiH * I$  crystals are shown in Figures 27 and 28, respectively. The positive ion spectrum of the  $LiH * I$  crystals and that of the  $LiI$  control were dominated by the  $Li^+$  ion.  $Li_2^+$ ,  $Na^+$ ,  $Ga^+$ , and a series of positive ions  $Li[LiI]_n^+$  were also observed. Unique peaks of the  $LiH * I$  sample were  $LiHI^+$ ,  $Li_2H_2I^+$ ,  $Li_4H_2I^+$ , and  $Li_6H_2I^+$ .

The negative ion ToF-SIMS of  $LiI$  and the  $LiH * I$  crystals are shown in Figure 29 and 30, respectively. The  $LiH * I$  spectrum was dominated by  $H^-$  and  $I^-$  peaks with the intensity of  $H^- > I^-$ . Iodide alone dominated the negative ion ToF-SIMS of the  $LiI$  control. For both,  $O^-$ ,  $OH^-$ ,  $Cl^-$ , and a series of negative ions  $I[LiI]_n^-$  were also observed. In addition to the increased hydride, other unique peaks of  $LiH * I$  sample were  $LiHI^-$ ,  $Li_2H_2I^-$ , and  $NaHI^-$  consistent with the formation of novel lithium iodohydride.

The negative ToF-SIMS spectrum ( $m/e = 20-30$ ) of  $NaH^*$ -coated  $Pt/Ti$  following the production of 15 kJ of excess heat is shown in Figure 31. Hydrino-hydride-compound series  $NaH_x^-$  was observed wherein the mass deficit from the high resolution (10,000) mass determination definitively distinguished this assignment over the  $C_2H_x^-$  series observed in controls. The XPS spectrum showed that  $NaH^*$ -coated  $Pt/Ti$  comprised two fractional hydrogen states,  $H^-(1/3)$  and  $H^-(1/4)$  (Sec. IIIF).

$NaH_x^-$  having the mass-deficit series was also observed in the spectrum of R-Ni from the Na/R-Ni water-flow calorimetric run that produced 36 kJ of excess heat. The positive ToF-SIMS spectrum obtained from R-Ni reacted over a 48 hour period at 50°C is shown in Figure 32. The dominant ion on the surface was  $Na^+$  consistent with  $NaOH$  doping of the surface. The ions of the other major elements of R-Ni 2400 such as  $Al^+$ ,  $Ni^+$ ,  $Cr^+$ , and  $Fe^+$  were also observed.

The negative ion ToF-SIMS of R-Ni reacted over a 48 hour period at 50°C is shown in Figure 33. The spectrum showed a very large  $H^-$  peak as well as hydroxide fragments  $OH^-$  and  $O^-$ . Two other dominant peaks matched the high resolution mass of  $NaH_3^-$  and  $NaH_3NaOH^-$  to 10,000 and were assigned to sodium hydrino hydride and this ion in combination with  $NaOH$ . Other unique ions assignable to sodium hydrino hydrides  $NaH_x^-$  in combinations with  $NaOH$ ,  $NaO$ ,  $OH^-$  and  $O^-$  were observed.

**E. NMR Identification of  $H^-(1/3)$ ,  $H^-(1/4)$ ,  $H_2(1/3)$  and  $H_2(1/4)$ .** The  $^1H$  MAS NMR spectra of  $LiH * Br$  and  $LiH * I$  relative to external TMS are shown in Figures 34A and 34B, respectively.  $LiH * X$  samples showed a large distinct upfield resonance at -2.51 ppm and -2.09 ppm for  $X = Br$  and  $X = I$ , respectively. None of the controls comprising  $LiH$ , equal molar mixtures of  $LiH$  and  $LiBr$  or  $LiI$ ,  $LiNH_2$ ,  $Li_2NH$ , and equal molar mixtures of  $LiNH_2$  or  $Li_2NH$  and  $LiBr$  or  $LiI$  showed an upfield-shifted peak. Since the upfield peak of  $LiH * X$

at about  $-2.2$  ppm was very broad, it is useful to compare these results to those of the prior identification of  $H^-(1/4)$  of  $KH^*Cl$  and  $KH^*I$ .

The  $^1H$  MAS NMR spectra relative to TMS of  $KH^*Cl$  samples (Figure 35A) from independent syntheses and controls were given previously [13-15, 24-26]. The experimental absolute resonance shift of TMS is  $-31.5$  ppm relative to the proton's gyromagnetic frequency [79-80]. The  $KH$  experimental shift of  $+1.1$  ppm relative to TMS corresponding to absolute resonance shift of  $-30.4$  ppm matches very well the predicted shift of  $H^-(1/1)$  of  $-30$  ppm given by Eq. (4) wherein  $p = 0$ . The novel peak at  $-4.46$  ppm relative to TMS corresponding to an absolute resonance shift of  $-35.96$  ppm indicates that  $p = 4$  in Eq. (4).  $H^-(1/4)$  is the hydride ion predicted by using  $K$  as the catalyst [1, 15, 30]. Furthermore, the extraordinarily narrow peak-width is indicative of a small hydride ion that is a free rotator. In contrast,  $KH^*I$  (Figure 35B) shows a very broad peak at  $-2.31$  ppm. The predicted product hydride ion  $H^-(1/4)$  of the reaction with  $K$  catalyst to form  $KH^*I$  was observed by XPS [13-15, 26, 30] at its predicted binding energy of  $11.2$  eV. Thus, the diamagnetic shift due to the larger halide is  $+2.15$  ppm. The corrected upfield NMR peaks for  $LiH^*X$  are each about  $-4.46$  ppm which matches the predicted shift of the free ion given by Eq. (4).

The elemental analysis of  $LiH^*Br$  by wt% was Li (8%), H (1.1%), Br (90.9%) corresponding stoichiometrically to  $LiHBr$  with the stainless steel and R-Ni components at less than detectable levels. The elemental analysis of  $LiH^*I$  by wt% was Li (5.2%), H (0.8%), I (94%) corresponding stoichiometrically to  $LiHI$  with the stainless steel and R-Ni components at less than detectable levels. Thus, no hydrides other than those of Li are possible assignments. U-H does not have an upfield-shifted NMR peak as determined previously [13-14]. F centers could not have been the source since no ESR signal was detectable in  $LiH^*Br$  or  $LiH^*I$  at room temperature or  $77$  K.  $^1H$  MAS NMR spectra obtained on  $LiNH_2$ ,  $Li_2NH$ , and these compounds in a  $LiBr$  or  $LiI$  matrix also showed that neither of these compounds have an upfield-shifted NMR peak. To further eliminate  $LiNH_2$  and  $Li_2NH$  as the source of the  $-2.5$  ppm peak,  $LiH^*Br$  samples with the  $-2.5$  ppm peak were heated to  $>600^\circ C$  under dynamic vacuum to decompose  $LiNH_2$  and  $Li_2NH$ . The heat-treated samples were analyzed by FTIR spectroscopy to confirm that the amide and imide were eliminated as indicated by the absence of the amide peaks at  $3314$ ,  $3259$ ,  $2079$ (broad),  $1567$ , and  $1541$   $cm^{-1}$  and the imide peaks at  $3172$  (broad),  $1953$ , and  $1578$   $cm^{-1}$  while the  $-2.5$  ppm peak remained upon reanalysis by NMR. The FTIR spectrum shown in Figure 57B shows the elimination of these species while the corresponding NMR showed the  $-2.5$  ppm peak. Since the past and present NMR and FTIR analysis leads to the conclusion that the  $-2.5$  ppm peak in  $^1H$  NMR spectrum is not associated with the U H,  $LiNH_2$ ,  $Li_2NH$ , or any other known species, the  $-2.5$  ppm peak in  $^1H$  NMR spectrum is assigned to the  $H^-(1/4)$  ion which matches theoretical prediction and is direct evidence of a lower-energy state hydride ion.

In addition to the  $-2.5$  ppm and  $-2.09$  ppm peaks assigned to  $H^-(1/4)$ , a  $1.3$  ppm peak was observed in the  $^1H$  MAS NMR spectra of  $LiH^*Br$  and  $LiH^*I$  shown in Figures 34A and 34B, respectively. None of the controls showed this peak which eliminated any of the starting compounds or their possible known products. However, the peak may be due to the  $H_2(1/4)$  molecule corresponding to  $H^-(1/4)$ .

$H_2$  has been characterized by gas-phase  $^1H$  NMR. The experimental absolute resonance shift of gas-phase TMS relative to the proton's gyromagnetic frequency is  $-28.5$  ppm [81].  $H_2$  was observed at  $0.48$  ppm compared to gas phase TMS set at  $0.00$  ppm [82]. Thus, the corresponding absolute  $H_2$  gas-phase resonance shift of  $-28.0$  ppm ( $-28.5 + 0.48$ ) ppm was in excellent agreement with the predicted absolute gas-phase shift of  $-28.01$  ppm given by Eq. (12).

The absolute  $H_2$  gas-phase shift can be used to determine the matrix shift for  $H_2$  in a lithium-compound matrix. The correction for the matrix shift can then be applied to the  $1.3$  ppm peak to determine the gas-phase absolute shift to compare to Eq. (12). The shifts of all of the peaks were relative to liquid-phase TMS which has an experimental absolute resonance shift of  $-31.5$  ppm relative to the proton's gyromagnetic frequency [79-80]. The experimental shift of  $H_2$  in a lithium-compound matrix of  $4.06$  ppm relative to liquid-phase TMS is shown in Figure 7 of Lu et al. [83] and corresponds to an absolute resonance shift of  $-27.44$  ppm ( $-31.5$  ppm +  $4.06$  ppm). Using the absolute  $H_2$  gas-phase resonance shift of  $-28.0$  ppm corresponding to  $3.5$  ppm ( $-28.0$  ppm  $-31.5$  ppm) relative to liquid TMS, the lithium-compound matrix effect is  $+0.56$  ppm ( $4.06$  ppm  $-3.5$  ppm) requiring a correction of the measured shift of  $-0.56$  ppm. Then, the peak upfield of  $H_2$  at  $1.26$  ppm peak relative to TMS corresponds to a matrix-corrected absolute resonance shift of  $-30.8$  ppm ( $-31.5$  ppm +  $1.26$  ppm  $-0.56$  ppm). Using Eq. (12), the data indicates  $p = 4$  and matches  $H_2(1/4)$ :

$$\begin{aligned}\frac{\Delta B_T}{B} &= -(28.01 + 0.64p) \text{ ppm} \\ &= -(28.01 + 0.64(4)) \text{ ppm} \\ &= -30.6 \text{ ppm}\end{aligned}\tag{46}$$

Lu et al. [83] also observed a peak at this position that increased in intensity relative to  $H_2$  with the duration of in situ heating of  $LiH + LiNH_2$  (1.1/1). They were unable to assign the peak labeled unknown in their Figures 6 and 7. The assignment of the peak that matched the theoretical shift of  $H_2(1/4)$  extremely well was confirmed by FTIR (Sec. IIIG) and electron beam-excitation emission spectroscopy (Sec. IIIH).

The presence of the  $H^-(1/4)$  ion in  $LiH * X$  was found to depend on the polarizability of the halide ion. The  $^1H$  MAS NMR spectra of  $LiH * F$  and  $LiH * Cl$  are shown in Figures 36A and 36B, respectively. Peaks at  $4.3$  ppm and  $1.2$  ppm matched theoretical predictions of molecular hydrogen in two different quantum states [1, 6]. The  $4.3$  ppm peak matched the assignment of Lu et al. [83] for  $H_2$ , and the  $1.2$  ppm peak labeled unknown by Lu et al. [83] matched  $H_2(1/4)$ . The  $H_2(1/4)$  assignment was confirmed by the observation of the predicted rotational transition in the FTIR spectrum (Sec. IIIG) and the predicted rotational spacing by electron beam-excitation emission spectroscopy (Sec. IIIH). The  $H^-(1/4)$  ion peak was absent in  $LiH * F$  comprising a nonpolarizable fluorine as well as in  $LiH * Cl$  comprising a nonpolarizable chlorine; whereas, it was the dominant peak in both  $LiH * Br$  and  $LiH * I$  as shown in Figures 34A and 34B, respectively. These results indicate that a polarizable halide is required for  $LiX$  to react with the  $H^-(1/4)$  ion to form the corresponding lithium halidohydride. Since molecular species are nonspecifically trapped in the crystalline lattice, the

H-content selectivity of  $LiH * X$  for molecular species alone or in combination with  $H^-(1/4)$  ions is based on the polarizability of the halide and the corresponding reactivity towards  $H^-(1/4)$ . Potassium catalyst formed  $H_2(1/4)$  as well, but in  $KCl$  and  $KI$  matrices with  $H^-(1/4)$ , as shown in Figures 35A and 35B.

The  $^1H$  MAS NMR spectra of  $NaH * Br$  relative to external TMS is shown in Figure 37.  $NaH * Br$  showed a large distinct upfield resonance at  $-3.58$  ppm. None of the controls comprising  $NaH$  or equal molar mixtures of  $NaH$  and  $NaBr$  showed an upfield-shifted peak. The  $-3.58$  ppm upfield peak of  $NaH * Br$  was broadened, but not significantly as in the case of  $KH * I$ ; thus, the matrix may not have as large an effect as in the prior case of the identification of  $H^-(1/4)$  in  $KH * I$ . Thus, the measured shift is directly compared to theory with the expectation that it is the peak shifted downfield due to the matrix effect. The experimental absolute resonance shift of TMS is  $-31.5$  ppm relative to the proton's gyromagnetic frequency [79-80]. The novel peak at  $-3.58$  ppm relative to TMS corresponding to an absolute resonance shift of  $-35.08$  ppm indicates that  $p = 4$  in Eq. (4).  $H^-(1/4)$  is the favored hydride ion predicted by using  $NaH$  as the catalyst (Eqs. (3-4) and (23-27)). Similar to the case of  $LiH * X$ , the  $4.3$  ppm peak shown in Figure 37 is assigned to  $H_2$ , and the  $1.13$  ppm peak is assigned to  $H_2(1/4)$ . The latter is commonly observed as a favored catalysis molecular product [29].

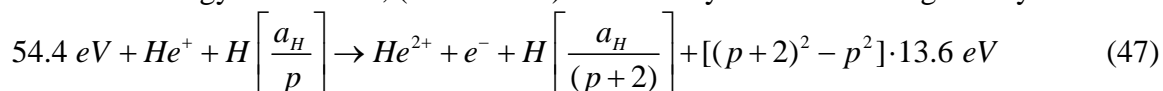
$NaH * Cl$   $^1H$  MAS NMR spectra relative to external TMS showing the effect of hydrogen addition on the relative intensities of  $H_2$ ,  $H_2(1/4)$ , and  $H^-(1/4)$  is shown in Figures 38A-B. The addition of hydrogen increased the  $H^-(1/4)$  peak and decreased the  $H_2(1/4)$  while the  $H_2$  increased. (A)  $NaH * Cl$  synthesized with hydrogen addition showing a  $-4$  ppm upfield-shifted peak assigned to  $H^-(1/4)$ , a  $1.1$  ppm peak assigned to  $H_2(1/4)$ , and a dominant  $4$  ppm peak assigned to  $H_2$ . (B)  $NaH * Cl$  synthesized without hydrogen addition showing a  $-4$  ppm upfield-shifted peak assigned to  $H^-(1/4)$ , a dominant  $1.0$  ppm peak assigned to  $H_2(1/4)$ , and a small  $4.1$  ppm assigned to  $H_2$ .

The effect of hydrogen addition on the relative  $^1H$  MAS NMR intensities of  $H_2$ ,  $H_2(1/4)$ , and  $H^-(1/4)$  in  $NaH * Cl$  is shown in Figures 38A-B. The dominant peak switched from being  $H_2$  to  $H_2(1/4)$  with the addition of external hydrogen indicating that  $H_2$  may occupy sites in the lattice that are filled by  $H_2(1/4)$  when  $H_2$  is less abundant. However, the addition of hydrogen increased the relative intensity of the  $H^-(1/4)$  peak, most likely by increasing the hydrino reactant concentration.  $NaH * Cl$  can also be synthesized using a solid source of H rather than gaseous hydrogen addition. The  $^1H$  MAS NMR spectrum of  $NaH * Cl$  from reaction of  $Na$ ,  $NaCl$ , and the solid H source  $NH_4Cl$  is shown in Figure 39. The upfield-shifted  $H^-(1/4)$  peak and the  $H_2(1/4)$  peak were observed at  $-3.84$  ppm and  $1.17$  ppm, respectively, in the absence of the  $H_2$  peak. Similarly, the  $^1H$  MAS NMR spectrum of

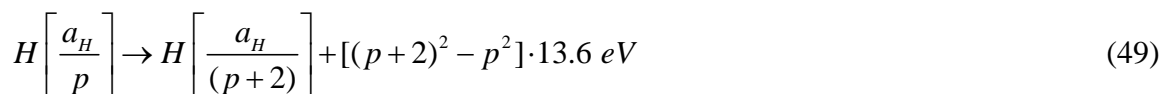
$NaH * Br$  from reaction of  $Na$ ,  $NaBr$ , and the solid H source  $NH_4Br$  is shown in Figure 40. The upfield-shifted  $H^-(1/4)$  peak and the  $H_2(1/4)$  peak were observed at  $-3.56$  ppm and  $1.23$  ppm, respectively, in the absence of the  $H_2$  peak.

NMR was then performed on  $NaH * Cl$  synthesized from  $NaCl$  and the solid acid  $KHSO_4$  as the only source of hydrogen to test whether  $H^-(1/3)$  formed by the reactions of Eqs. (23-25) could be observed when the rapid reaction to  $H^-(1/4)$  according to Eq. (27) was partially inhibited due to the absence of a high concentration of  $H$  from a dissociator with  $H_2$  or a hydride. The  $^1H$  MAS NMR spectrum of  $NaH * Cl$  formed using the solid acid relative to external TMS is shown in Figure 41. Peaks at  $-3.97$  ppm and  $1.15$  ppm matched the  $-4$  ppm and  $1.1$  ppm peaks of Figures 39A-B that were assigned to  $H^-(1/4)$  and  $H_2(1/4)$ , respectively, of  $NaH * Cl$  synthesized using  $H$  from a dissociator with  $H_2$  or a hydride. The close match was expected since the  $KHSO_4$  was only 6.5 mole% of the mixture with  $NaCl$  such that the matrix effect was essentially constant between samples. Uniquely, another set of peaks at  $-3.15$  ppm and  $1.7$  ppm was observed for the solid-acid product. Using Eqs. (4) and (12) with the matrix shift given previously for  $NaH * Cl$ , these peaks matched and were assigned to  $H^-(1/3)$  and  $H_2(1/3)$ , respectively. Curve fitting of two peaks put the peaks at about  $-3$  ppm and  $-4$  ppm, the theoretical values with experimental error. Thus, both fractional hydrogen states were present, and the  $H_2$  peak was absent at  $4.3$  ppm due to the synthesis of  $NaH * Cl$  using a solid acid as the only  $H$  source that confirms the reactions given by Eqs. (23-30). The presence of  $H^-(1/4)$  and  $H_2(1/4)$  in  $NaH * Cl$  from reaction of  $NaCl$  and the solid acid  $KHSO_4$  was confirmed by XPS and electron beam-excitation emission spectroscopy.

Helium is another catalyst that can cause a transition reaction to  $\left[\frac{a_H}{3}\right]$  because the second ionization energy is  $54.4 eV$ , ( $2 \cdot 27.2 eV$ ). The catalyst reactions are given by



And, the overall reaction is



As in the case of the  $NaH$  catalyst reaction, the subsequently rapid transition of the  $He^+$  catalysis product  $\left[\frac{a_H}{3}\right]$  to  $\left[\frac{a_H}{4}\right]$  may occur via further catalysis by atomic hydrogen that accepts  $27.2 eV$  from  $\left[\frac{a_H}{3}\right]$  as given by Eq. (27). Characteristic continuum emission starting at  $30.4$  nm and continuing to longer wavelengths is predicted for this transition reaction as the energetic hydrino intermediate decays. The emission has been observed by EUV spectroscopy recorded on microwave discharges of helium with 2% hydrogen [44]. The spectroscopic and

NMR data provide strong support for the catalyst mechanism of the formation of  $\left[\frac{a_H}{3}\right]$  with the subsequent transition to  $\left[\frac{a_H}{4}\right]$ . Additional evidence is the observation of both  $H^-(1/3)$  and  $H^-(1/4)$  in  $NaH * Cl$  as given in Sec. IIIF.

The  $^1H$  MAS NMR spectrum of  $NaH * F$  is shown in Figure 42. The  $H_2(1/4)$  and  $H_2$  peaks at 1.13 ppm and 4.3 ppm, respectively, were unshifted, and the upfield-shifted peak in  $NaH * F$  was observed at  $-0.18$  ppm. As shown in the case of the  $LiH * X$  series, typically the polar anion favors the incorporation of predominantly  $H_2(1/4)$  as the hydrino-type product. With a change to a  $Na$  cation and a higher temperature during synthesis,  $H_2(1/4)$  and, additionally, an upfield  $-$ shifted peak were observed. The lattice spacing of  $NaF$  is the smallest of the  $Na$  halides; thus, the positive-ion crystal field of  $NaF$  will influence  $H^-(1/4)$  the most in the series  $NaX$  ( $X = F, Cl, Br, I$ ). Thus, it was considered that the  $-0.18$  ppm peak in  $NaH * F$  was  $H^-(1/4)$  shifted down field by the  $Na^+$  field due to the near approach of these cations to  $H^-(1/4)$  in the unit cell. This was tested by dissolving  $NaH * F$  in DMF and running solution NMR to record the spectrum on isolated species.

The  $^1H$  NMR of  $NaH * F$  dissolved in DMF-d7 (Figure 43) showed  $H_2(1/4)$  and  $H^-(1/4)$  peaks at 1.2 ppm and  $-3.86$  ppm, respectively. The other peaks in the spectrum shown in Figure 43 are due to DMF except for the 3.46 ppm peak which is due to water. Note that the water peak has no  $^{13}C$  side-bands. The 1.2 ppm peak is also absent  $^{13}C$  side-bands which eliminates hydrocarbon as an assignment. In addition, the high intensity served to eliminate  $NaH$  as the source of the 1.2 ppm peak since  $NaH$  reacts rapidly with water to completion. This was shown in control studies by the disappearance of the sharp singlet peak of  $NaH$  at 1.35 ppm with an increase in the  $H_2O$  peak wherein the only analyte peaks of the controls were the  $NaH$  peak and the sharp singlet  $H_2$  peak at 4.55 ppm due to the reaction of  $NaH$  with water in DMF.  $NaH$  was also unexpected in  $NaH * F$  since the synthesis reaction was run at  $550^\circ C$  which is above the  $350^\circ C$  decomposition temperature of  $NaH$  [54] and the final pressure was vacuum. In addition to the presence of a free hydride ion in a water mixture that is indicative of the remarkable stability of  $H^-(1/4)$ , another distinguishable feature of the solution NMR of the hydrino products is the width of the peaks. The latter is indicative of strong interactions of  $H_2(1/4)$  and  $H^-(1/4)$  with the solution that is expected especially for the negative-charged hydride ion further involving the positive counterion  $Na^+$ . Applicable relaxation interactions with the solution that effect the line width such as nuclear magnetic dipole interactions due to high mobility, spin rotational interaction ( $H_2(1/4)$ ), and scalar relaxation ( $H^-(1/4)$ ) are given in Becker [84].

The solution-phase NMR provides a definitive test of the theoretically predicted chemical shifts. Using Eq. (46) and the experimental absolute resonance shift of TMS,  $-31.5$  ppm, the predicted gas-phase shift of  $H_2(1/4)$  is

$$\frac{\Delta B_T}{B} = -30.6 \text{ ppm} - (-31.5 \text{ ppm}) = 0.9 \text{ ppm} \quad (50)$$

which is very close to the observed shift of 1.2 ppm (Figure 43), and this peak-position is also in good agreement with the  $^1\text{H}$  MAS NMR value of 1.13 ppm observed for  $\text{H}_2(1/4)$  in  $\text{NaH} * \text{F}$  as shown in Figure 42. Furthermore, the experimental absolute  $\text{H}_2$  gas-phase resonance shift of -28.0 ppm is in excellent agreement with the predicted absolute gas-phase shift of -28.01 ppm (Eq. (12)) as given in Sec. III E.

Similarly, excellent agreement is found between the theoretical and experimental shifts in the case of  $\text{H}^-(1/4)$ . Using Eq. (4) with  $p = 4$  and the experimental absolute resonance shift of TMS, -31.5 ppm, the predicted gas-phase shift of  $\text{H}^-(1/4)$  is

$$\begin{aligned} \frac{\Delta B_T}{B} &= -(29.9 + 1.37(4)) \text{ ppm} - (-31.5 \text{ ppm}) \\ &= -35.38 \text{ ppm} - (-31.5 \text{ ppm}) \\ &= -3.88 \text{ ppm} \end{aligned} \quad (51)$$

which is extraordinarily close to the observed shift of -3.86 ppm (Figure 43). Theoretical accuracy is also found for ordinary  $\text{H}^-$ . Using Eq. (4) and the experimental absolute resonance shift of TMS, -31.5 ppm, the predicted gas-phase shift of  $\text{H}^-$  is 1.6 ppm compared to the observed value of 1.35 ppm. ToF-SIMS which has a detection limit below the parts per million (ppm) level showed no metals other than alkali metals. The positive ToF-SIMS spectrum showed  $\text{H}$ ,  $\text{Na}$ ,  $\text{Na}_2$ ,  $\text{Na}_n\text{F}_{n-1}$ ,  $(\text{NaH})_3\text{F}_3$ , and low levels of the other alkali metals. The negative ToF-SIMS spectrum showed large hydride and fluoride ion peaks as well as  $\text{Na}$ ,  $\text{NaH}$ ,  $\text{NaH}_2$ ,  $\text{NaH}_3\text{F}$ ,  $\text{S}$ ,  $\text{Cl}$ , and  $\text{I}$ . Thus, there is no other possible assignment of the upfield-shifted peak based on the elements present. Furthermore, these solution-phase results not only provide an unequivocal identification of  $\text{H}_2(1/4)$  and  $\text{H}^-(1/4)$ , but their characteristics of having the absence of any solid matrix effect or the possibility of alternative assignments such as U-centered H or F centers in solid matrix confirm the solid NMR assignments as well.

The MAS  $^1\text{H}$  NMR of  $\text{KH} * \text{Cl}$  showed a very sharp -4.46 ppm upfield-shifted peak corresponding to an environment that is essentially that of a free ion; thus, it was used as a standard to determine the correction for the matrix shift of the  $\text{H}^-(1/4)$  peak. This was confirmed by solution NMR on  $\text{KH} * \text{Cl}$  having a very sharp -4.46 ppm peak and a substantial peak at 1.13 ppm in the MAS  $^1\text{H}$  NMR. Isolated  $\text{H}_2(1/4)$  and  $\text{H}^-(1/4)$  were observed in the  $^1\text{H}$  NMR of  $\text{KH} * \text{Cl}$  dissolved in DMF-d7 at 1.2 ppm and -3.86 ppm, respectively, as shown in Figure 44. The replication of the shifts with free species in the absence of any factors related to the solid matrix confirmed the solid NMR assignments of the 1.13 ppm and -4.46 ppm peaks (Figure 35A) to  $\text{H}_2(1/4)$  and  $\text{H}^-(1/4)$ . The positions of 1.2 ppm  $\text{H}_2(1/4)$  peak and the -3.86 ppm  $\text{H}^-(1/4)$  peak are identical for both compounds indicating no ion-dependent chemical shift of the corresponding free species. However, the peak width from the negative charged  $\text{H}^-(1/4)$  is dependent on the type of ions in solution. Both compounds were dissolved in the same solvent, DMF-d7, but the peak in the presence of the larger, less iterating  $\text{K}^+$  and  $\text{Cl}^-$  ions is

sharp; whereas, the peak in the presence of smaller, more strongly interacting  $Na^+$  and  $F^-$  ions is very broad indicating that the different ions in the solution differentially influence the NMR relaxation time and corresponding peak width.

The  $KH * I$  behaved differently from  $KH * Cl$  in solution NMR as well as in solid NMR. The  $^1H$  solution NMR of  $KH * I$  dissolved to saturation in DMF-d7 showed increasing intensities and slight downfield shifts of the  $H_2(1/4)$  and  $H^-(1/4)$  peaks to 1.28 ppm and -3.79 ppm, respectively, as the concentration of  $KH * I$  increased (Figure 45). The concentration-dependent solution matrix effect confirmed the solid matrix effect corresponding to the NMR assignment of  $H_2(1/4)$  and  $H^-(1/4)$  to the peaks at 1.13 ppm and -2.31 ppm shown in Figure 35B.

$^1H$  solution NMR was performed on product gases of  $NaOH$ -doped R-Ni 2400 collected and dissolved in DMF-d7 initially under liquid helium. A large  $H_2(1/4)$  peak was observed at 1.2 ppm as shown in Figure 46 confirming that  $H_2(1/4)$  was formed as a major product during the liberation of 0.75kJ/g R-Ni from the hydrino reaction. Consistent with the thermal desorption gas analysis, large methane and hydrogen peaks were also observed at 0.18 ppm and 4.55 ppm, respectively.

**F. XPS Identification of  $H^-(1/4)$  and  $H^-(1/3)$ .** A survey spectrum was obtained on each of  $LiBr$  and  $LiH * Br$  over the region  $E_b = 0 eV$  to  $1200 eV$  (Figures 47A-B). The primary element peaks allowed for the determination of all of the elements present in the  $LiH * Br$  crystals and the control  $LiBr$ . No elements were present in the survey scan which could be assigned to peaks in the low binding energy region (Figure 48) with the exception of the  $Li 1s$  peak at 55 eV (shifted 1 eV lower compared to  $LiBr$ ), the  $O 2s$  at 23 eV, the  $Br 3d_{5/2}$  and  $Br 3d_{3/2}$  peaks at 69 eV and 70 eV, respectively, the  $Br 4s$  at 15 eV, and the  $Br 4d$  at 5 eV. Accordingly, any other peaks in this region must be due to novel species. As shown in Figure 48, the XPS spectrum of  $LiH * Br$  differs from that of  $LiBr$  by having additional peaks at 9.5 eV and 12.3 eV that do not correspond to any other primary element peaks but do match the  $H^-(1/4)$   $E_b = 11.2 eV$  hydride ion (Eqs. (4) and (16)). The literature was searched for elements having a peak in the valence-band region that could be assigned to these peaks. Given the primary element peaks present, there was no known alternative assignment. Thus, the 9.5 eV and 12.3 eV peaks that could not be assigned to known elements and do not correspond to any other primary element peak were assigned to the  $H^-(1/4)$  in two different chemical environments. These features closely matched those for  $H^-(1/4)$  of  $KH * I$  reported previously [13-15, 26, 30]. The presence of  $H^-(1/4)$  in two different chemical environments is further evidenced by the  $^1H$  MAS NMR spectrum such as that  $KH * Cl$  shown in Figure 49 compared to Figure 35A.

A survey spectrum was obtained on each of  $NaBr$  and  $NaH * Br$  over the region  $E_b = 0 eV$  to  $1200 eV$  (Figures 50A-B). The primary element peaks allowed for the determination of all of the elements present in the  $NaH * Br$  crystals and the control  $NaBr$ . No

elements were present in the survey scan which could be assigned to peaks in the low binding energy region (Figure 51) with the exception of the *Na 2p* and *Na 2s* peaks at 30 eV and 63 eV (shifted 1 eV lower compared to *NaBr*), the *O 2s* at 23 eV, the *Br 3d<sub>5/2</sub>* and *Br 3d<sub>3/2</sub>* peaks at 69 eV and 70 eV, respectively, the *Br 4s* at 15.2 eV, and the *Br 4d* at 5 eV. Accordingly, any other peaks in this region must be due to novel species. As shown in Figure 51, the XPS spectrum of *NaH\*Br* differs from that of *NaBr* by having additional peaks at 9.5 eV and 12.3 eV that do not correspond to any other primary element peaks but do match the  $H^-(1/4) E_b = 11.2 \text{ eV}$  hydride ion (Eqs. (4) and (16)). The literature was searched for elements having a peak in the valence-band region that could be assigned to these peaks. Given the primary element peaks present, there was no known alternative assignment. Thus, the 9.5 eV and 12.3 eV peaks that could not be assigned to known elements and do not correspond to any other primary element peak were assigned to the  $H^-(1/4)$  in two different chemical environments.

Survey spectra over the region  $E_b = 0 \text{ eV}$  to  $1200 \text{ eV}$  were obtained on each of *Pt/Ti* and *NaH\**-coated *Pt/Ti* following the production of 15 kJ of excess heat (Figures 52A-B). The primary element peaks allowed for the determination of all of the elements present in the *NaH\**-coated *Pt/Ti* and the control *Pt/Ti*. No elements were present in the survey scan which could be assigned to peaks in the low binding energy region (Figures 53A-B) with the exception of the *Pt 4f<sub>7/2</sub>* and *Pt 4f<sub>5/2</sub>* peaks at 70.7 eV and 74 eV, respectively, and the *O 2s* at 23 eV. The *Na 2p* and *Na 2s* peaks were observed at 31 eV and 64 eV on *NaH\**-coated *Pt/Ti*, and a valence band was only observed for *Pt/Ti*. Accordingly, any other peaks in this region must be due to novel species. As shown in Figures 54A-B, the XPS spectrum of *NaH\**-coated *Pt/Ti* differs from that of *Pt/Ti* by having additional peaks at 6 eV, 10.8 eV, and 12.8 eV that do not correspond to any other primary element peaks but do match the  $H^-(1/3) E_b = 6.6 \text{ eV}$  and  $H^-(1/4) E_b = 11.2 \text{ eV}$  hydride ions (Eqs. (4) and (16)). The literature was searched for elements having a peak in the valence-band region that could be assigned to these peaks. Given the primary element peaks present, there was no known alternative assignment. Thus, the 10.8 eV, and 12.8 eV peaks that could not be assigned to known elements and do not correspond to any other primary element peak were assigned to the  $H^-(1/4)$  in two different chemical environments. The 6 eV peak matched and was assigned to  $H^-(1/3)$ . Thus, in the absence of a halide peak in this region, both fractional hydrogen states, 1/3 and 1/4, were observed as predicted by Eq. (27). The absence of a valence band due to the high-binding energies was also consistent with the hydrino hydride assignments of *NaH\**-coated *Pt/Ti*.

The results of the *NaH\**-coated *Pt/Ti* shown in Figure 54B were replicated with *NaH\**-coated *Si*. As shown in Figures 55 and 56, the XPS spectra of *NaH\**-coated *Si* showed peaks at 6 eV, 10.8 eV, and 12.8 eV that could not be assigned to known elements and do not correspond to any other primary element peak, but matched  $H^-(1/3)$  and  $H^-(1/4)$ . Thus, both fractional hydrogen states, 1/3 as  $H^-(1/3)$  at the 6 eV and 1/4 as  $H^-(1/4)$  at 10.8 eV and 12.8 eV, were present as predicted by Eq. (27).

**G. FTIR Identification of  $H_2(1/4)$ .** Samples of  $LiH * Br$  having an upfield-shifted  $^1H$  NMR peak at  $-2.5$  ppm assigned to  $H^-(1/4)$  and an NMR peak at  $1.3$  ppm assigned to the corresponding molecule  $H_2(1/4)$  were analyzed by high resolution FTIR spectroscopy. As shown in Figure 57B, a single narrow peak was observed at  $1989\text{ cm}^{-1}$ . The compounds,  $LiNH_2$ ,  $Li_2NH$ , and  $Li_3N$  are possible, based on the starting materials and predicted reactions, but none of these compounds showed peaks in the region of  $1989\text{ cm}^{-1}$ . No additional peaks other than those easily assignable to  $LiBr$  were observed (Figure 57A). An exhaustive list of species that have features in this region were considered, including exotic species such as azide, metal carbonyls, and metaborate ion. The former were eliminated based on their known spectra, which have very broad bands. Metaborate ion was eliminated by ToF-SIMS analysis, which showed a total boron content that was not detectable at the ppb level which is orders of magnitude below its FTIR detection limit and the absence of two peaks corresponding to the boron isotopes  $^{10}B$  (20% N.A.) and  $^{11}B$  (80% N.A.).

Considering a possible matrix effect, the peak at  $1989\text{ cm}^{-1}$  ( $0.24\text{ eV}$ ) matched the theoretical prediction of  $1947\text{ cm}^{-1}$  for  $H_2(1/4)$ . From Eqs. (14-15), the unprecedented rotational energy of  $4^2$  times that of ordinary hydrogen establishes the internuclear distance of  $H_2(1/4)$  as  $1/4$  that of  $H_2$ . Interstitial  $H_2$  in silicon and  $GaAs$  is a nearly free rotator showing single rovibrational transitions [85-89].  $H_2$  is FTIR active as well as Raman active due to the induced dipole from interactions with the crystalline lattice [85]. The crystalline lattice may also influence the selection rules to permit an otherwise forbidden transition in  $H_2(1/4)$ . Considering a matrix effect, the match to the predicted  $1943\text{ cm}^{-1}$  peak and the relatively narrow peak width, indicates that  $H_2(1/4)$  can rotate essentially freely inside of the crystal and confirms its small size corresponding to  $1/4$  the dimensions of ordinary hydrogen. Ordinary hydrogen shows a 3:1 ortho-para ratio at non-cryogenic temperatures; whereas, a single peak of  $H_2(1/4)$  formed under the synthesis conditions is assigned to the para form only due to the 64 times increase in stability due to the  $1/4$  relative internuclear separation. Given the frequency match of the  $1989\text{ cm}^{-1}$  peak and the absence of any known alternative, wherein hydrogen is the only known species that exhibits single rovibrational transitions in a solid matrix, the  $1989\text{ cm}^{-1}$  peak is assigned to the  $J = 0$  to  $J = 1$  rotational transitions of para  $H_2(1/4)$ .

**H.  $H_2(1/4)$  Rotational UV Spectrum by Electron Beam Excitation.**  $H_2(1/4)$  trapped in the lattice of alkali halides,  $MgX_2$  ( $X = F, Cl, Br, I$ ), and  $CuX_2$  ( $X = F, Cl, Br$ ) was investigated by windowless UV spectroscopy on electron beam excitation of the crystals using the  $12.5\text{ keV}$  electron gun at a beam current of  $10\text{-}20\ \mu\text{A}$  in the pressure range of  $<10^{-5}$  Torr. Of the alkali metals, it was found that only alkali chlorides showed the peaks predicted by Eq. (14), and the intensity roughly matched the order predicted, increasing intensity down the column of the Group I elements. In all cases, the peaks could be eliminated by heating with the loss of the Lyman  $\alpha$  peak, and no other peaks were observed in the UV. The on-line mass spectrometer recorded hydrogen only.  $^1H$  MAS NMR on these crystals showed the  $H_2(1/4)$  peak at  $1.1$  ppm with relative intensities  $Na < K < Cs$  as shown in Figure 58 that matched the intensity of the band by electron beam-excitation emission shown in Figure 59.

Of the compounds of the series  $MgX_2$  ( $X = F, Cl, Br, I$ ) and  $CuX_2$  ( $X = F, Cl, Br$ ), the predicted band was just detectable only for  $MgI_2$  which, in this case, can be attributed to  $Mg^{2+}$  as the catalyst. NMR on these crystals showed the  $H_2(1/4)$  peak at 1.13 ppm only in  $MgX_2$  with relative intensities  $F, Cl, Br, \ll I$  that matched the detection of the band by electron beam-excitation emission for  $MgI_2$  only.

The 100-350 nm spectrum of electron beam-excited  $CsCl$  crystals having trapped  $H_2(1/4)$  is shown in Figure 60. A series of evenly spaced lines was observed in the 220-300 nm region as shown in Figure 60. The series matched the spacing and intensity profile of the P branch of  $H_2(1/4)$  given by Eq. (14). P(1), P(2), P(3), P(4), P(5), and P(6) were observed at 226.0 nm, 237.0 nm, 249.5 nm, 262.5 nm, 277.0 nm, and 292.5 nm, respectively. The slope of the linear curve-fit of the energies of the peaks shown in Figure 60 is 0.25 eV with an intercept of 5.73 eV and a sum of residual errors  $r^2 < 10^{-4}$ . The slope matches the predicted rotational energy spacing of 0.241 eV (Eq. (14);  $p = 4$ ) with  $J' - J'' = -1$ ;  $J'' = 1, 2, 3, 4, 5, 6$  where  $J''$  is the rotational quantum number of the final state.  $H_2(1/4)$  is a free rotator, but is not a free vibrator which is similar to the case of interstitial hydrogen in silicon discussed previously [85-89]. The observed intercept of 5.73 eV is shifted from the predicted  $\nu = 1 \rightarrow \nu = 0$  vibrational energy of  $H_2(1/4)$  of 8.25 eV (Eq. (13)) by about twice the percentage as that of interstitial  $H_2$  in silicon [85-89]. In the latter case, vibrational energy of free  $H_2$  is  $4161 \text{ cm}^{-1}$ , whereas the vibrational peaks in silicon are observed at 3618 and  $3627 \text{ cm}^{-1}$  corresponding to ortho and para- $H_2$ , respectively [85]. In the former case the shift is about 30% lower, possibly due to an increase in the effective mass from coupling of the molecular vibrational mode with the crystal lattice.

Using Eqs. (14) and (15) with the measured rotational energy spacing of 0.25 eV establishes an internuclear distance of 1/4 that of the ordinary  $H_2$  for  $H_2(1/4)$ . A corresponding weak band was observed from  $NaH^*Br$ , and a more intense band was observed from  $NaH^*Cl$ . Regarding the latter case, the intensity of the emission was significantly increased by trapping  $H_2(1/4)$  in a silicon matrix. The 100-550 nm spectrum of an electron beam-excited silicon wafer coated with  $NaH^*Cl$  having trapped  $H_2(1/4)$  is shown in Figure 61. The series matching the spacing and intensity profile of the P branch of  $H_2(1/4)$  given by Eq. (14) was observed. P(1), P(2), P(3), P(4), P(5), and P(6) were observed at 222.5 nm, 233.4 nm, 245.2 nm, 258.2 nm, 272.2 nm, and 287.4 nm, respectively. The slope of the linear curve-fit of the energies of the peaks shown in Figure 61 is 0.25 eV with an intercept of 5.82 eV and a sum of residual errors  $r^2 < 10^{-4}$ . The linearity is characteristic of rotation, and the results again match  $H_2(1/4)$ . This technique confirms the solid NMR and FTIR results given in Secs. III E and III G, respectively.

The results of the spectroscopic investigation of the vibration-rotational emission of  $H_2(1/4)$  using a 12.5 keV electron gun to initiate argon plasmas with 1% hydrogen as a source of  $Ar^+$  catalysts and  $H$  atoms were reported previously [50-51]. The typically observed series shown in Figure 62 matches the predicted  $\nu = 1 \rightarrow \nu = 0$  vibrational energy of  $H_2(1/4)$  of 8.25 eV (Eq. (13)) and its predicted rotational energy spacing of 0.24 eV (Eq. (14)). Specifically, the

series identically matched the P branch of  $H_2(1/4)$  for the vibrational transition  $\nu=1 \rightarrow \nu=0$ . P(1), P(2), P(3), P(4), and P(5) were observed (Figure 62) at 154.8 nm, 160.0 nm, 165.6 nm, 171.6 nm, and 177.8 nm, respectively. Similarly to the case of the MAS  $^1H$  NMR of  $H_2(1/4)$  reported in Sec. III E, the evenly spaced series of lines shown in Figure 62 were previously reported by another research group as shown in Figure 6 of Ref. [90] and could not be unambiguously assigned by the authors. The series was observed with the same type of e-beam argon plasma with a “contaminant gas” and not observed in krypton and xenon plasmas. The results match the P branch of  $H_2(1/4)$  formed with hydrogen contamination of the argon plasma. It was also reported previously [13-14] that when  $KH^*Cl$  having  $H^-(1/4)$  by NMR was incident to the 12.5 keV electron beam, similar excited emission of interstitial  $H_2(1/4)$  was observed as that from electron-beam excited alkali chlorides,  $NaH^*Cl$ -coated  $Si$ , and the argon-hydrogen plasmas [13-14]. It was further observed that the band assigned to  $H_2(1/4)$  was eliminated from the  $KCl$  starting material by heating to high temperature.  $KH^*Cl$  was then synthesized from the heat-treated  $KCl$ , and  $H_2(1/4)$  trapped in the lattice of  $KH^*Cl$  was then observed in addition to  $H^-(1/4)$  demonstrating that multiple catalysts,  $HCl$ ,  $NaH$ ,  $K$ , and  $Ar^+$ , can give rise to  $H_2(1/4)$ .

#### IV. Conclusion

In this study we made specific theoretical predictions and tested them with standard, easily interpretable experiments. The results of spectroscopic, chemical, and thermal data show that new energy states of hydrogen are formed by the reaction of  $H$  with catalysts such as  $Li$  and  $NaH$ . Using reagents to generate the catalysts such as  $Li$  and  $NaH$  to form significantly more stable hydrides and hydrogen molecules, the power and energy balance data demonstrate that this novel reaction of atomic hydrogen can proceed with fast kinetics and produce high reaction yields. It is a new energy source ready for commercialization. The energy scaled linearly and the power increased nonlinearly to easily achieve over 50 kW. Based on the volume of the catalyst and hydrogen fuel, the power density is among the highest known, (comparable to or higher than that of internal combustion), and the energy balance is greater than that of any known material on a weight or molar basis. Consequently, the mass balance and cost per unit energy is much lower than that of burning fossil fuels. Furthermore, the process is nonpolluting. Since the identified  $H_2(1/p)$  byproduct is stable and lighter-than-air, it cannot accumulate in the Earth's atmosphere. And, it is present in the environment such as in common ingested salts. Thus, the typical \$500,000,000/plant-yr fossil fuel cost and the environmental impact to the air, water, and ground of producing, handling, and using fossil fuels may be eliminated. Similarly, the radioactive waste from nuclear plants, their tremendous infrastructure costs, and security and accident risks may also be avoided.

Preferably, as reported previously [13], rather than pollutants the byproducts have significant advanced technology applications based on their stability characteristics. For example, hydride ions  $H^-(1/p)$  having extraordinary binding energies may stabilize a cation  $M^{x+}$  in an extraordinarily high oxidation state as the basis of a high voltage battery, and significant applications exist for the corresponding molecular species  $H_2(1/p)$  wherein the

excited vibration-rotational levels could be the basis of a UV laser that could significantly advance photolithography and line-of-sight telecommunications.

With simple systems, commercial levels of power can be generated at typical power-plant operating temperatures and at higher power densities, and the power was found to be easily scalable in terms of the quantity of reactants used. We envision plants that continuously regenerate the solid fuel mixture using known industrial processes involving evaporation of small amounts of excess  $Na$  reductant and reaction of the chemical intermediate  $Na_2O$  with a water-vapor stream to form  $NaOH$  as the source of the  $NaH$  catalyst. Only the hydrogen fuel obtained ultimately from the water is consumed with enormous energy release relative to combustion.

## References

1. R. Mills, *The Grand Unified Theory of Classical Physics*; June 2008 Edition, posted at <http://www.blacklightpower.com/theory/bookdownload.shtml>.
2. R. Mills, Y. Lu, "Fifth Force," submitted.
3. R. L. Mills, "Classical Quantum Mechanics," *Physics Essays*, Vol. 16, No. 4, December, (2003), pp. 433-498.
4. R. Mills, "Physical Solutions of the Nature of the Atom, Photon, and Their Interactions to Form Excited and Predicted Hydrino States," in press.
5. R. L. Mills, "Exact Classical Quantum Mechanical Solutions for One- Through Twenty-Electron Atoms," *Physics Essays*, Vol. 18, (2005), pp. 321-361.
6. R. L. Mills, "The Nature of the Chemical Bond Revisited and an Alternative Maxwellian Approach," *Physics Essays*, Vol. 17, (2004), pp. 342-389.
7. R. L. Mills, "Maxwell's Equations and QED: Which is Fact and Which is Fiction," *Physics Essays*, Vol. 19, (2006), pp. 225-262.
8. R. L. Mills, "Exact Classical Quantum Mechanical Solution for Atomic Helium Which Predicts Conjugate Parameters from a Unique Solution for the First Time," in press.
9. R. L. Mills, "The Fallacy of Feynman's Argument on the Stability of the Hydrogen Atom According to Quantum Mechanics," *Annales de la Fondation Louis de Broglie*, Vol. 30, No. 2, (2005), pp. 129-151.
10. R. Mills, "The Grand Unified Theory of Classical Quantum Mechanics," *Int. J. Hydrogen Energy*, Vol. 27(5), (2002), pp. 565-590.
11. R. Mills, The Nature of Free Electrons in Superfluid Helium—a Test of Quantum Mechanics and a Basis to Review its Foundations and Make a Comparison to Classical Theory, *Int. J. Hydrogen Energy*, Vol. 26(10), (2001), pp. 1059-1096.
12. R. Mills, "The Hydrogen Atom Revisited," *Int. J. of Hydrogen Energy*, Vol. 25(12), December, (2000), pp. 1171-1183.
13. R. L. Mills, J. He, Y. Lu, M. Nansteel, Z. Chang, B. Dhandapani, "Comprehensive Identification and Potential Applications of New States of Hydrogen," *Int. J. Hydrogen Energy*, Vol. 32(14), (2007), pp. 2988-3009.
14. R. Mills, J. He, Z. Chang, W. Good, Y. Lu, B. Dhandapani, "Catalysis of Atomic Hydrogen to Novel Hydrogen Species  $H^-(1/4)$  and  $H_2(1/4)$  as a New Power Source," *Int. J. Hydrogen Energy*, Vol. 32(12), (2007), pp. 2573-2584.
15. R. Mills, P. Ray, B. Dhandapani, W. Good, P. Jansson, M. Nansteel, J. He, A. Voigt, "Spectroscopic and NMR Identification of Novel Hydride Ions in Fractional Quantum

- Energy States Formed by an Exothermic Reaction of Atomic Hydrogen with Certain Catalysts,” *European Physical Journal-Applied Physics*, Vol. 28, (2004), pp. 83-104.
16. R. Mills and M. Nansteel, P. Ray, “Argon-Hydrogen-Strontium Discharge Light Source,” *IEEE Transactions on Plasma Science*, Vol. 30, No. 2, (2002), pp. 639-653.
  17. R. Mills and M. Nansteel, P. Ray, “Bright Hydrogen-Light Source due to a Resonant Energy Transfer with Strontium and Argon Ions,” *New Journal of Physics*, Vol. 4, (2002), pp. 70.1-70.28.
  18. R. Mills, J. Dong, Y. Lu, “Observation of Extreme Ultraviolet Hydrogen Emission from Incandescently Heated Hydrogen Gas with Certain Catalysts,” *Int. J. Hydrogen Energy*, Vol. 25, (2000), pp. 919-943.
  19. R. Mills, M. Nansteel, and P. Ray, “Excessively Bright Hydrogen-Strontium Plasma Light Source Due to Energy Resonance of Strontium with Hydrogen,” *J. of Plasma Physics*, Vol. 69, (2003), pp. 131-158.
  20. R. L. Mills, J. He, M. Nansteel, B. Dhandapani, “Catalysis of Atomic Hydrogen to New Hydrides as a New Power Source,” *International Journal of Global Energy Issues (IJGEI)*, Special Edition in Energy Systems, Vol. 28, Nos. 2/3 (2007), pp. 304-324.
  21. H. Conrads, R. Mills, Th. Wrubel, “Emission in the Deep Vacuum Ultraviolet from a Plasma Formed by Incandescently Heating Hydrogen Gas with Trace Amounts of Potassium Carbonate,” *Plasma Sources Science and Technology*, Vol. 12, (2003), pp. 389-395.
  22. J. Phillips, R. L. Mills, X. Chen, “Water Bath Calorimetric Study of Excess Heat in ‘Resonance Transfer’ Plasmas,” *Journal of Applied Physics*, Vol. 96, No. 6, pp. 3095-3102.
  23. R. L. Mills, X. Chen, P. Ray, J. He, B. Dhandapani, “Plasma Power Source Based on a Catalytic Reaction of Atomic Hydrogen Measured by Water Bath Calorimetry,” *Thermochimica Acta*, Vol. 406/1-2, (2003), pp. 35-53.
  24. R. Mills, B. Dhandapani, M. Nansteel, J. He, T. Shannon, A. Echezuria, “Synthesis and Characterization of Novel Hydride Compounds,” *Int. J. of Hydrogen Energy*, Vol. 26(4), (2001), pp. 339-367.
  25. R. Mills, B. Dhandapani, M. Nansteel, J. He, A. Voigt, “Identification of Compounds Containing Novel Hydride Ions by Nuclear Magnetic Resonance Spectroscopy,” *Int. J. Hydrogen Energy*, Vol. 26(9), (2001), pp. 965-979.
  26. R. Mills, B. Dhandapani, N. Greenig, J. He, “Synthesis and Characterization of Potassium Iodo Hydride,” *Int. J. of Hydrogen Energy*, Vol. 25(12), (2000), pp. 1185-1203.
  27. R. L. Mills, P. Ray, “Extreme Ultraviolet Spectroscopy of Helium-Hydrogen Plasma,” *J. Phys. D, Applied Physics*, Vol. 36, (2003), pp. 1535-1542.
  28. R. L. Mills, P. Ray, B. Dhandapani, M. Nansteel, X. Chen, J. He, “New Power Source from Fractional Quantum Energy Levels of Atomic Hydrogen that Surpasses Internal Combustion,” *J Mol. Struct.*, Vol. 643, No. 1-3, (2002), pp. 43-54.
  29. R. Mills, P. Ray, “Spectral Emission of Fractional Quantum Energy Levels of Atomic Hydrogen from a Helium-Hydrogen Plasma and the Implications for Dark Matter,” *Int. J. Hydrogen Energy*, Vol. 27(3), (2002), pp. 301-322.
  30. R. L. Mills, P. Ray, “A Comprehensive Study of Spectra of the Bound-Free Hyperfine Levels of Novel Hydride Ion  $H^-(1/2)$ , Hydrogen, Nitrogen, and Air,” *Int. J. Hydrogen Energy*, Vol. 28(8), (2003), pp. 825-871.
  31. R. Mills, “Spectroscopic Identification of a Novel Catalytic Reaction of Atomic Hydrogen and the Hydride Ion Product,” *Int. J. Hydrogen Energy*, Vol. 26(10), (2001), pp. 1041-1058.

32. R. L. Mills, P. Ray, B. Dhandapani, R. M. Mayo, J. He, "Comparison of Excessive Balmer  $\alpha$  Line Broadening of Glow Discharge and Microwave Hydrogen Plasmas with Certain Catalysts," J. Applied Physics, Vol. 92, No. 12, (2002), pp. 7008-7022.
33. R. L. Mills, P. Ray, B. Dhandapani, J. He, "Comparison of Excessive Balmer  $\alpha$  Line Broadening of Inductively and Capacitively Coupled RF, Microwave, and Glow Discharge Hydrogen Plasmas with Certain Catalysts," IEEE Transactions on Plasma Science, Vol. 31, (2003), pp. 338-355.
34. R. L. Mills, P. Ray, "Substantial Changes in the Characteristics of a Microwave Plasma Due to Combining Argon and Hydrogen," New Journal of Physics, www.njp.org, Vol. 4, (2002), pp. 22.1-22.17.
35. R. L. Mills, B. Dhandapani, K. Akhtar, "Excessive Balmer  $\alpha$  Line Broadening of Water-Vapor Capacitively-Coupled RF Discharge Plasmas," Int. J. Hydrogen Energy, Vol. 33, (2008), pp. 802-815.
36. R. Mills, P. Ray, B. Dhandapani, "Evidence of an Energy Transfer Reaction Between Atomic Hydrogen and Argon II or Helium II as the Source of Excessively Hot H Atoms in RF Plasmas," Journal of Plasma Physics, (2006), Vol. 72, Issue 4, pp. 469-484.24.
37. J. Phillips, C-K Chen, K. Akhtar, B. Dhandapani, R. Mills, "Evidence of Catalytic Production of Hot Hydrogen in RF Generated Hydrogen/Argon Plasmas," Int. J. Hydrogen Energy, Vol. 32(14), (2007), 3010-3025.
38. R. Mills, P. Ray, R. M. Mayo, "CW HI Laser Based on a Stationary Inverted Lyman Population Formed from Incandescently Heated Hydrogen Gas with Certain Group I Catalysts," IEEE Transactions on Plasma Science, Vol. 31, No. 2, (2003), pp. 236-247.
39. R. L. Mills, P. Ray, "Stationary Inverted Lyman Population Formed from Incandescently Heated Hydrogen Gas with Certain Catalysts," J. Phys. D, Applied Physics, Vol. 36, (2003), pp. 1504-1509.
40. R. Mills, P. Ray, R. M. Mayo, "The Potential for a Hydrogen Water-Plasma Laser," Applied Physics Letters, Vol. 82, No. 11, (2003), pp. 1679-1681.
41. R. L. Mills, *The Grand Unified Theory of Classical Quantum Mechanics*, November 1995 Edition, HydroCatalysis Power Corp., Malvern, PA, Library of Congress Catalog Number 94-077780, ISBN number ISBN 0-9635171-1-2, Chp. 22.
42. F. Bournaud, P. A. Duc, E. Brinks, M. Boquien, P. Amram, U. Lisenfeld, B. Koribalski, F. Walter, V. Charmandaris, "Missing mass in collisional debris from galaxies," Science, Vol. 316, (2007), pp. 1166-1169.
43. B. G. Elmegreen, "Dark matter in galactic collisional debris," Science, Vol. 316, (2007), pp. 32-33.
44. R. L. Mills, Y. Lu, K. Akhtar, "Spectroscopic Observation of Helium-Ion- and Hydrogen-Catalyzed Hydrino Transitions," submitted.
45. N. V. Sidgwick, *The Chemical Elements and Their Compounds*, Volume I, Oxford, Clarendon Press, (1950), p.17.
46. M. D. Lamb, *Luminescence Spectroscopy*, Academic Press, London, (1978), p. 68.
47. K. R. Lykke, K. K. Murray, W. C. Lineberger, "Threshold photodetachment of  $H^-$ ," Phys. Rev. A, Vol. 43, No. 11, (1991), pp. 6104-6107.
48. D. R. Lide, *CRC Handbook of Chemistry and Physics*, 79 th Edition, CRC Press, Boca Raton, Florida, (1998-9), p. 10-175.
49. H. Beutler, Z. Physical Chem., "Die dissoziationswärme des wasserstoffmolekuls  $H_2$ , aus einem neuen ultravioletten resonanzbandenzug bestimmt," Vol. 27B, (1934), pp. 287-302.

50. G. Herzberg, L. L. Howe, "The Lyman bands of molecular hydrogen," *Can. J. Phys.*, Vol. 37, (1959), pp. 636-659.
51. P. W. Atkins, *Physical Chemistry*, Second Edition, W. H. Freeman, San Francisco, (1982), p. 589.
52. F. Abeles (Ed.), *Optical Properties of Solids*, (1972), p. 725.
53. D. R. Lide, *CRC Handbook of Chemistry and Physics*, 86th Edition, CRC Press, Taylor & Francis, Boca Raton, (2005-6), pp. 10-202 to 10-204.
54. F. A. Cotton, G. Wilkinson, C. A. Murillo, M. Bochmann, *Advanced Inorganic Chemistry*, Sixth Edition, John Wiley & Sons, Inc., New York, (1999), pp. 92-93.
55. D. R. Lide, *CRC Handbook of Chemistry and Physics*, 86th Edition, CRC Press, Taylor & Francis, Boca Raton, (2005-6), pp. 9-54 to 9-59.
56. P. Chen, Z. Xiong, J. Luo, J. Lin, K. L. Tan, "Interaction of Hydrogen with Metal Nitrides and Amides," *Nature*, 420, (2002), 302-304.
57. P. Chen, Z. Xiong, J. Luo, J. Lin, K. L. Tan, "Interaction between Lithium Amide and Lithium Hydride," *J. Phys. Chem. B*, 107, (2003), 10967-10970.
58. W. I. F. David, M. O. Jones, D. H. Gregory, C. M. Jewell, S. R. Johnson, A. Walton, P. Edwards, "A Mechanism for Non-stoichiometry in the Lithium Amide/Lithium Imide Hydrogen Storage Reaction," *J. Am. Chem. Soc.*, 129, (2007), 1594-1601.
59. D. B. Grotjahn, P. M. Sheridan, I. Al Jihad, L. M. Ziurys, "First Synthesis and Structural Determination of a Monomeric, Unsolvated Lithium Amide,  $\text{LiNH}_2$ ," *J. Am. Chem. Soc.*, 123, (2001), 5489-5494.
60. F. E. Pinkerton, "Decomposition Kinetics of Lithium Amide for Hydrogen Storage Materials," *J. Alloys Compd.*, 400, (2005), 76-82.
61. Y. Kojima, Y. Kawai, "IR Characterizations of Lithium Imide and Amide," *J. Alloys Compd.*, 395, (2005), 236-239.
62. T. Ichikawa, S. Isobe, N. Hanada, H. Fujii, "Lithium Nitride for Reversible Hydrogen Storage," *J. Alloys Compd.*, 365, (2004), 271-276.
63. Y. H. Hu, E. Ruckenstein, "Ultrafast Reaction between  $\text{Li}_3\text{N}$  and  $\text{LiNH}_2$  to Prepare the Effective Hydrogen Storage Material  $\text{Li}_2\text{NH}$ ," *Ind. Eng. Chem. Res.*, 45, (2006), 4993-4998.
64. Y. H. Hu, E. Ruckenstein, "Hydrogen Storage of  $\text{LiNH}_2$  Prepared by Reacting Li with  $\text{NH}_3$ ," *Ind. Eng. Chem. Res.*, 45, (2006), 182-186.
65. Y. H. Hu, E. Ruckenstein, "High Reversible Hydrogen Capacity of  $\text{LiNH}_2/\text{Li}_3\text{N}$  Mixtures," *Ind. Eng. Chem. Res.*, 44, (2005), 1510-1513.
66. D. R. Lide, *CRC Handbook of Chemistry and Physics*, 86th Edition, CRC Press, Taylor & Francis, Boca Raton, (2005-6), pp. 5-4 to 5-18; 9-63.
67. P. Chen, Z. Xiong, J. Luo, J. Lin, K.L. Tan, "Interaction of hydrogen with metal nitrides and imides," *Nature*, Vol. 420, (2002), pp. 302-304.
68. Yun Hang Hu, Eli Ruckenstein, "Hydrogen Storage of  $\text{Li}_2\text{NH}$  Prepared by Reacting Li with  $\text{NH}_3$ ," *Ind. Eng. Chem. Res.*, Vol. 45, (2006), pp. 182-186.
69. K. Ohoyama, Y. Nakamori, S. Orimo, "Characteristic Hydrogen Structure in Li-N-H Complex Hydrides," *Proceedings of the International Symposium on Research Reactor and Neutron Science—In Commemoration of the 10<sup>th</sup> Anniversary of HANARO—Daejeon, Korea, April 2005*, pp. 655-657.
70. *Microsc. Microanal. Microstruct.*, Vol. 3, 1, (1992).
71. For specifications see PHI Trift II, ToF-SIMS Technical Brochure, (1999), Eden Prairie, MN 55344.

72. W. M. Muller, J. P. Blackledge, G. G. Libowitz, *Metal Hydrides*, Academic Press, New York, (1968), p 201.
73. David R. Lide, *CRC Handbook of Chemistry and Physics*, 79 th Edition, CRC Press, Boca Raton, Florida, (1998-9), p. 12-191.
74. R. R. Cavanagh, R. D. Kelley, J. J. Rush, “Neutron vibrational spectroscopy of hydrogen and deuterium on Raney nickel,” *J. Chem. Phys.*, 77(3), (1982), 1540–1547.
75. I. Nicolau, R. B. Andersen, “Hydrogen in a commercial Raney nickel,” *J. Catalysis*, Vol. 68, (1981), 339–348.
76. K. Niessen, A. R. Miedema, F. R. de Boer, R. Boom, “Enthalpies of formation of liquid and solid binary alloys based on 3d metals,” *Physica B*, Vol. 152, (1988), 303–346.
77. B. S. Hemingway, R. A. Robie, “Enthalpies of formation of low albite ( $NaAlSi_3O_8$ ), gibbsite ( $Al(OH)_3$ ), and  $NaAlO_2$ ; revised values for  $\Delta H_{f,298^{\circ}}$  and  $\Delta G_{f,298^{\circ}}$  of some aluminosilicate minerals,” *J. Res. U.S. Geol. Surv.*, Vol. 5(4), (1977), pp. 413-429.
78. B. Baranowski, S. M. Filipek, “45 years of nickel hydride—history and perspectives,” *J. Alloys Compd.*, 404-406, (2005), pp. 2-6.
79. K. K. Baldrige, J. S. Siegel, “Correlation of empirical  $\delta$ (TMS) and absolute NMR chemical shifts predicted by ab initio computations,” *J. Phys. Chem. A*, Vol. 103, (1999), pp. 4038-4042.
80. J. Mason, Editor, *Multinuclear NMR*, Plenum Press, New York, (1987), Chp. 3.
81. C. Suarez, E. J. Nicholas, M. R. Bowman, “Gas-phase dynamic NMR study of the internal rotation in N-trifluoroacetylpyrrolidine,” *J. Phys. Chem. A*, Vol. 107, (2003), pp. 3024-3029.
82. C. Suarez, “Gas-phase NMR spectroscopy,” *The Chemical Educator*, Vol. 3, No. 2, (1998).
83. C. Lu, J. Hu, J. H. Kwak, Z. Yang, R. Ren, T. Markmaitree, L. Shaw, “Study the Effects of Mechanical Activation on Li-N-H Systems with  $^1H$  and  $^6Li$  Solid-State NMR,” *J. Power Sources*, Vol. 170, (2007), 419–424.
84. E. D. Becker, *High Resolution NMR Theory and Chemical Applications*, Second Edition, Academic Press, Inc., Orlando, (1980), pp. 20-22, 184-198.
85. M. Stavola, E. E. Chen, W. B. Fowler, G. A. Shi, “Interstitial  $H_2$  in Si: are All Problems Solved?” *Physica B*, 340–342, (2003), pp. 58–66.
86. E. V. Lavrov, J. Weber, “Ortho and Para Interstitial  $H_2$  in Silicon,” *Phys. Rev. Letts.*, 89(21), (2002), pp. 215501 to 1–215501-4.
87. E. E. Chen, M. Stavola, W. B. Fowler, J. A. Zhou, “Rotation of Molecular Hydrogen in Si: Unambiguous Identification of Ortho- $H_2$  and Para- $D_2$ ,” *Phys. Rev. Letts.*, 88(24), (2002), pp. 245503-1 to 245503-4.
88. E. E. Chen, M. Stavola, W. B. Fowler, P. Walters, “Key to Understanding Interstitial  $H_2$  in Si,” *Phys. Rev. Letts.*, 88(10), (2002), pp. 105507-1 to 105507-4.
89. A. W. R. Leitch, V. Alex, J. Weber, “Raman Spectroscopy of Hydrogen Molecules in Crystalline Silicon,” *Phys. Rev. Letts.*, 81(2), (1998), pp. 421–424.
90. A. Ulrich, J. Wieser, D. E. Murnick, “Excimer Formation Using Low Energy Electron Beam Excitation,” Second International Conference on Atomic and Molecular Pulsed Lasers, Proceedings of SPIE, Vol. 3403, (1998), pp. 300-307.

Figure 1. The experimental set up comprising a filament gas cell to form lithium-argon-hydrogen and lithium-hydrogen rt-plasmas.

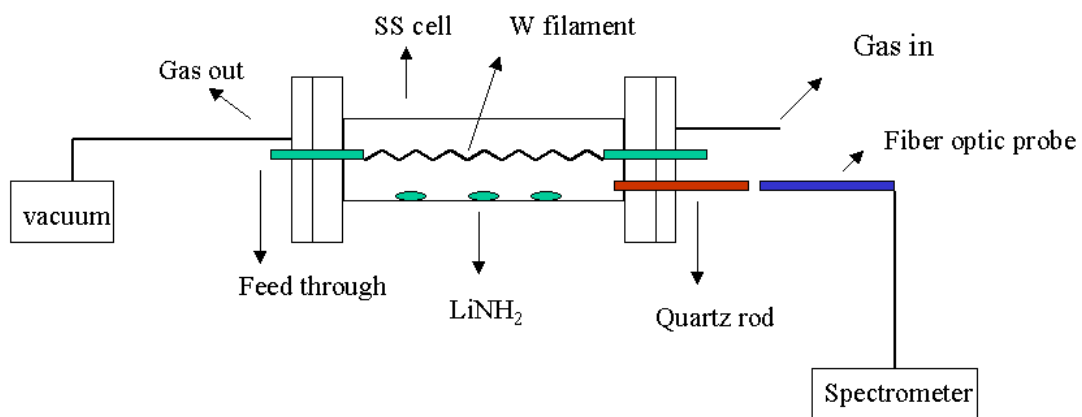


Figure 2. Schematic of the reaction cell and the cross sectional view of the water flow calorimeter used to measure the energy balances of the *Li* and *NaH* catalyst reactions to form hydrinos. The components were: 1—inlet and outlet thermistors; 2—high-temperature valve; 3—ceramic fiber heater; 4—copper water-coolant coil; 5—reactor; 6—insulation; 7—cell thermocouple, and 8—water flow chamber.

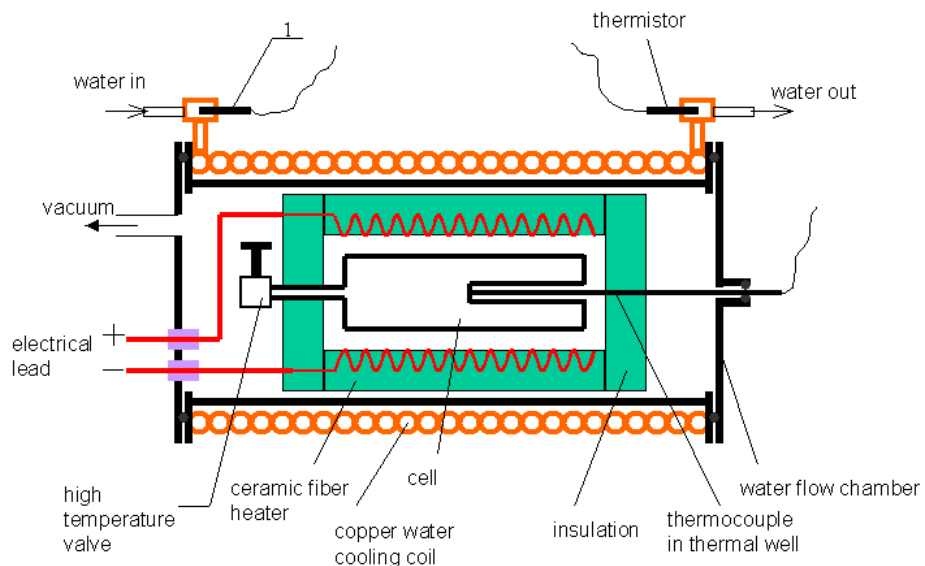


Figure 3. Schematic of the water flow calorimeter used to measure the energy balance of the  $NaH$  catalyst reaction to form hydrinos.

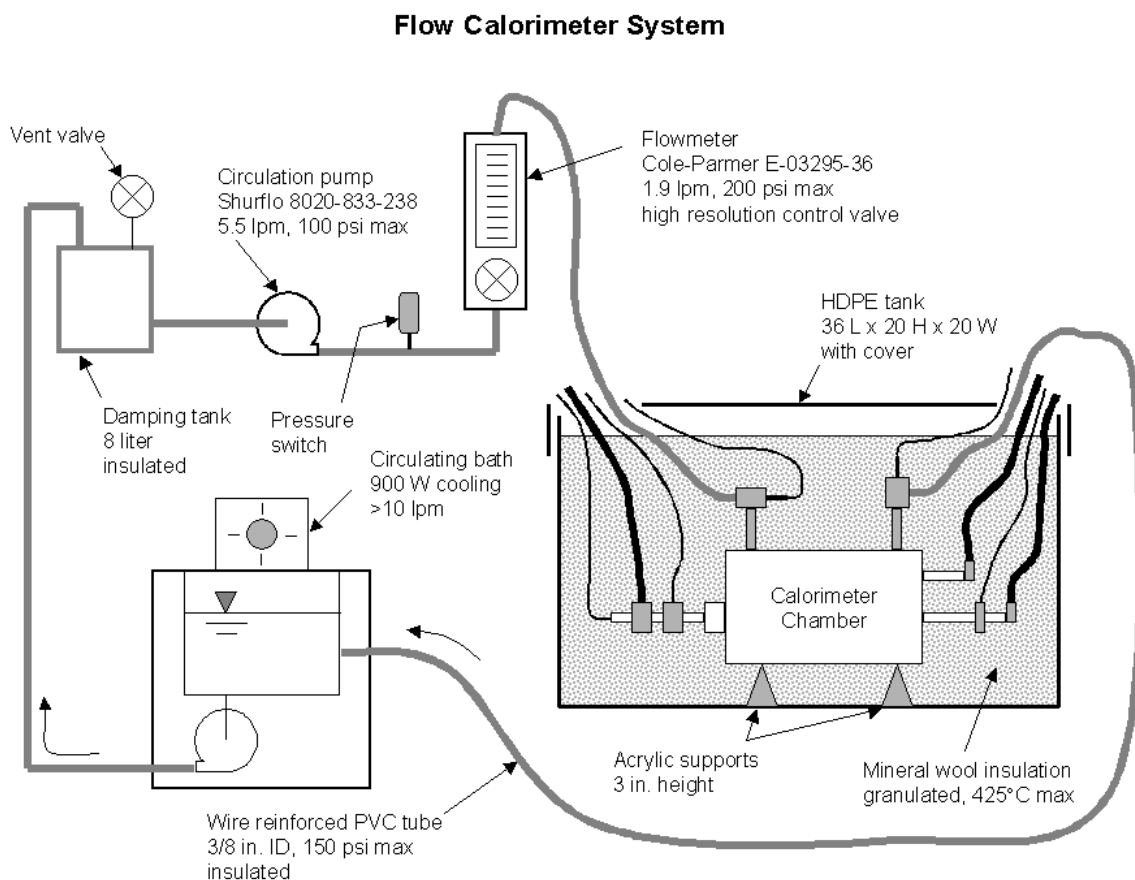


Figure 4. Stainless steel gas cell to synthesize  $LiH \cdot X$  and  $NaH \cdot X$  comprising a reaction mixture such as (i) R-Ni,  $Li$ ,  $LiNH_2$ , and  $LiX$  ( $X$  is a halide) (ii) Pt/Ti dissociator,  $Na$ ,  $NaH$ , and  $NaX$  ( $X$  is a halide) as the reactants. The components were: 101—stainless steel cell; 117—internal cavity of cell; 118—high vacuum conflat flange; 119—mating blank conflat flange; 102—stainless steel tube vacuum line and gas supply line; 103—lid to the kiln or top insulation, 104—surrounding heaters covered by high temperature insulation; 108—Pt/Ti dissociator; 109—reactants; 110—high vacuum turbo pump; 112—pressure gauge; 111—vacuum pump valve; 113—valve; 114—valve; 115—regulator, and 116—hydrogen tank.

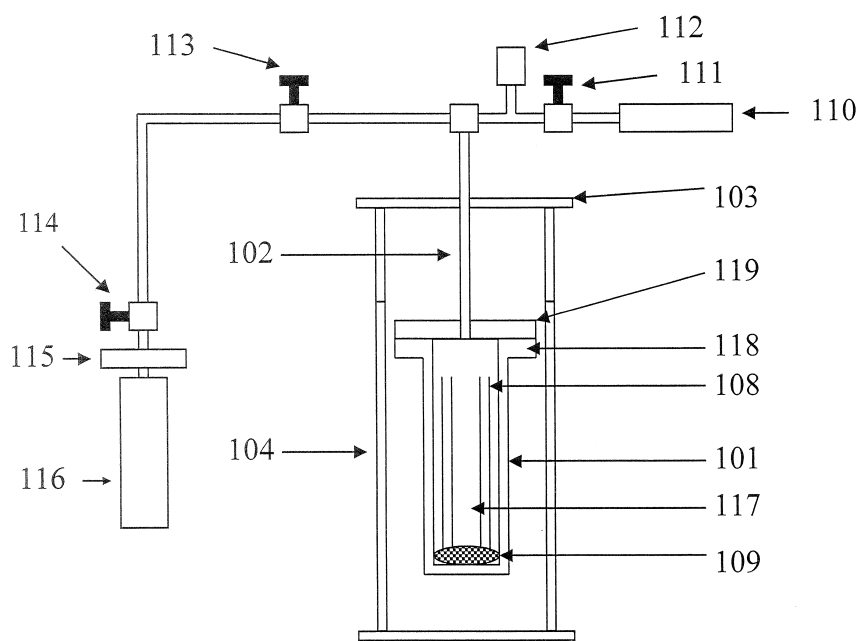


Figure 5. The 656.3 nm Balmer  $\alpha$  line width recorded with a high-resolution visible spectrometer on (A) the initial emission of a lithium-argon-hydrogen rt-plasma and (B) the emission at 70 hours of operation. Lithium lines and significant broadening of only the  $H$  lines was observed over time corresponding to an average hydrogen atom temperature of  $>40$  eV and fractional population over 90%.

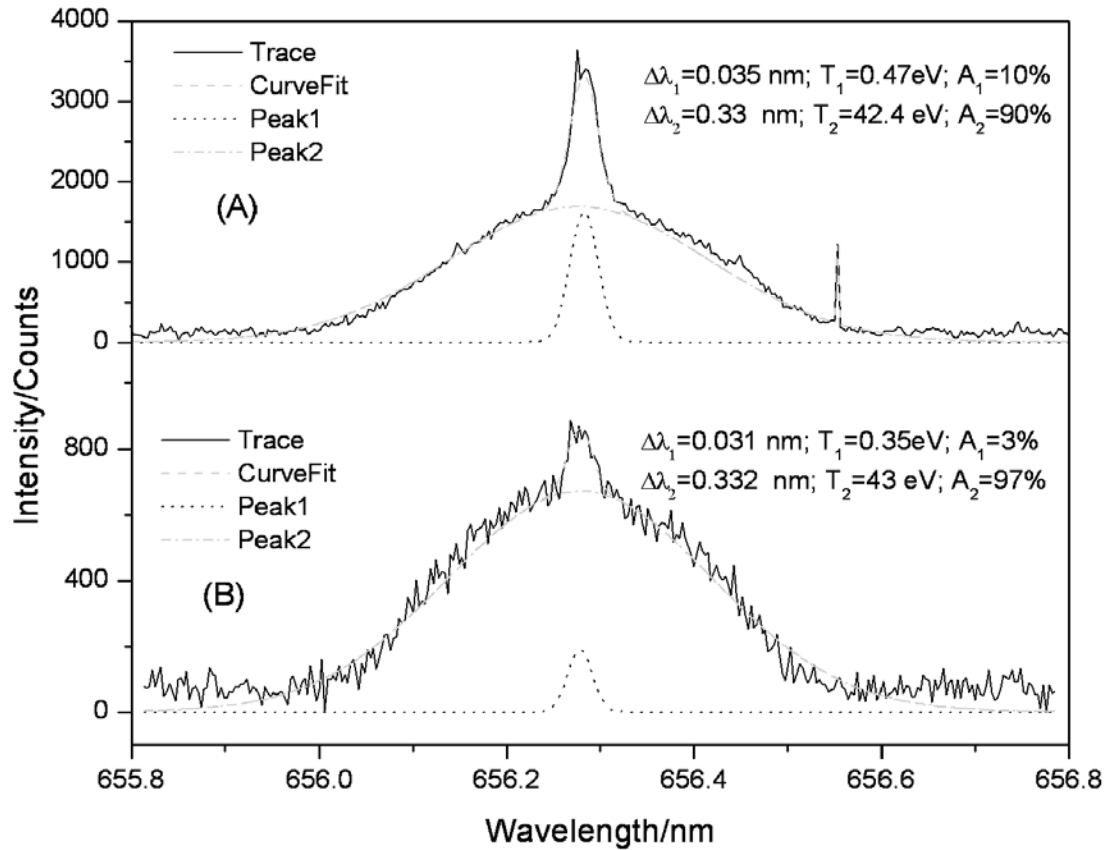


Figure 6. The 656.3 nm Balmer  $\alpha$  line width recorded with a high-resolution ( $\pm 0.006$  nm) visible spectrometer on (A) the initial emission of a lithium-hydrogen rt-plasma and (B) the emission at 70 hours of operation. Lithium lines and broadening of only the  $H$  lines was observed over time, but diminished relative to the case having the argon-hydrogen gas (95/5%). The Balmer width corresponded to an average hydrogen atom temperature of 6 eV and a 27% fractional population.

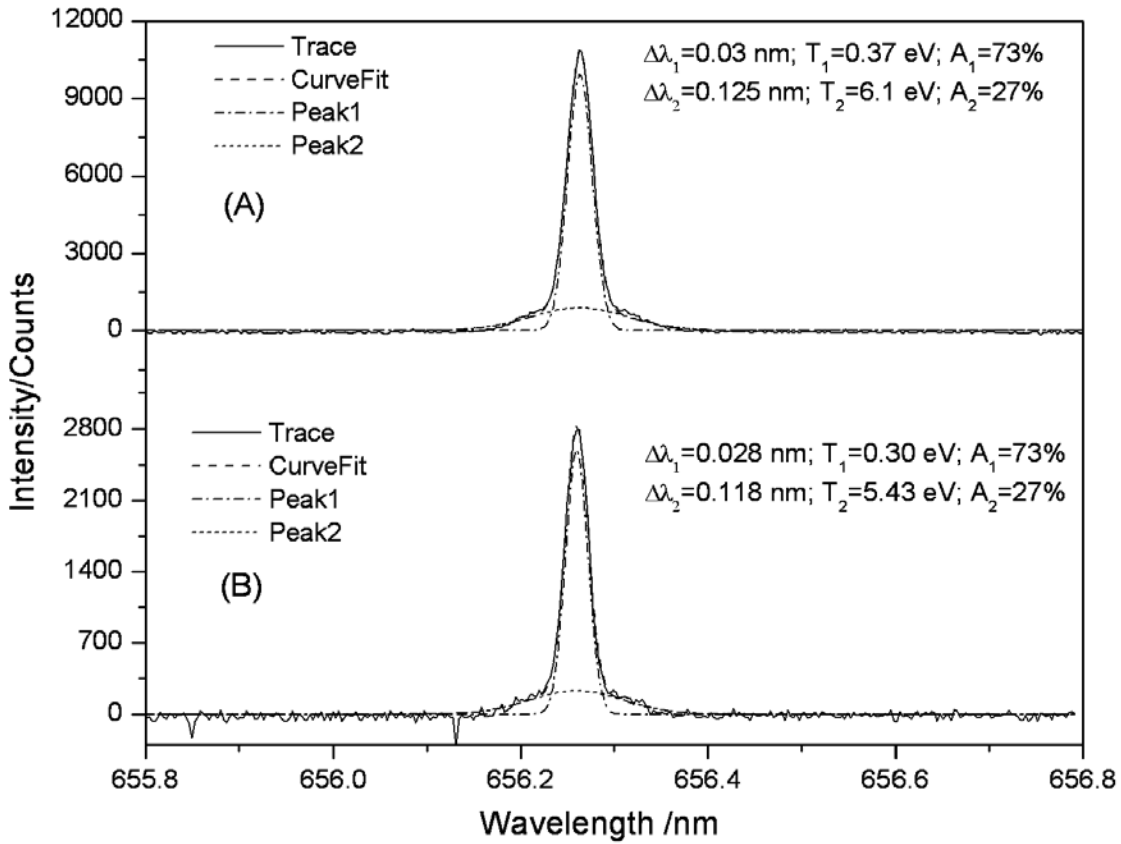


Figure 7. The results of the DSC (100-750 °C) of  $\text{NaH}$  at a scan rate of 0.1 degree/minute. A broad endothermic peak was observed at 350°C to 420 °C which corresponds to 47 kJ/mole and matches sodium hydride decomposition in this temperature range with a corresponding enthalpy of 57 kJ/mole . A large exotherm was observed under conditions that form  $\text{NaH}$  catalyst in the region 640°C to 825 °C which corresponds to at least  $-354 \text{ kJ/mole H}_2$ , greater than that of the most exothermic reaction possible for  $\text{H}$ , the  $-241.8 \text{ kJ/mole H}_2$  enthalpy of the combustion of hydrogen.

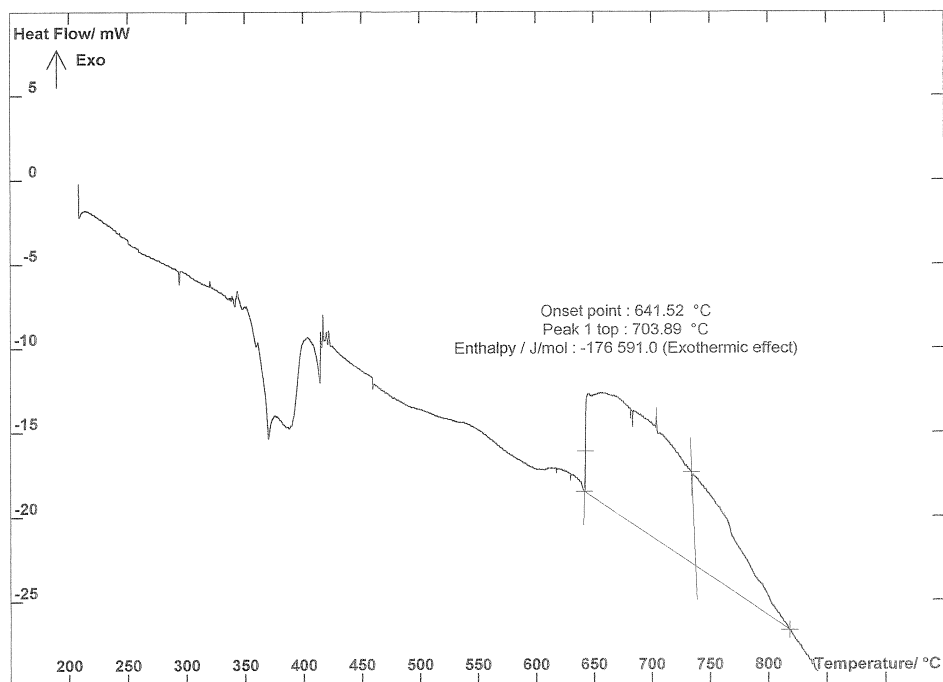


Figure 8. The results of the DSC (100-750 °C) of  $MgH_2$  at a scan rate of 0.1 degree/minute. Two sharp endothermic peaks were observed. A first peak centered at 351.75 °C corresponding to 68.61 kJ/mole  $MgH_2$  matches the 74.4 kJ/mole  $MgH_2$  decomposition energy. The second peak at 647.66 °C corresponding to 6.65 kJ/mole  $MgH_2$  matches the known melting point of  $Mg(m)$  of 650 °C and enthalpy of fusion of 8.48 kJ/mole  $Mg(m)$ . Thus, the expected behavior was observed for the decomposition of a control, noncatalyst hydride.

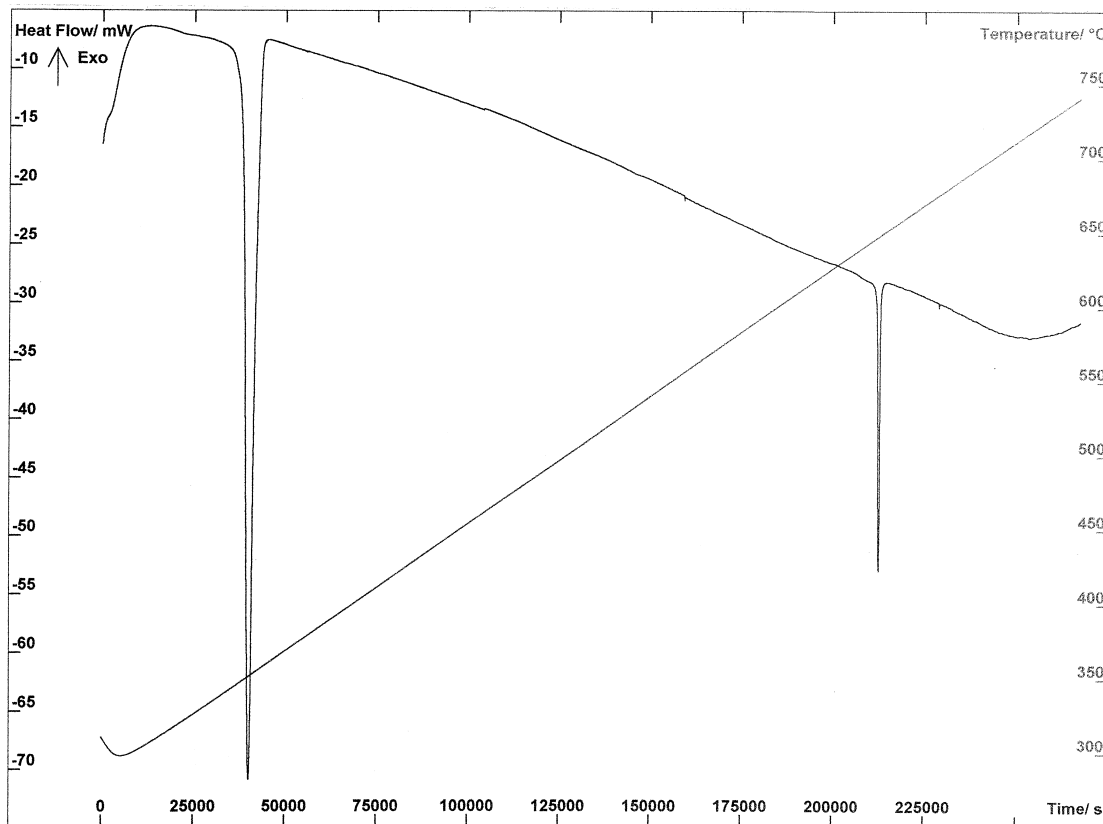


Figure 9. Temperature versus time for the calibration run with an evacuated test cell and resistive heating only.

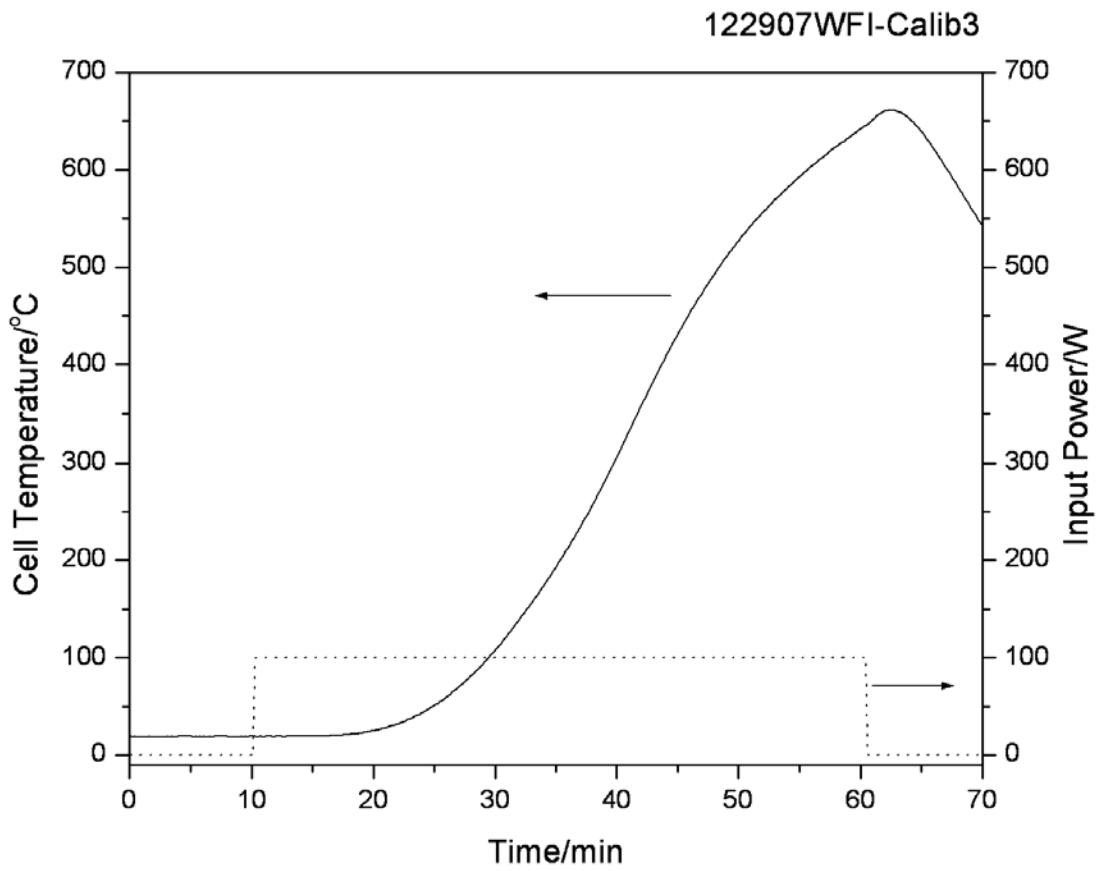


Figure 10. Power versus time for the calibration run with an evacuated test cell and resistive heating only. The numerical integration of the input and output power curves yielded an output energy of 292.2 kJ and an input energy of 303.1 kJ corresponding to a coupling of flow of 96.4% of the resistive input to the output coolant.

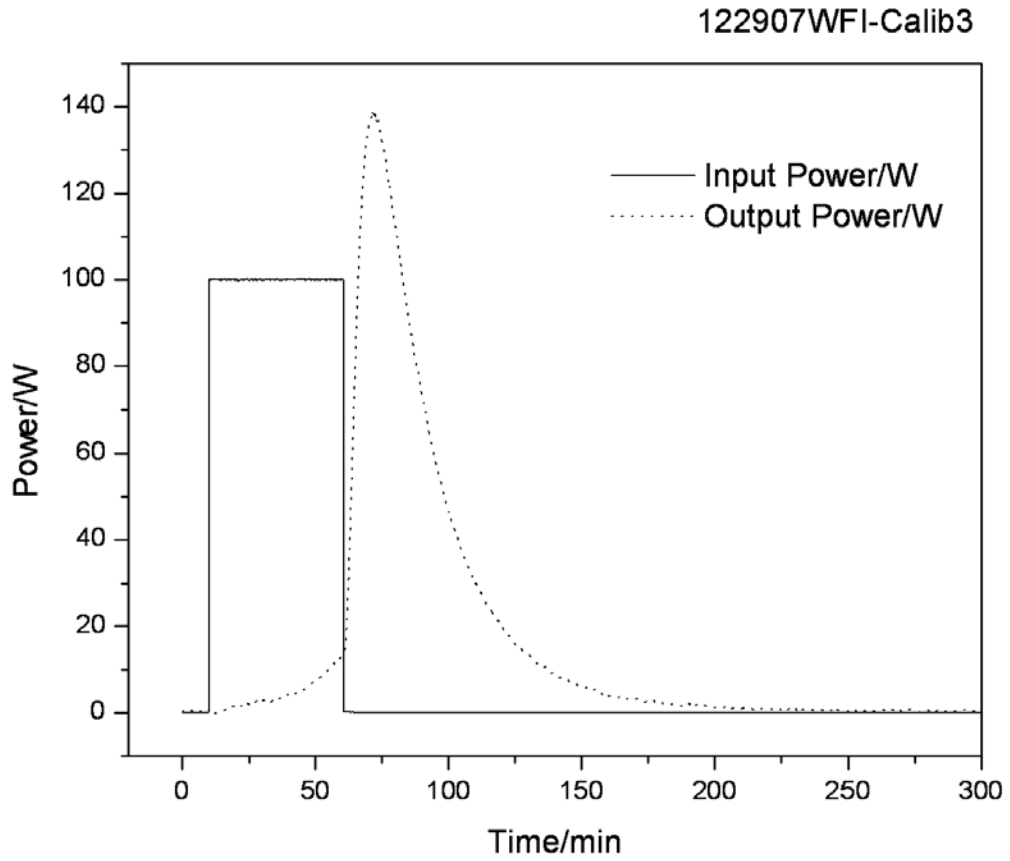


Figure 11. The cell temperature with time for the hydriano reaction with the cell containing the reagents comprising the catalyst material, 1g *Li*, 0.5g *LiNH<sub>2</sub>*, 10g *LiBr*, and 15g *Pd/Al<sub>2</sub>O<sub>3</sub>*. The reaction liberated 19.1 kJ of energy in less than 120 s to develop a system-response-corrected peak power in excess of 160 W.

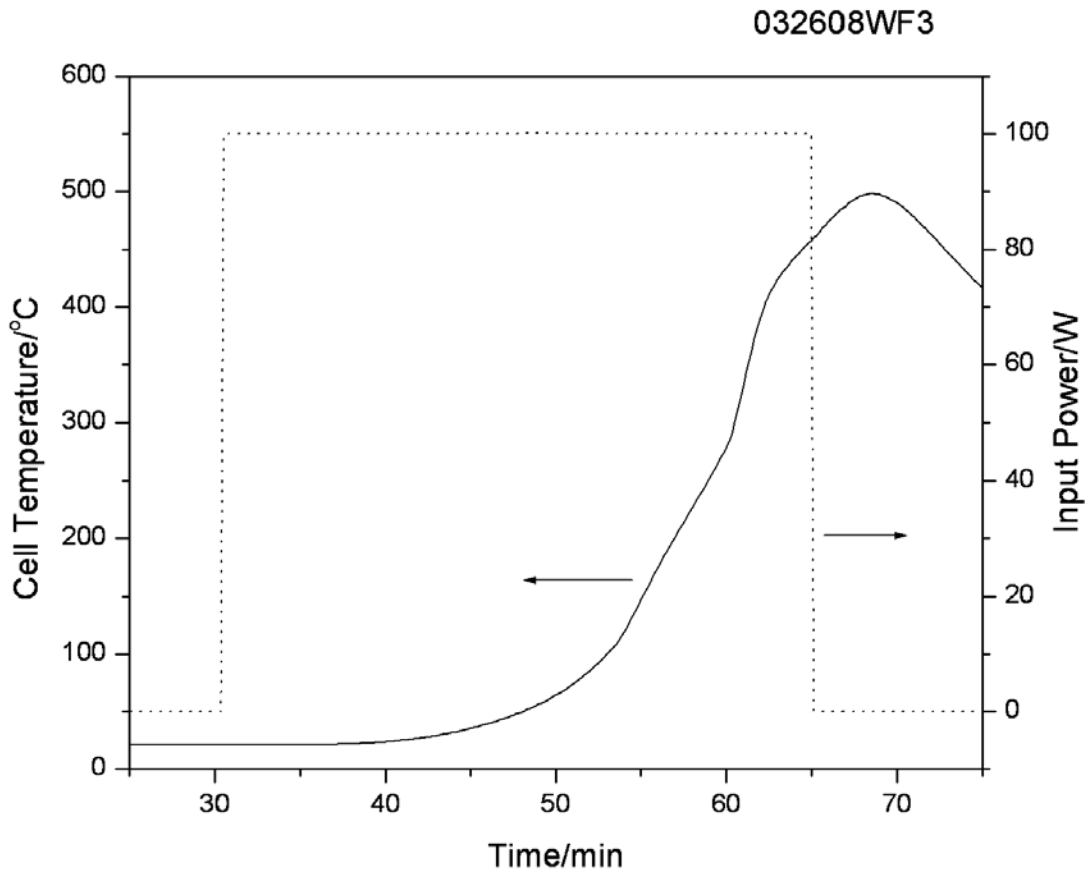


Figure 12. The coolant power with time for the hydrino reaction with the cell containing the reagents comprising the catalyst material, 1g *Li*, 0.5g *LiNH<sub>2</sub>*, 10g *LiBr*, and 15g *Pd/Al<sub>2</sub>O<sub>3</sub>*. The numerical integration of the input and output power curves with the calibration correction applied yielded an output energy of 227.2 kJ and an input energy of 208.1 kJ corresponding to an excess energy of 19.1 kJ.

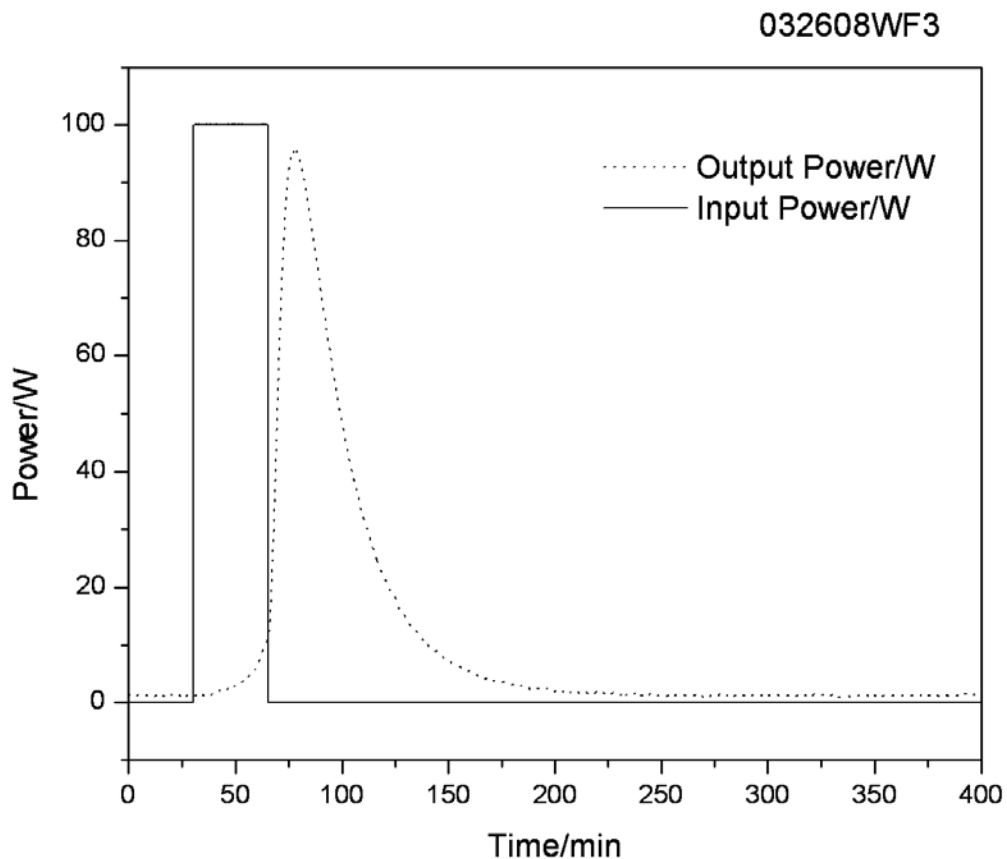


Figure 13. The cell temperature with time for the R-Ni control power test with the cell containing the reagents comprising the starting material for R-Ni, 15g R-Ni/Al alloy powder, and 3.28g of Na.

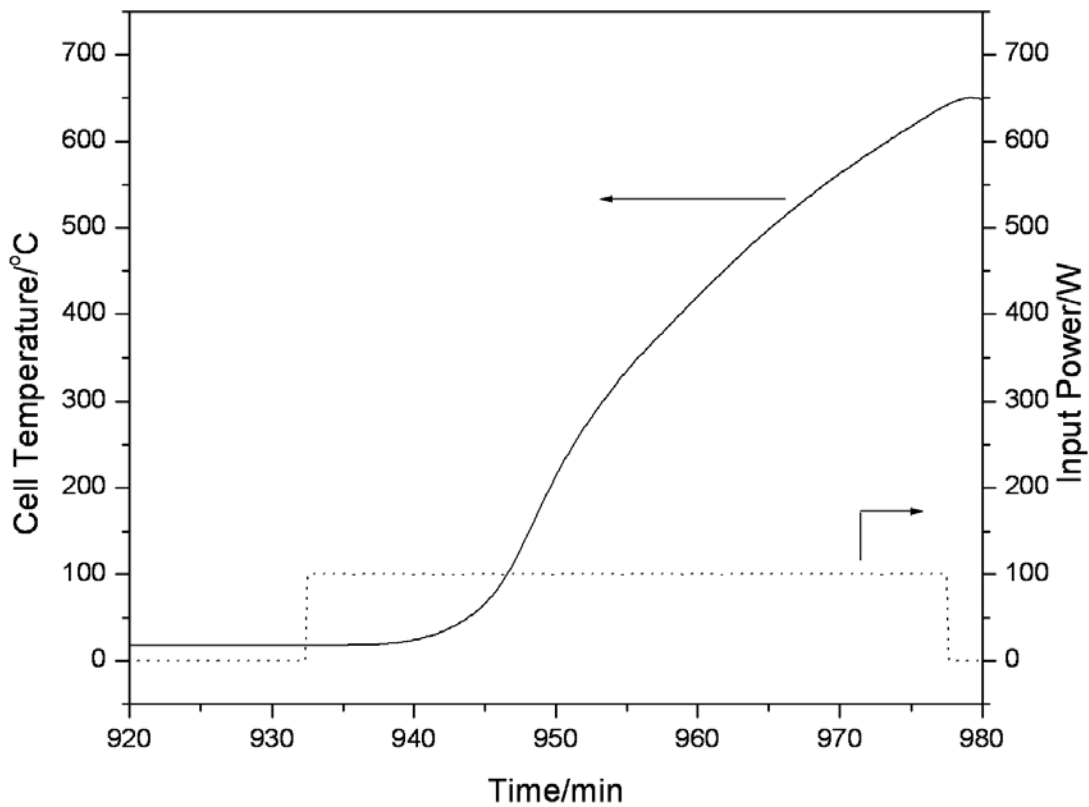


Figure 14. The coolant power with time for the control power test with the cell containing the reagents comprising the starting material for R-Ni, 15g R-Ni/Al alloy powder, and 3.28g of Na. Energy balance was obtained with the calibration-corrected numerical integration of the input and output power curves yielding an output energy of 384 kJ and an input energy of 385 kJ.

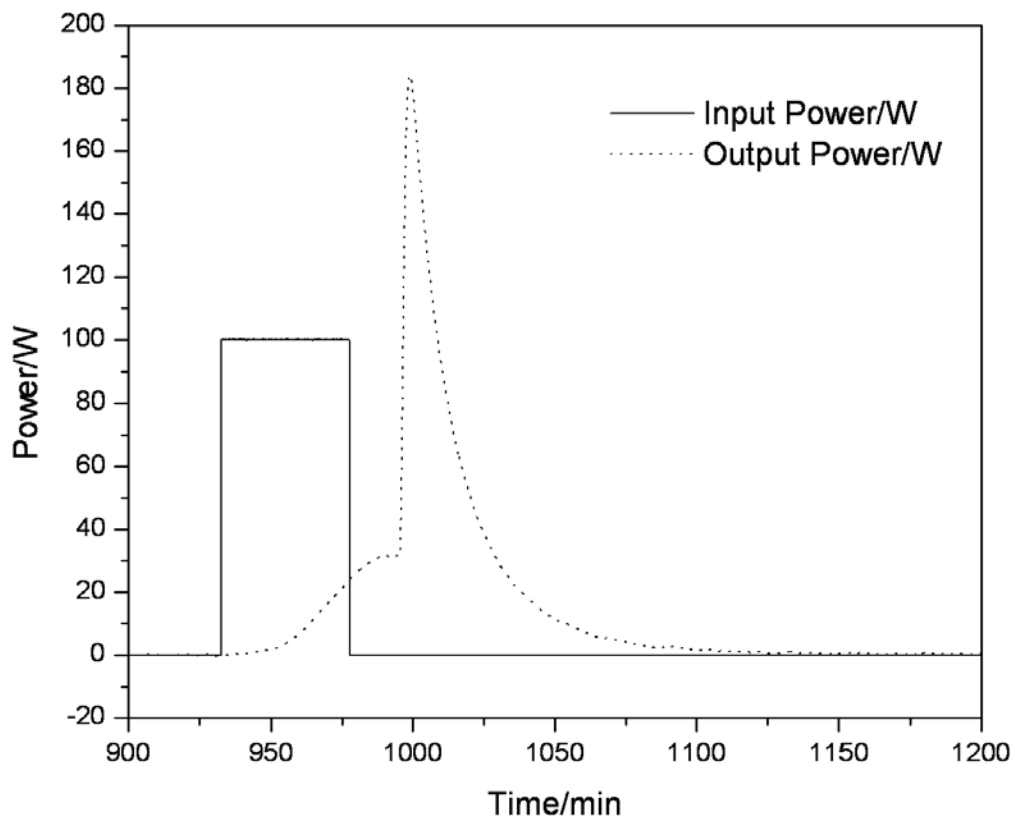


Figure 15. The cell temperature with time for the hydrido reaction with the cell containing the reagents comprising the catalyst material, 15g *NaOH*-doped R-Ni 2800, and 3.28g of Na. The reaction liberated 36 kJ of energy in less than 90 s to develop a system-response-corrected peak power in excess of 0.5 kW.

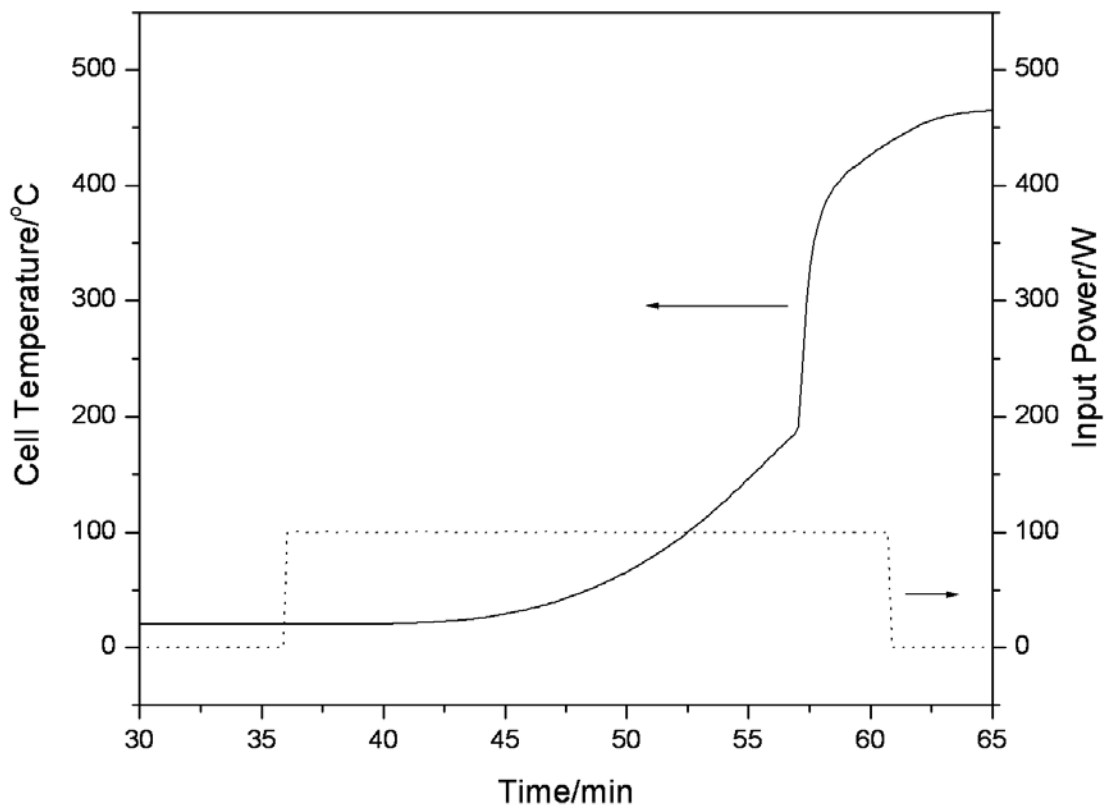


Figure 16. The coolant power with time for the hydriano reaction with the cell containing the reagents comprising the catalyst material, 15g *NaOH*-doped R-Ni 2800, and 3.28g of Na. The numerical integration of the input and output power curves with the calibration correction applied yielded an output energy of 185.1 kJ and an input energy of 149.1 kJ corresponding to an excess energy of 36 kJ.

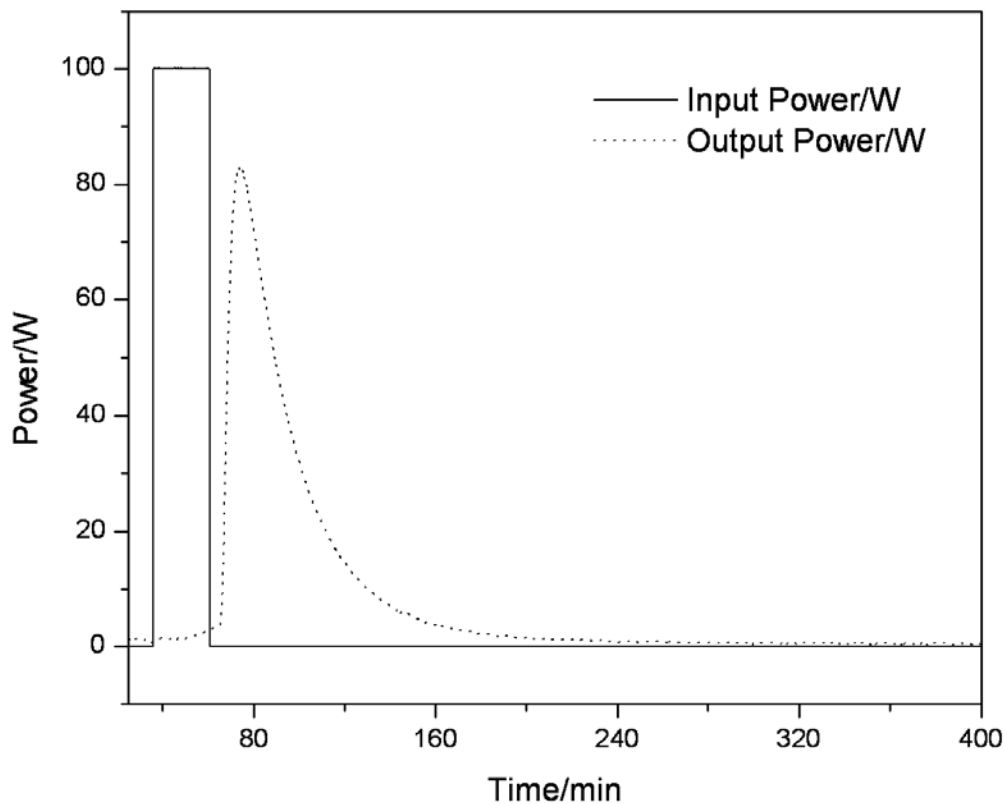


Figure 17. The cell temperature with time for the hydrino reaction with the cell containing the reagents comprising the catalyst material, 15g *NaOH*-doped R-Ni 2400. The cell temperature jumped from 60°C to 205°C in 60 s wherein the reaction liberated 11.7 kJ of energy in less time to develop a system-response-corrected peak power in excess of 0.25 kW.

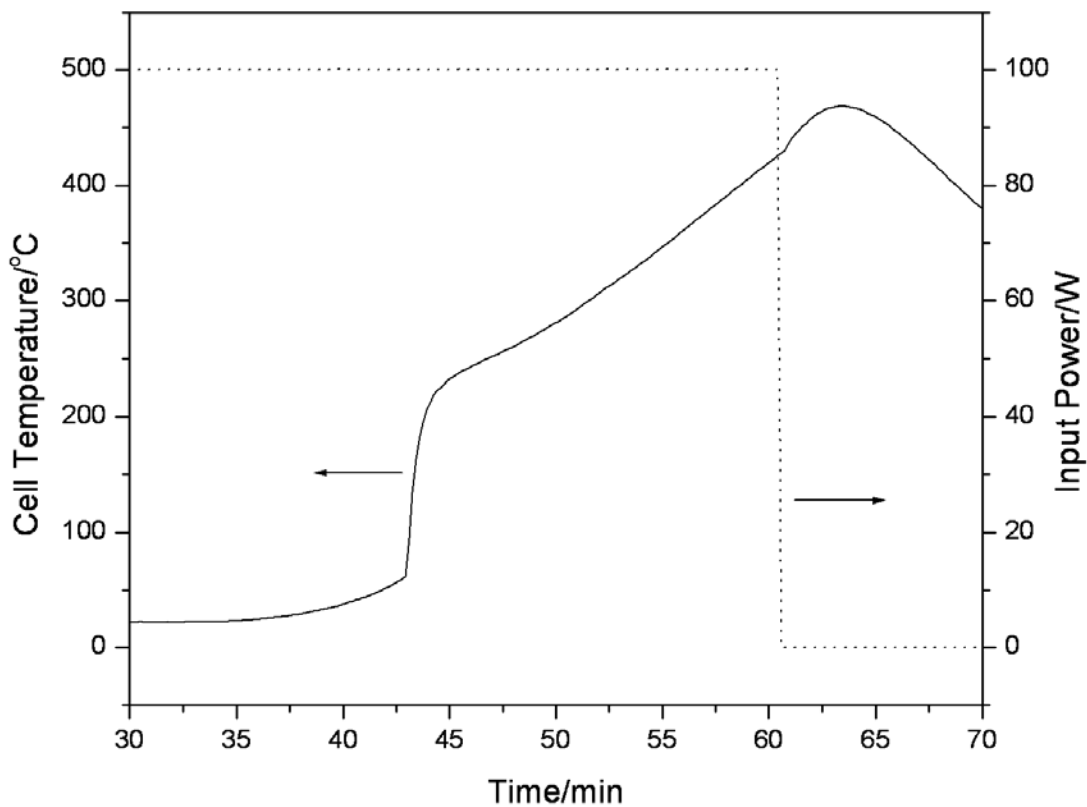


Figure 18. The coolant power with time for the hydrino reaction with the cell containing the reagents comprising the catalyst material, 15g *NaOH*-doped R-Ni 2400. The numerical integration of the input and output power curves with the calibration correction applied yielded an output energy of 195.7 kJ and an input energy of 184.0 kJ corresponding to an excess energy of 11.7 kJ.

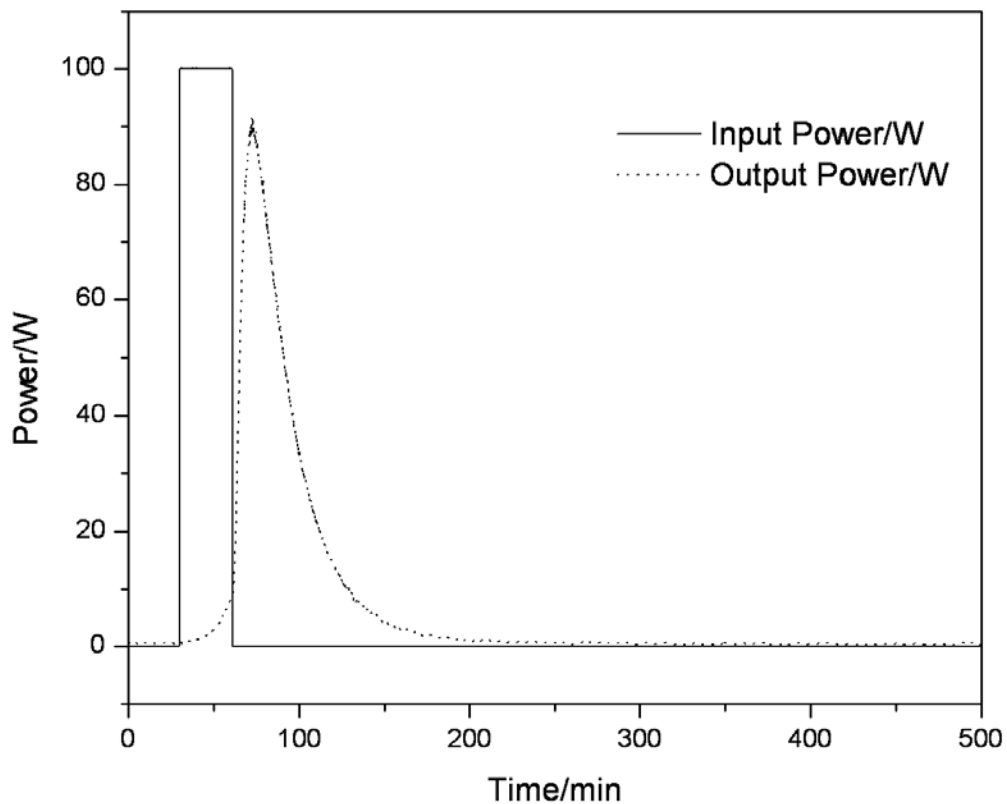


Figure 19. Temperature versus time for the scale-up cell calibration run with an evacuated test cell and resistive heating only.

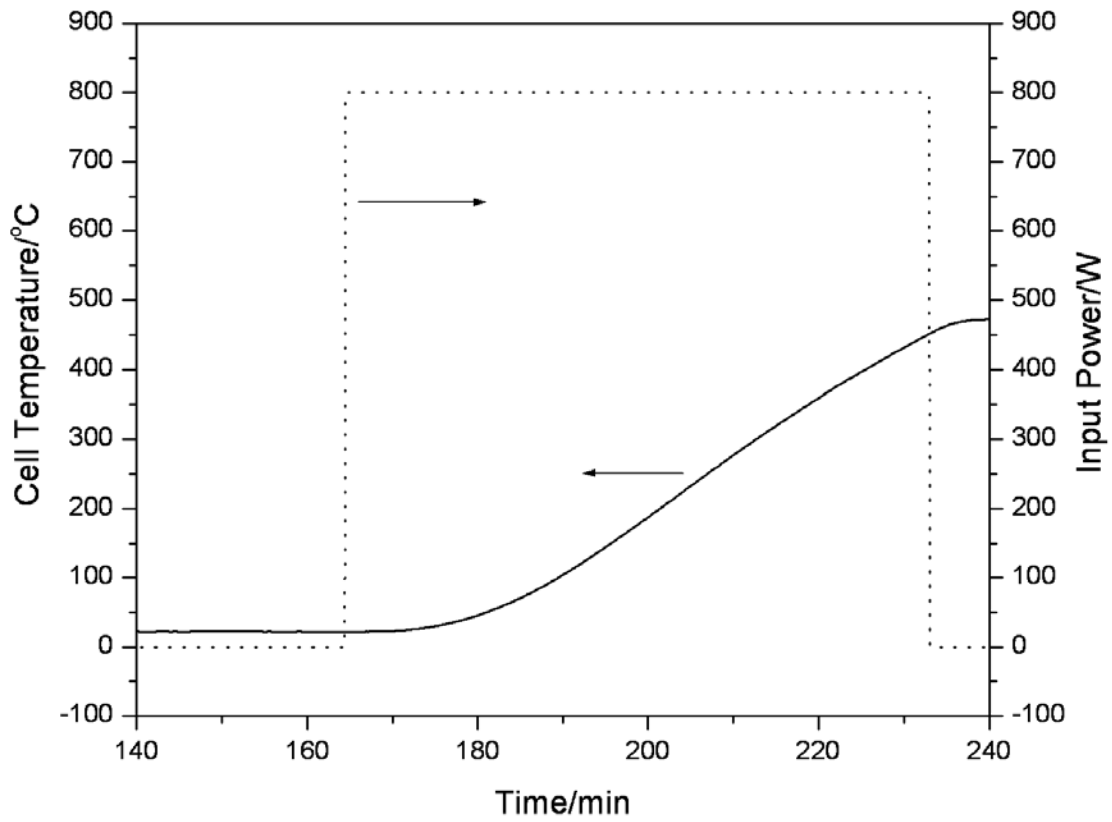


Figure 20. Power versus time for the scale-up cell calibration run with an evacuated test cell and resistive heating only. The numerical integration of the input and output power curves yielded an output energy of 3284.1 kJ and an input energy of 3292.1 kJ corresponding to a coupling of flow of 99.76% of the resistive input to the output coolant.

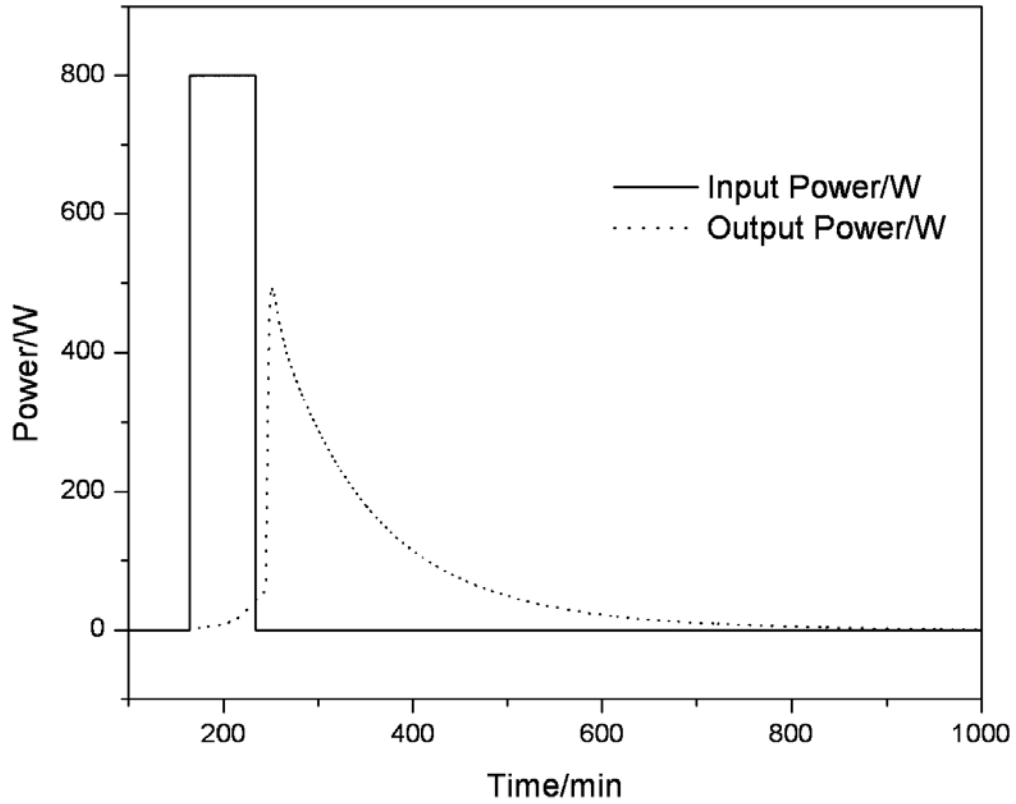


Figure 21. The cell temperature with time for the hydri-no reaction with the scale-up cell containing the reagents comprising the catalyst material, 1kg *NaOH*-doped R-Ni 2400. The cell temperature jumped from 85.6°C to 518°C in 35 s wherein the reaction liberated 753.1 kJ of energy in less time to develop a system-response-corrected peak power in excess of 50 kW.

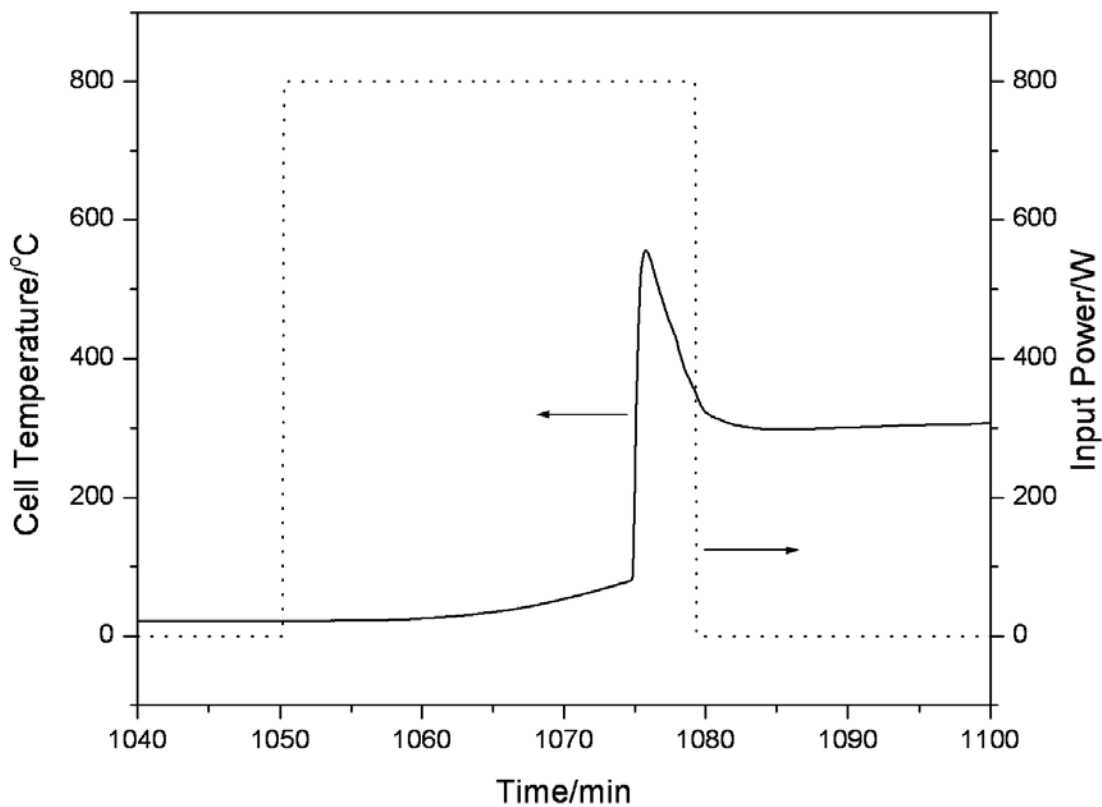


Figure 22. The coolant power with time for the hydrino reaction with the scale-up cell containing the reagents comprising the catalyst material, 1kg *NaOH*-doped R-Ni 2400. The numerical integration of the input and output power curves with the calibration correction applied yielded an output energy of 2149.1 kJ and an input energy of 1396 kJ corresponding to an excess energy of 753.1 kJ.

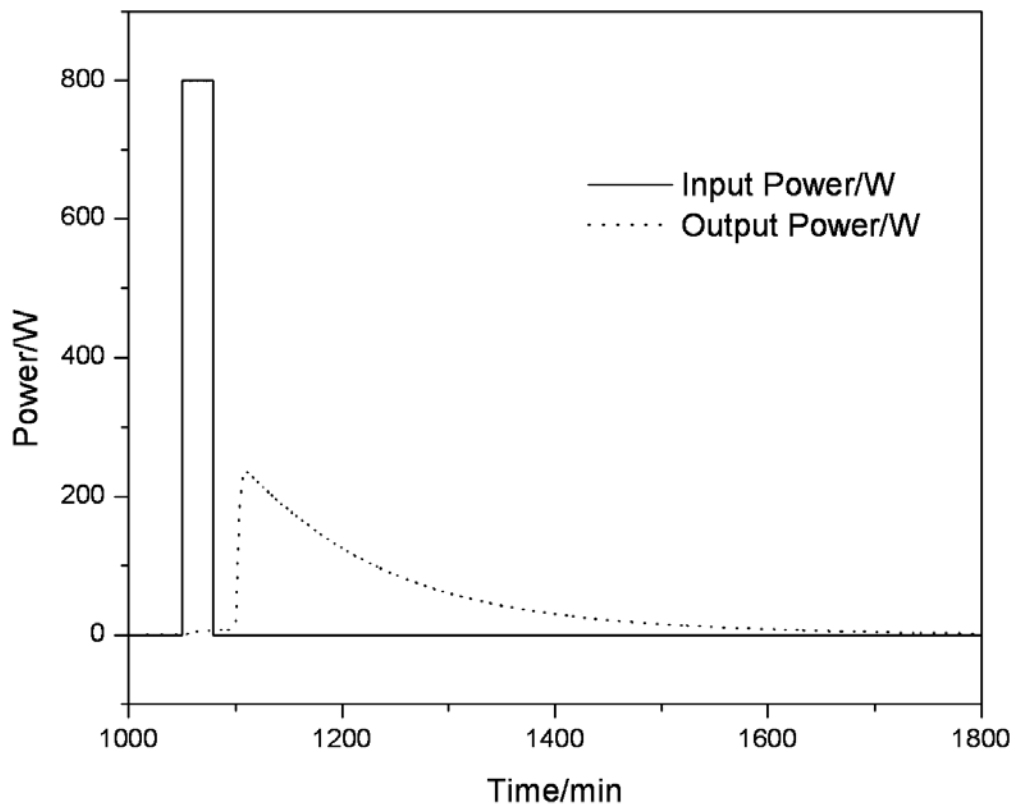


Figure 23. The positive ToF-SIMS spectrum ( $m/e = 0-100$ ) of *LiBr*.

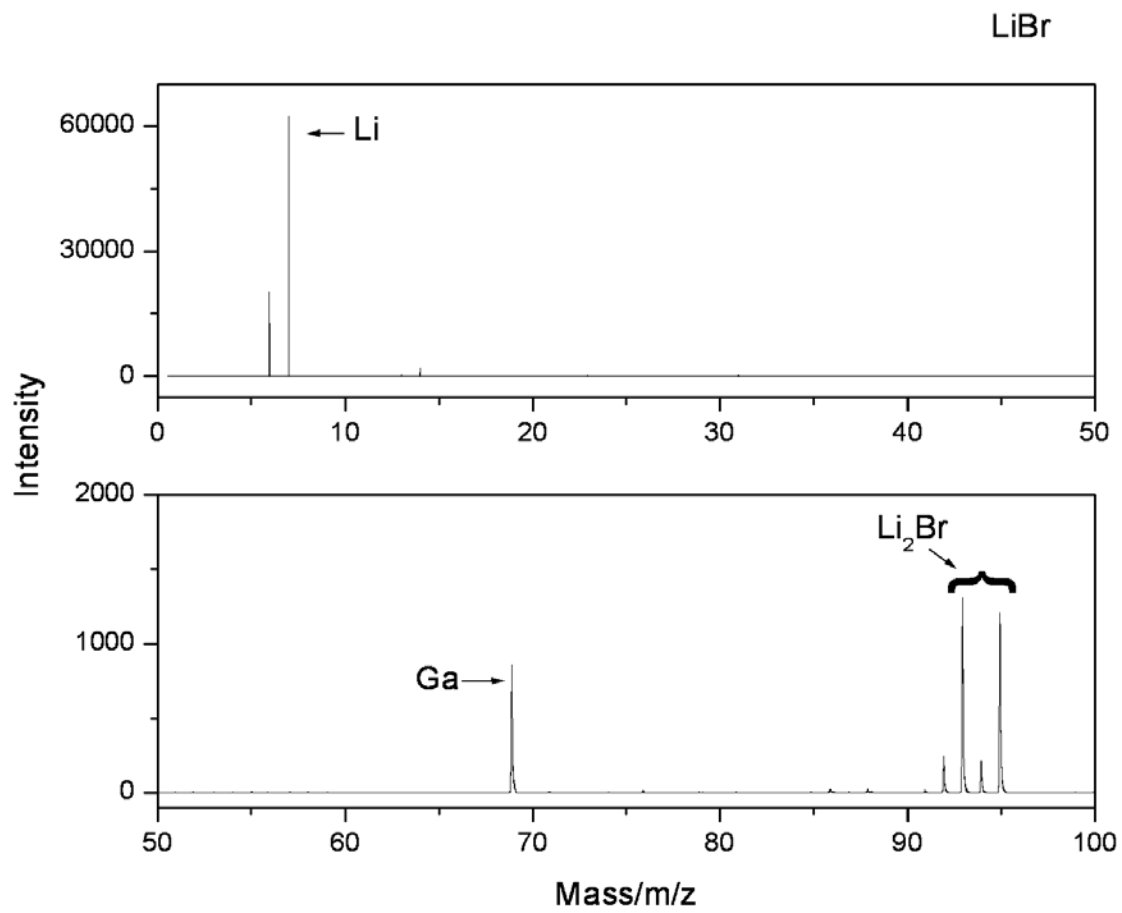


Figure 24. The positive ToF-SIMS spectrum ( $m/e = 0-100$ ) of the  $LiH^*Br$  crystals.

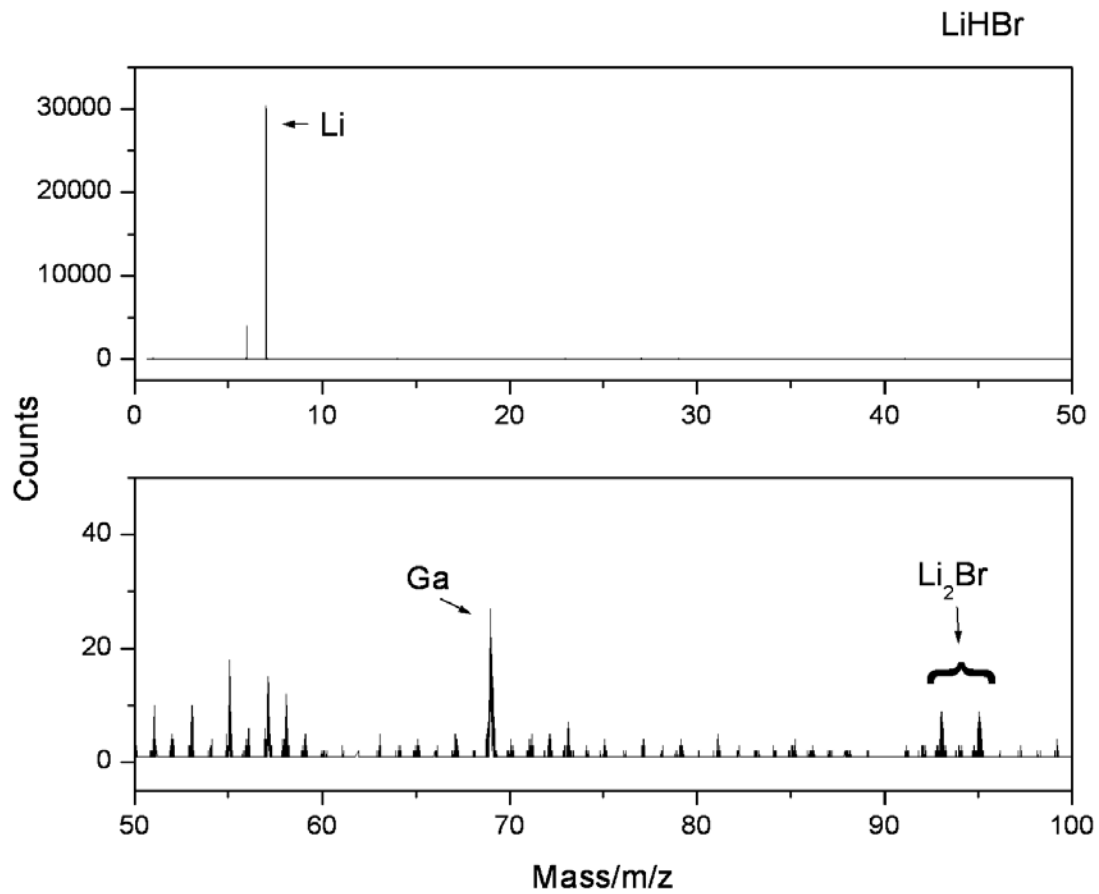


Figure 25. The negative ToF-SIMS spectrum ( $m/e = 0-100$ ) of *LiBr*.

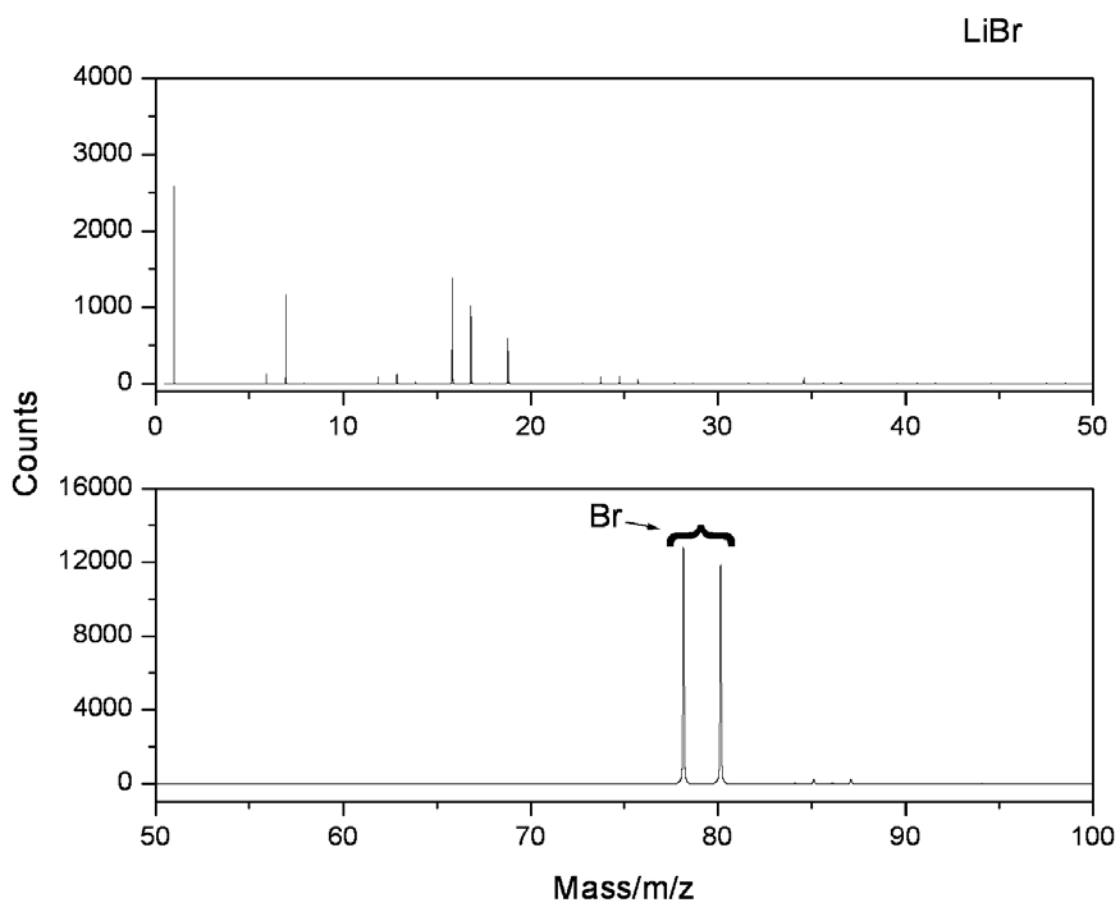


Figure 26. The negative ToF-SIMS spectrum ( $m/e=0-100$ ) of the  $LiH * Br$  crystals. A dominant hydride,  $LiHBr^-$ , and  $Li_2H_2Br^-$  peaks were uniquely observed.

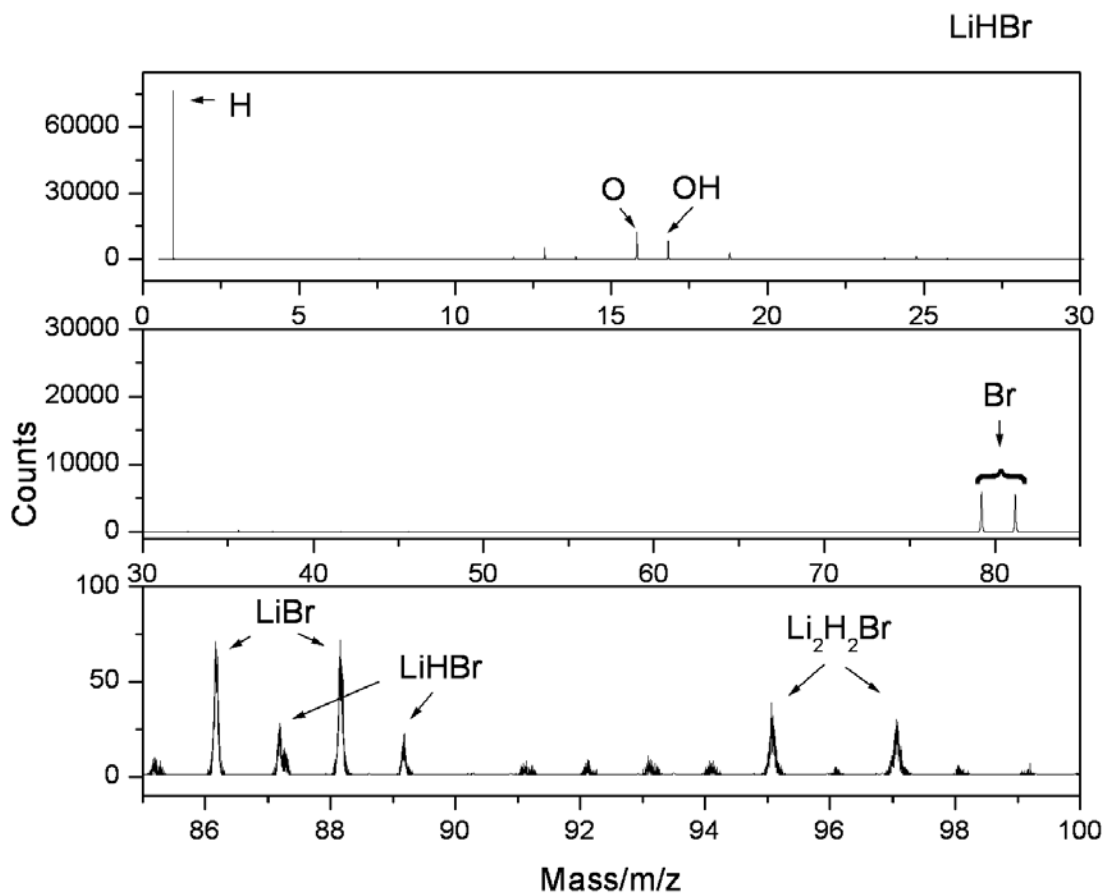


Figure 27. The positive ToF-SIMS spectrum ( $m/e = 0 - 200$ ) of  $LiI$ .

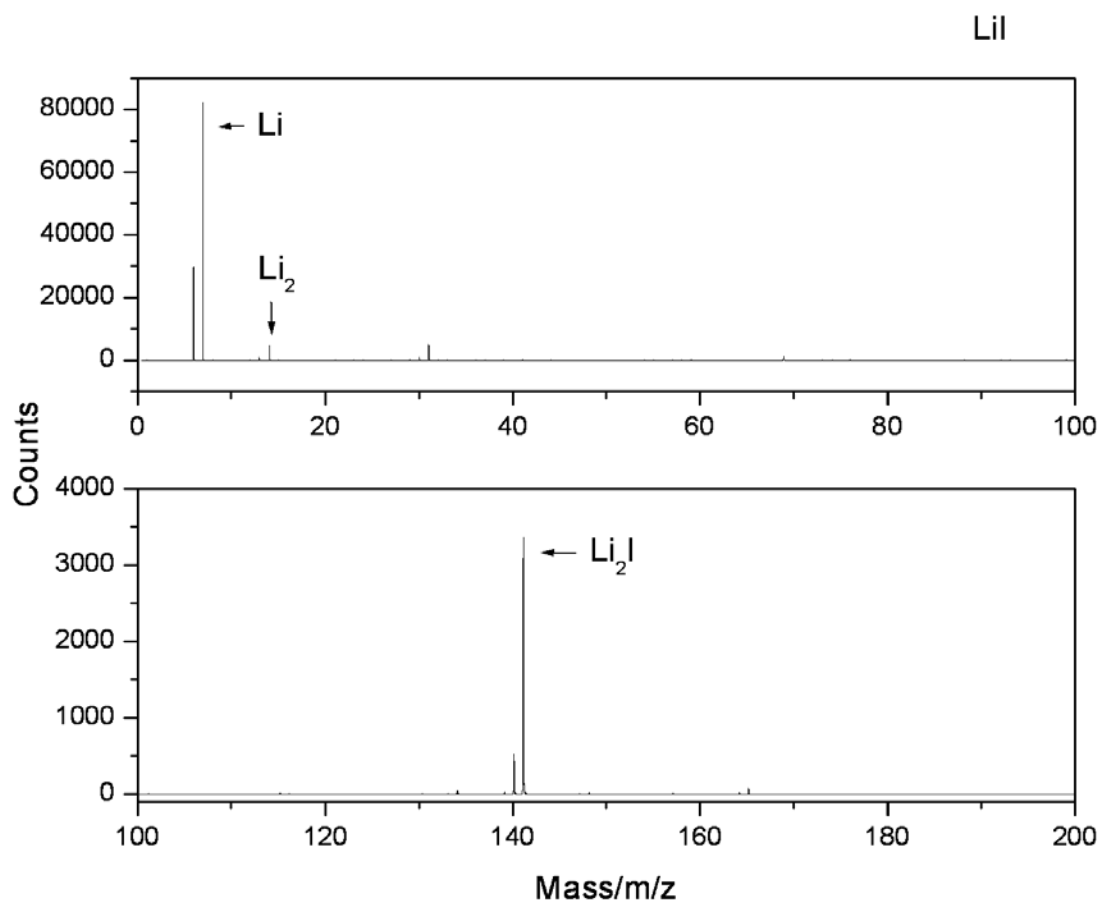


Figure 28. The positive ToF-SIMS spectrum ( $m/e = 0 - 200$ ) of the  $LiH * I$  crystals.  $LiHI^+$ ,  $Li_2H_2I^+$ ,  $Li_4H_2I^+$ , and  $Li_6H_2I^+$  were only observed in the positive ion spectrum of the  $LiH * I$  crystals.

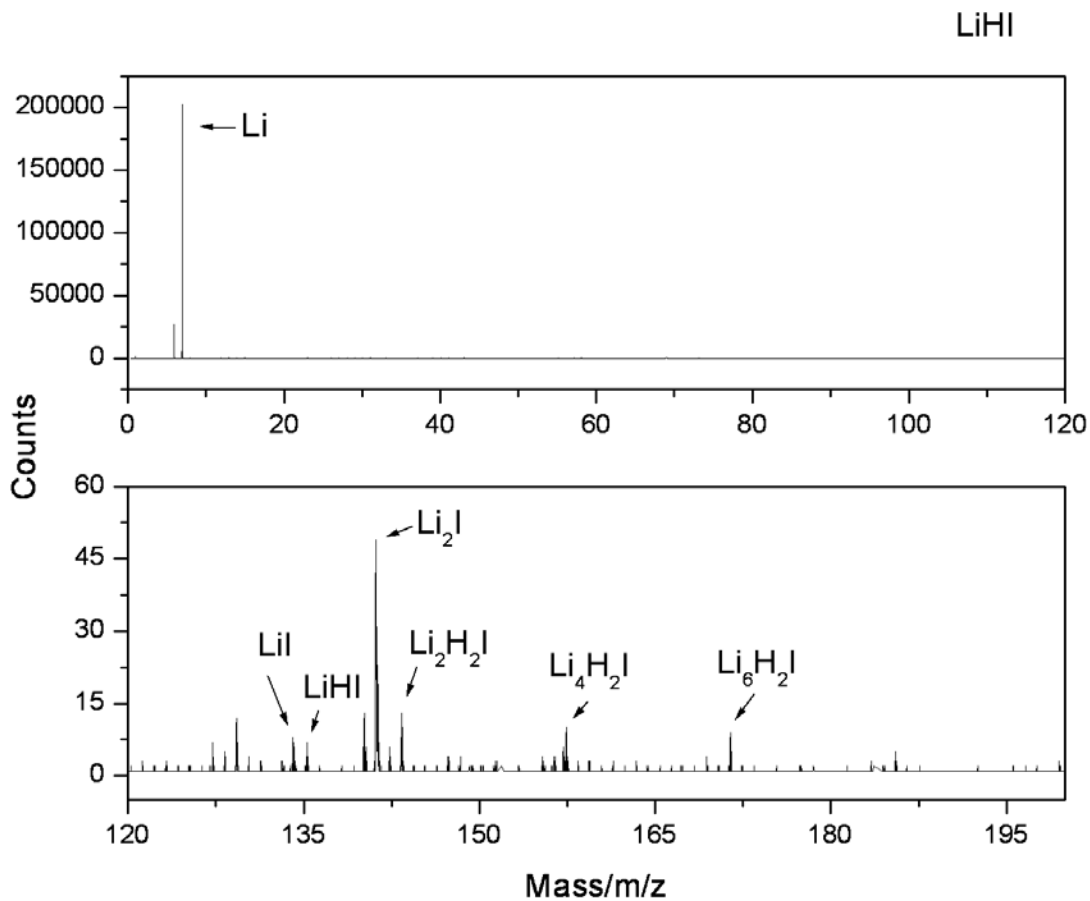


Figure 29. The negative ToF-SIMS spectrum ( $m/e = 0-180$ ) of *LiI*.

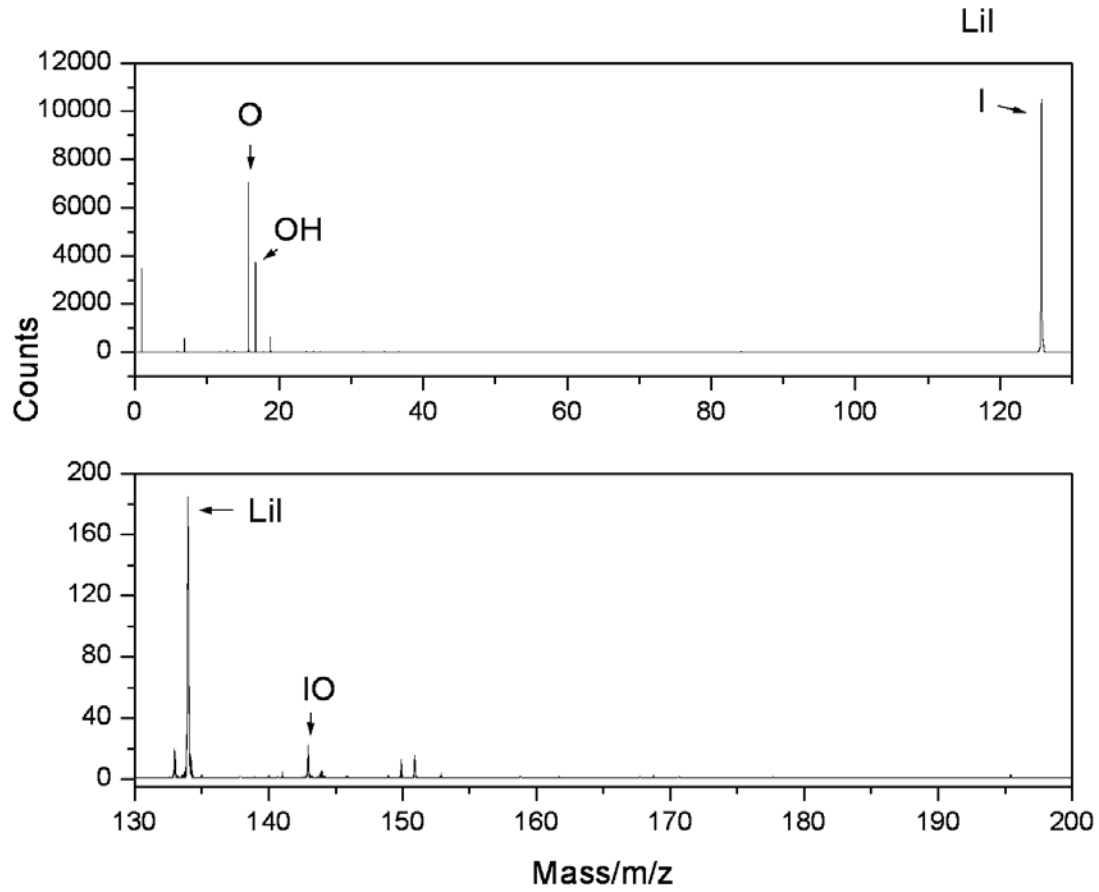


Figure 30. The negative ToF-SIMS spectrum ( $m/e=0-180$ ) of the  $LiH^*I$  crystals. A dominant hydride,  $LiHI^-$ ,  $Li_2H_2I^-$ , and  $NaHI^-$  peaks were uniquely observed.

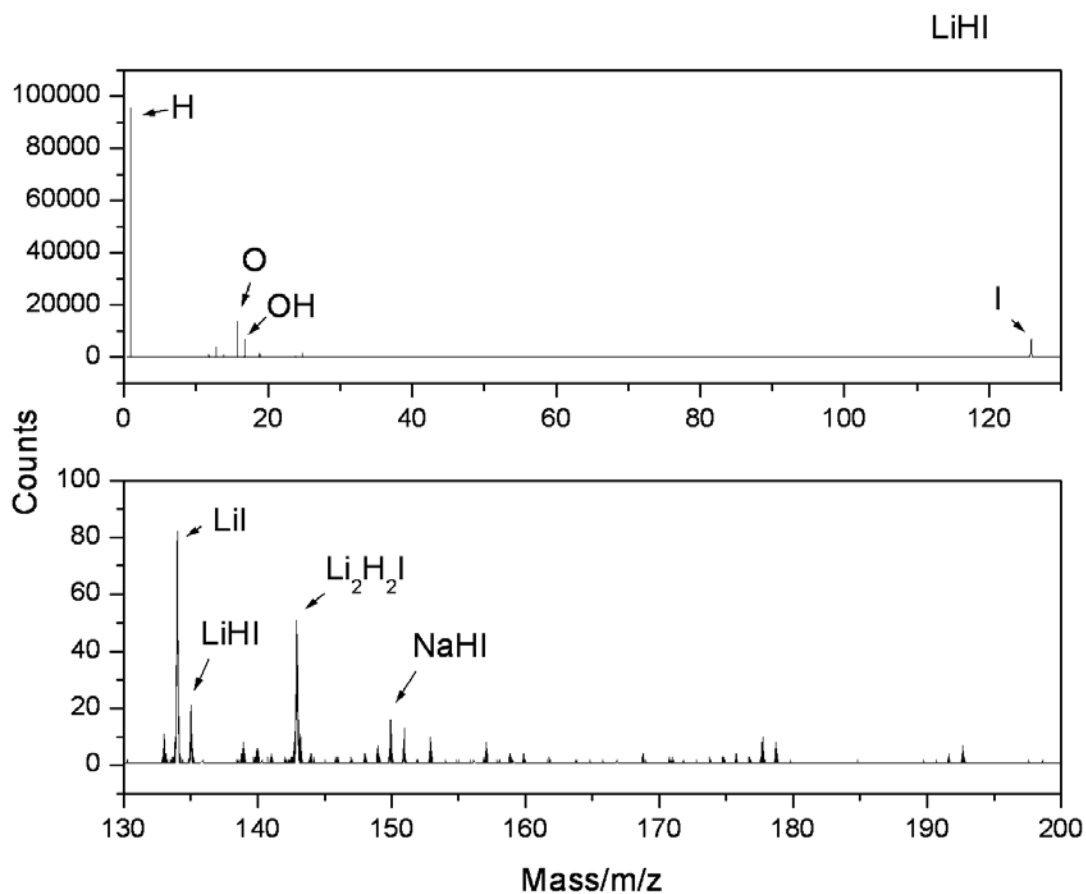


Figure 31. The negative ToF-SIMS spectrum ( $m/e = 20-30$ ) of  $\text{NaH}^*$ -coated  $\text{Pt}/\text{Ti}$  following the production of 15 kJ of excess heat. Hydrino hydride compounds  $\text{NaH}_x^-$  were observed.

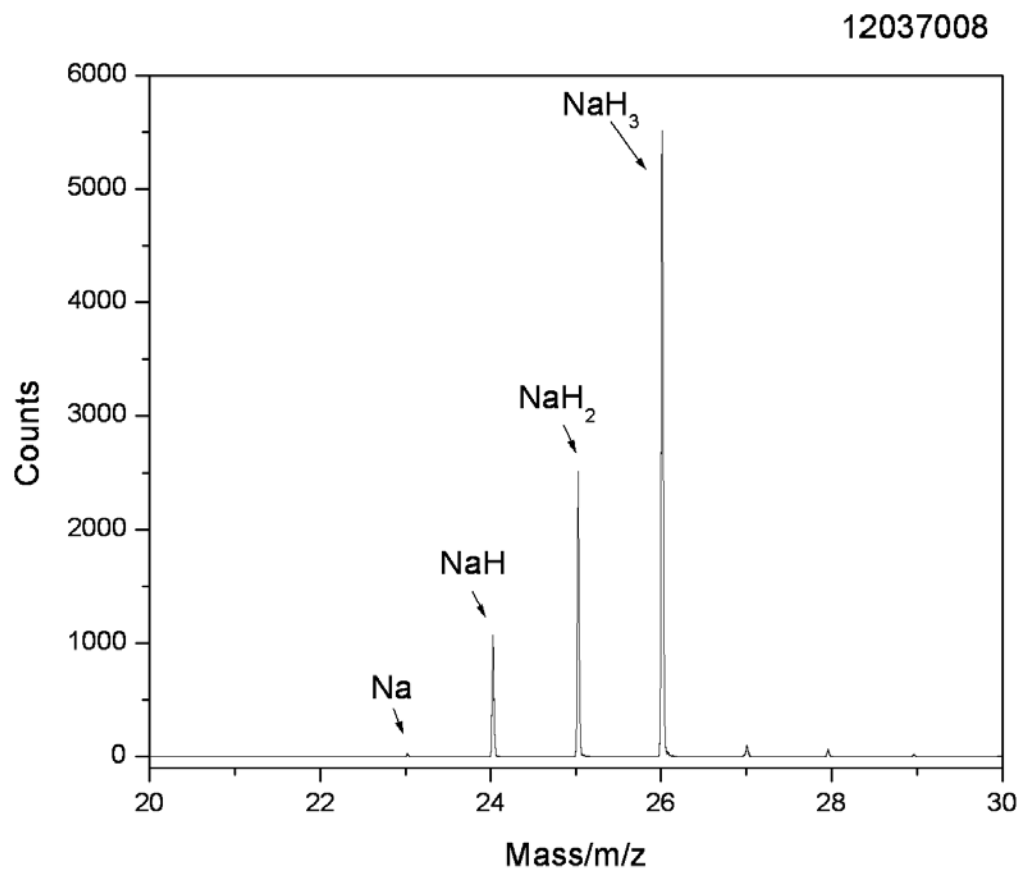


Figure 32. The positive ToF-SIMS spectrum ( $m/e = 0-100$ ) of R-Ni reacted over a 48 hour period at 50°C. The dominant ion on the surface was  $Na^+$  consistent with  $NaOH$  doping of the surface. The ions of the other major elements of R-Ni 2400 such as  $Al^+$ ,  $Ni^+$ ,  $Cr^+$ , and  $Fe^+$  were also observed.

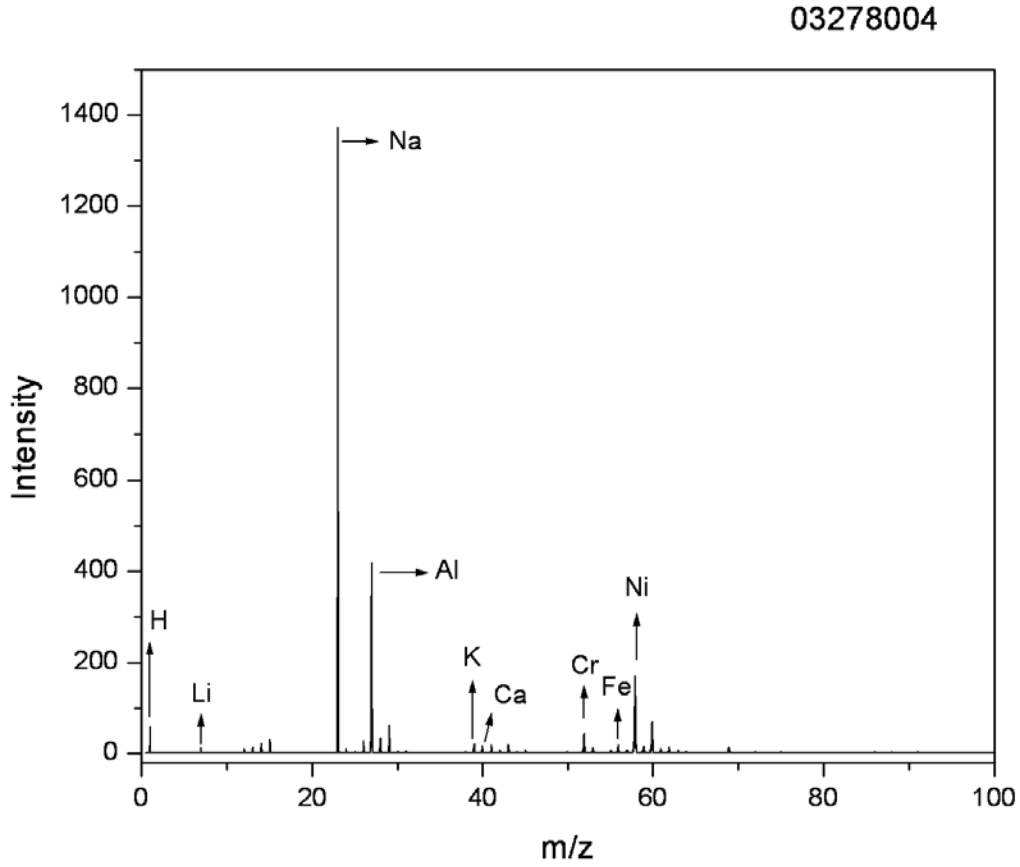
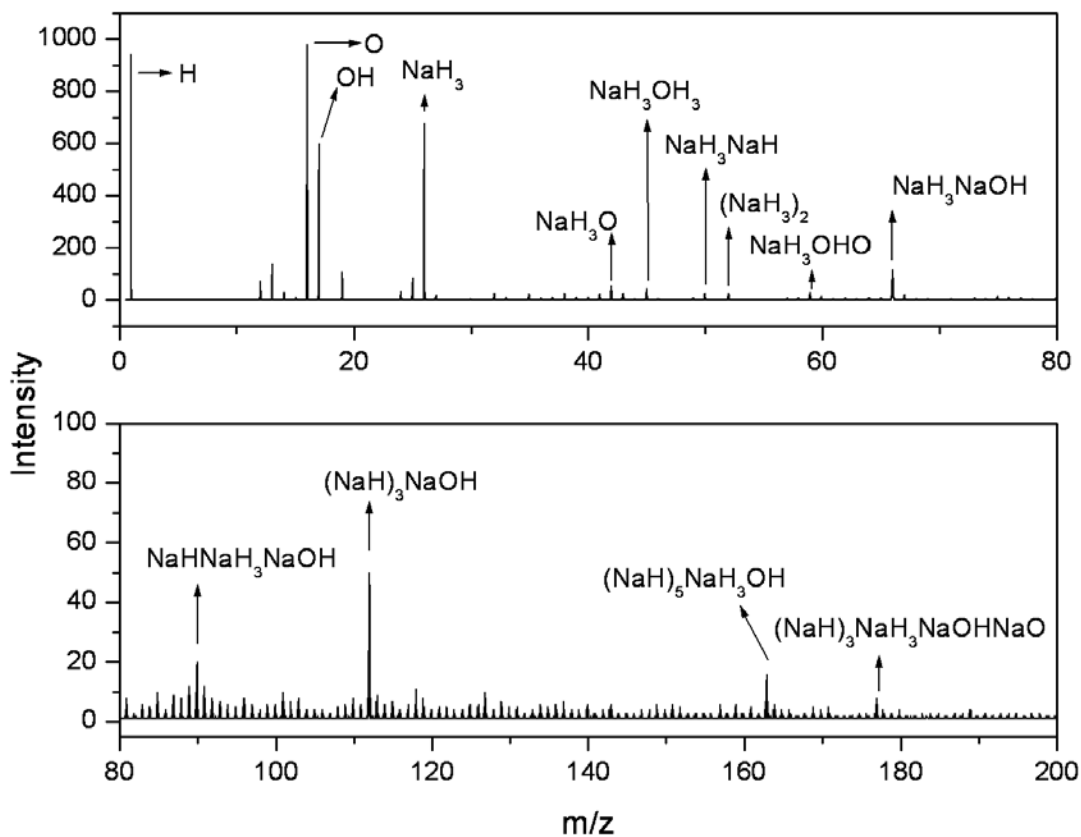
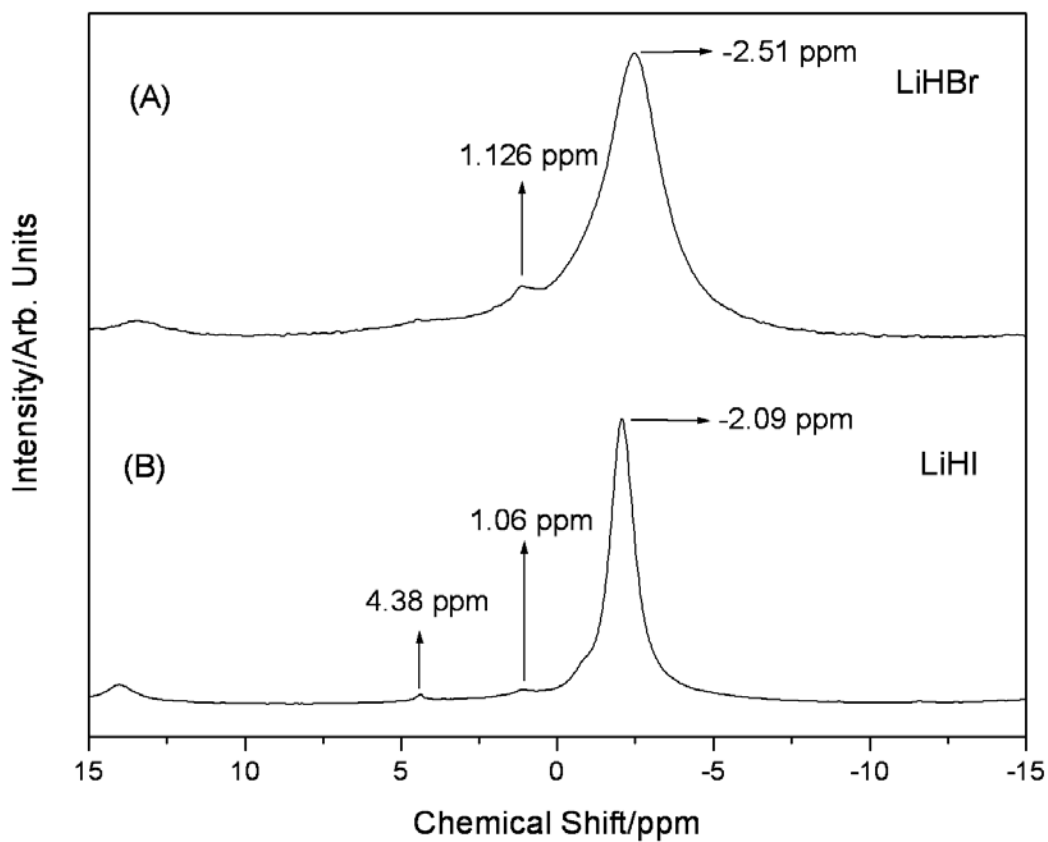


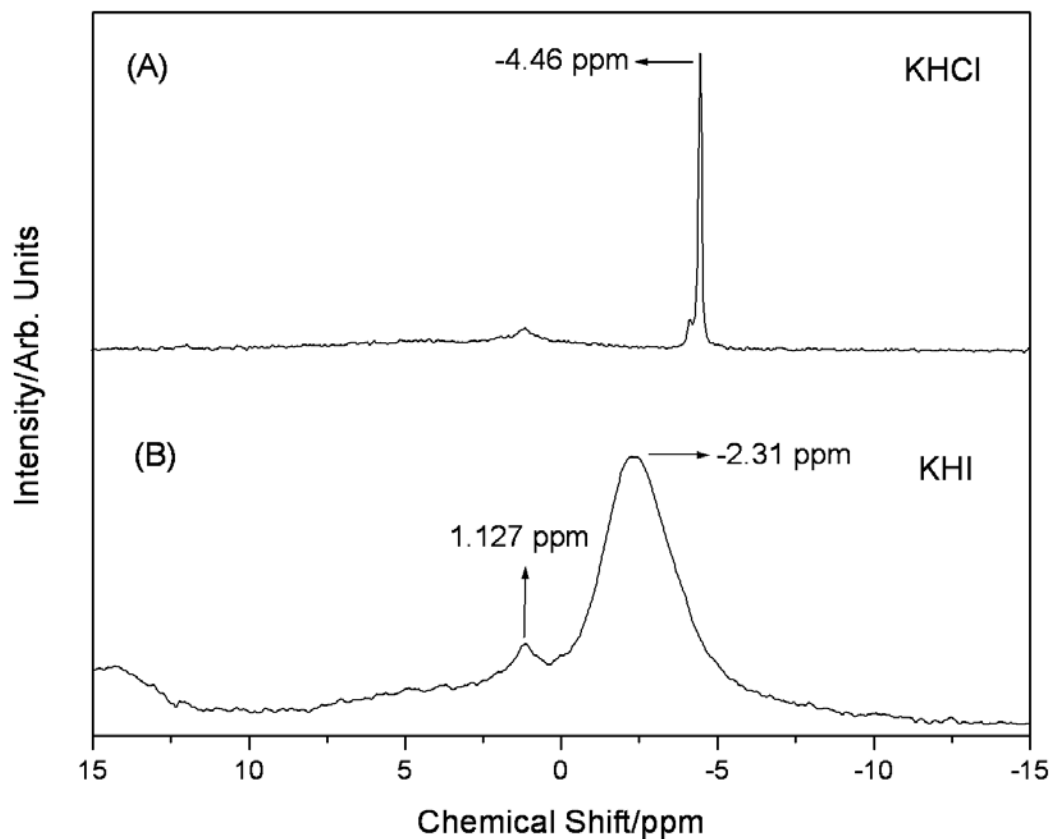
Figure 33. The negative ToF-SIMS spectrum ( $m/e = 0-180$ ) of R-Ni reacted over a 48 hour period at  $50^{\circ}\text{C}$ . A dominant hydride,  $\text{NaH}_3^-$  and  $\text{NaH}_3\text{NaOH}^-$  assigned to sodium hydrino hydride and this ion in combination with  $\text{NaOH}$ , as well as other unique ions assignable to sodium hydrino hydrides  $\text{NaH}_x^-$  in combinations with  $\text{NaOH}$ ,  $\text{NaO}$ ,  $\text{OH}^-$  and  $\text{O}^-$  were observed.



Figures 34A-B.  $^1\text{H}$  MAS NMR spectra relative to external TMS. (A)  $\text{LiH}^*\text{Br}$  showing a broad  $-2.5$  ppm upfield-shifted peak and a peak at  $1.13$  ppm assigned to  $\text{H}^-(1/4)$  and  $\text{H}_2(1/4)$ , respectively. (B)  $\text{LiH}^*\text{I}$  showing a broad  $-2.09$  ppm upfield-shifted peak assigned to  $\text{H}^-(1/4)$  and peaks at  $1.06$  ppm and  $4.38$  ppm assigned to  $\text{H}_2(1/4)$  and  $\text{H}_2$ , respectively.



Figures 35A-B.  $^1\text{H}$  MAS NMR spectra relative to external TMS. (A)  $\text{KH}^*\text{Cl}$  showing a very sharp  $-4.46$  ppm upfield-shifted peak corresponding to an environment that is essentially that of a free ion. (B)  $\text{KH}^*\text{I}$  showing a broad  $-2.31$  ppm upfield-shifted peak similar to the case of  $\text{LiH}^*\text{Br}$  and  $\text{LiH}^*\text{I}$ . Both spectra also had a  $1.13$  ppm peak assigned to  $\text{H}_2(1/4)$ .



Figures 36A-B.  $^1\text{H}$  MAS NMR spectra relative to external TMS showing an H-content selectivity of  $\text{LiH}^*X$  for molecular species alone based on the nonpolarizability of the halide and the corresponding nonreactivity towards  $\text{H}^-(1/4)$ . (A)  $\text{LiH}^*F$  comprising a nonpolarizable fluorine showing peaks at 4.31 ppm assigned to  $\text{H}_2$  and 1.16 ppm assigned to  $\text{H}_2(1/4)$  and the absence of the  $\text{H}^-(1/4)$  ion peak. (B)  $\text{LiH}^*Cl$  comprising a nonpolarizable chlorine showing peaks at 4.28 ppm assigned to  $\text{H}_2$  and 1.2 ppm assigned to  $\text{H}_2(1/4)$  and the absence of the  $\text{H}^-(1/4)$  ion peak.

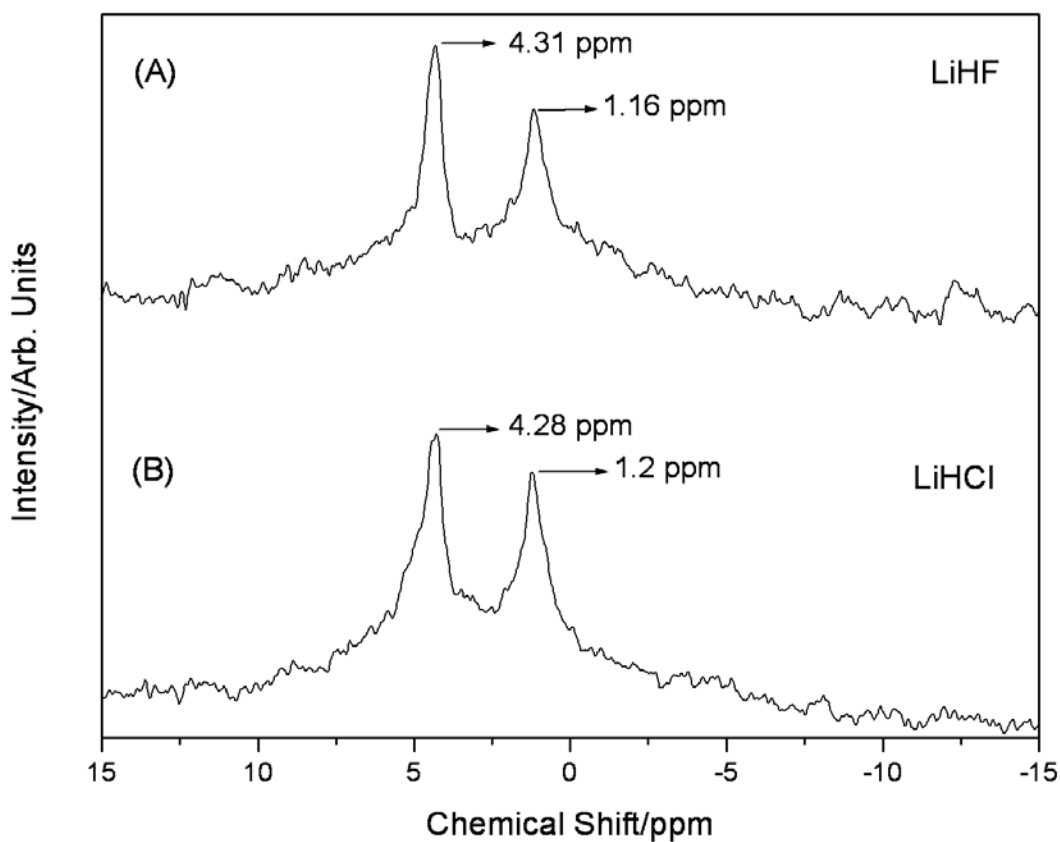
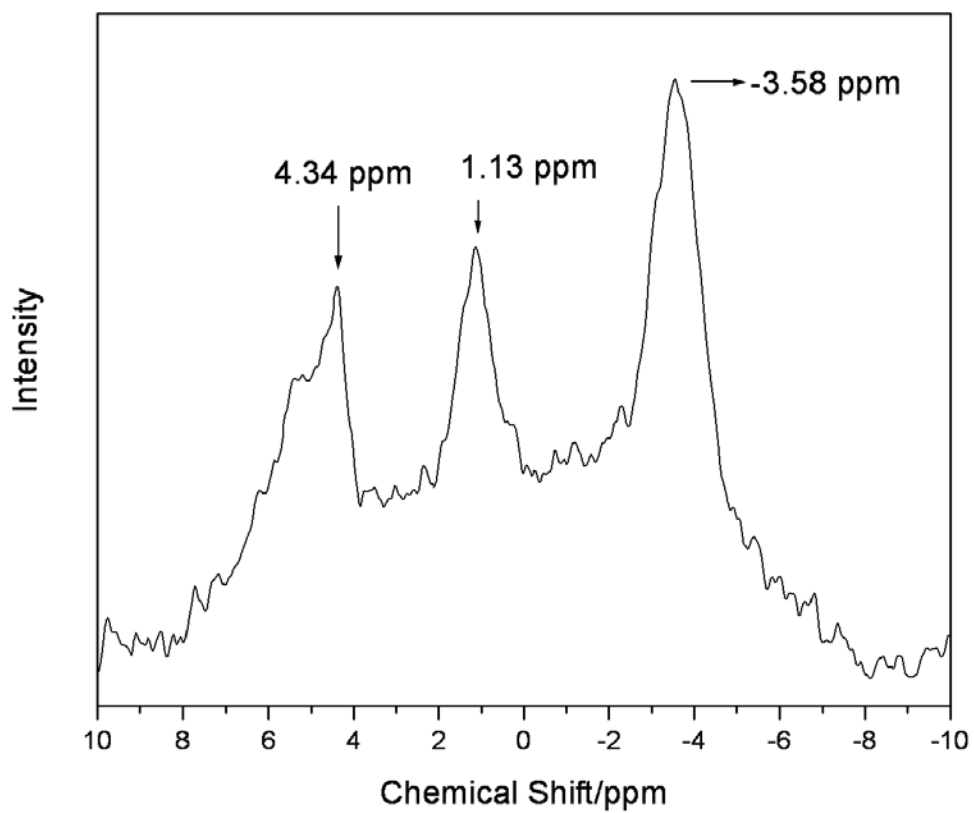


Figure 37. The  $^1\text{H}$  MAS NMR spectra of  $\text{NaH} \cdot \text{Br}$  relative to external TMS showing a  $-3.58$  ppm upfield-shifted peak, a peak at  $1.13$  ppm, and a peak at  $4.3$  ppm assigned to  $\text{H}^- (1/4)$ ,  $\text{H}_2 (1/4)$ , and  $\text{H}_2$ , respectively.



Figures 38A-B.  $\text{NaH} \cdot \text{Cl}$   $^1\text{H}$  MAS NMR spectra relative to external TMS showing the effect of hydrogen addition on the relative intensities of  $\text{H}_2$ ,  $\text{H}_2(1/4)$ , and  $\text{H}^-(1/4)$ . The addition of hydrogen increased the  $\text{H}^-(1/4)$  peak and decreased the  $\text{H}_2(1/4)$  while the  $\text{H}_2$  increased. (A)  $\text{NaH} \cdot \text{Cl}$  synthesized with hydrogen addition showing a  $-4$  ppm upfield-shifted peak assigned to  $\text{H}^-(1/4)$ , a  $1.1$  ppm peak assigned to  $\text{H}_2(1/4)$ , and a dominant  $4$  ppm peak assigned to  $\text{H}_2$ . (B)  $\text{NaH} \cdot \text{Cl}$  synthesized without hydrogen addition showing a  $-4$  ppm upfield-shifted peak assigned to  $\text{H}^-(1/4)$ , a dominant  $1.0$  ppm peak assigned to  $\text{H}_2(1/4)$ , and a small  $4.1$  ppm peak assigned to  $\text{H}_2$ .

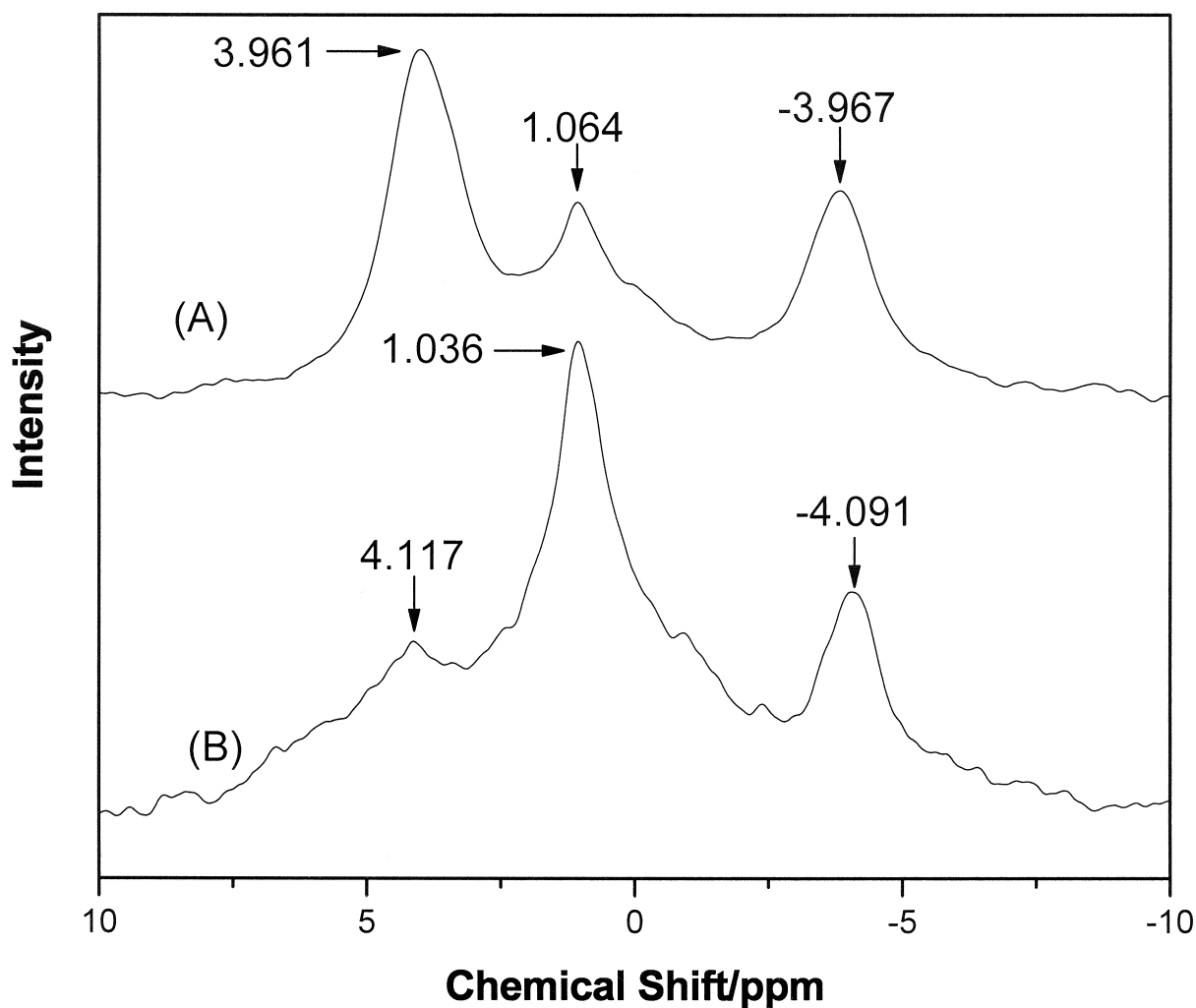


Figure 39. The  $^1\text{H}$  MAS NMR spectrum relative to external TMS of  $\text{NaH} \cdot \text{Cl}$  from reaction of  $\text{Na}$ ,  $\text{NaCl}$ , and the solid H source  $\text{NH}_4\text{Cl}$  showing a  $-3.84$  ppm upfield-shifted peak and a peak at  $1.17$  ppm assigned to  $\text{H}^-(1/4)$  and  $\text{H}_2(1/4)$ , respectively, and the absence of the  $\text{H}_2$  peak.

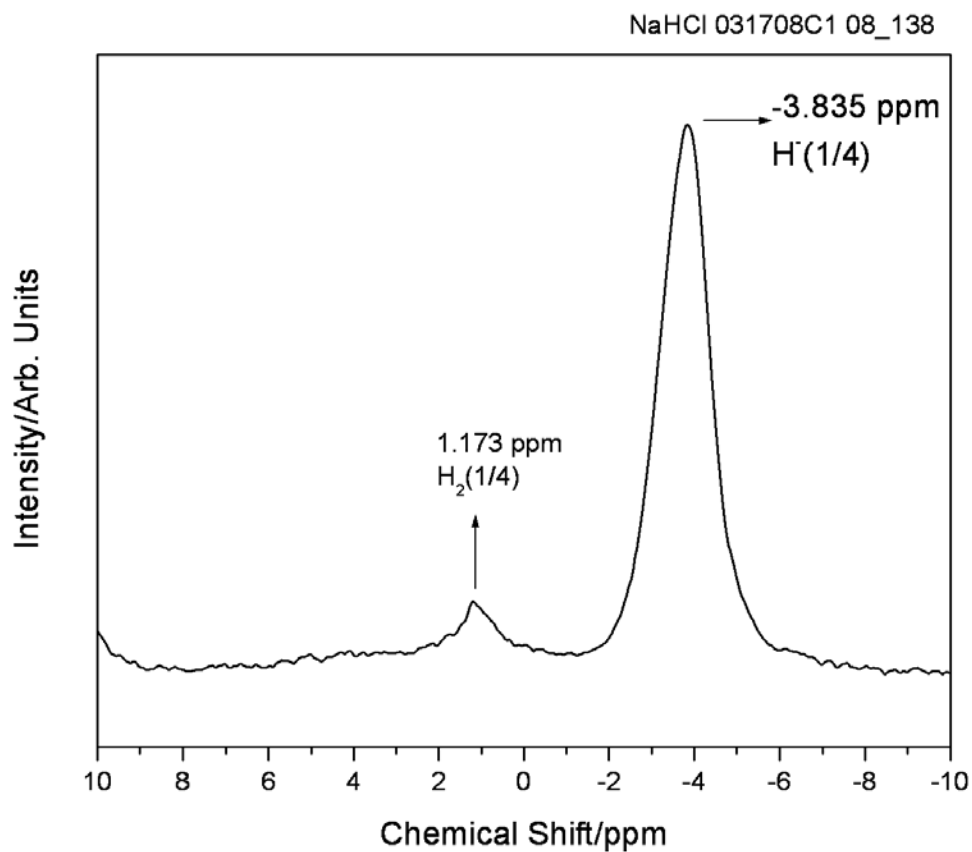


Figure 40. The  $^1\text{H}$  MAS NMR spectrum relative to external TMS of  $\text{NaH} * \text{Br}$  from reaction of  $\text{Na}$ ,  $\text{NaBr}$ , and the solid H source  $\text{NH}_4\text{Br}$  showing a  $-3.56$  ppm upfield-shifted peak and a peak at  $1.23$  ppm assigned to  $\text{H}^- (1/4)$  and  $\text{H}_2 (1/4)$ , respectively, and the absence of the  $\text{H}_2$  peak.

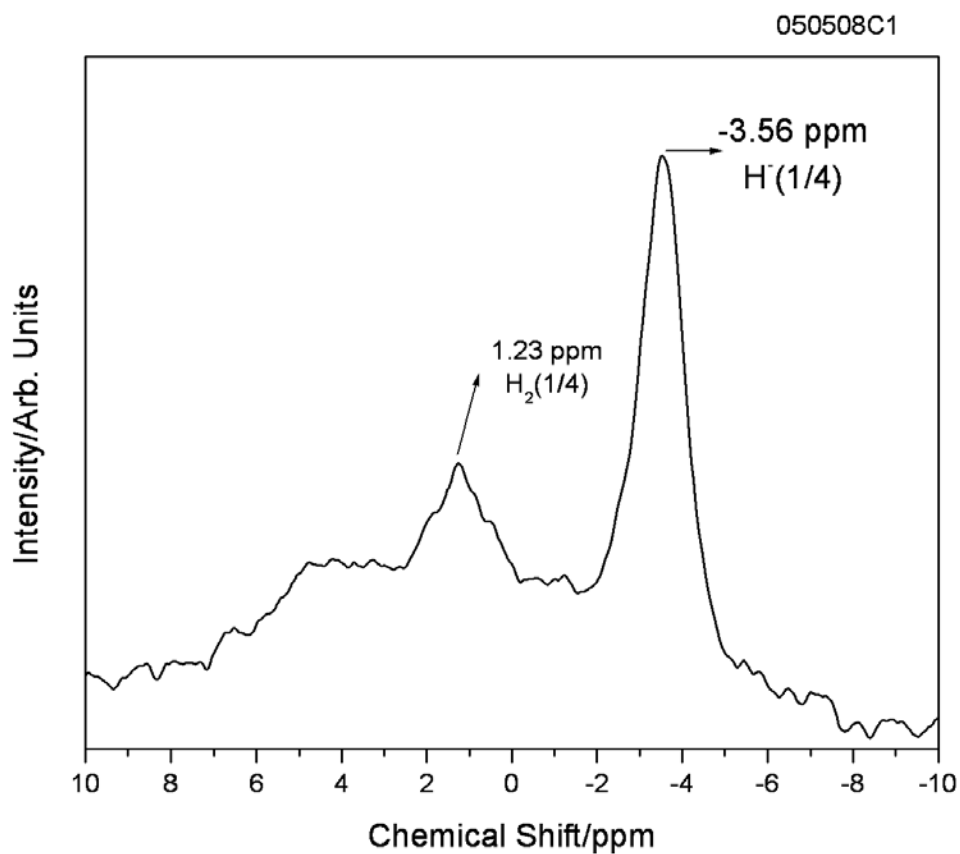


Figure 41. The  $^1\text{H}$  MAS NMR spectrum relative to external TMS of  $\text{NaH} \cdot \text{Cl}$  from reaction of  $\text{NaCl}$  and the solid acid  $\text{KHSO}_4$  as the only source of hydrogen showing both the  $\text{H}^- (1/4)$  peak at  $-3.97$  ppm and an upfield-shifted peak at  $-3.15$  ppm assigned to  $\text{H}^- (1/3)$ . The corresponding  $\text{H}_2 (1/4)$  and  $\text{H}_2 (1/3)$  peaks are shown at  $1.15$  ppm and  $1.7$  ppm, respectively. Both fractional hydrogen states were present and the  $\text{H}_2$  peak was absent at  $4.3$  ppm due to the synthesis of  $\text{NaH} \cdot \text{Cl}$  using a solid acid as the  $\text{H}$  source rather than addition of hydrogen gas and a dissociator. (SB=side band).

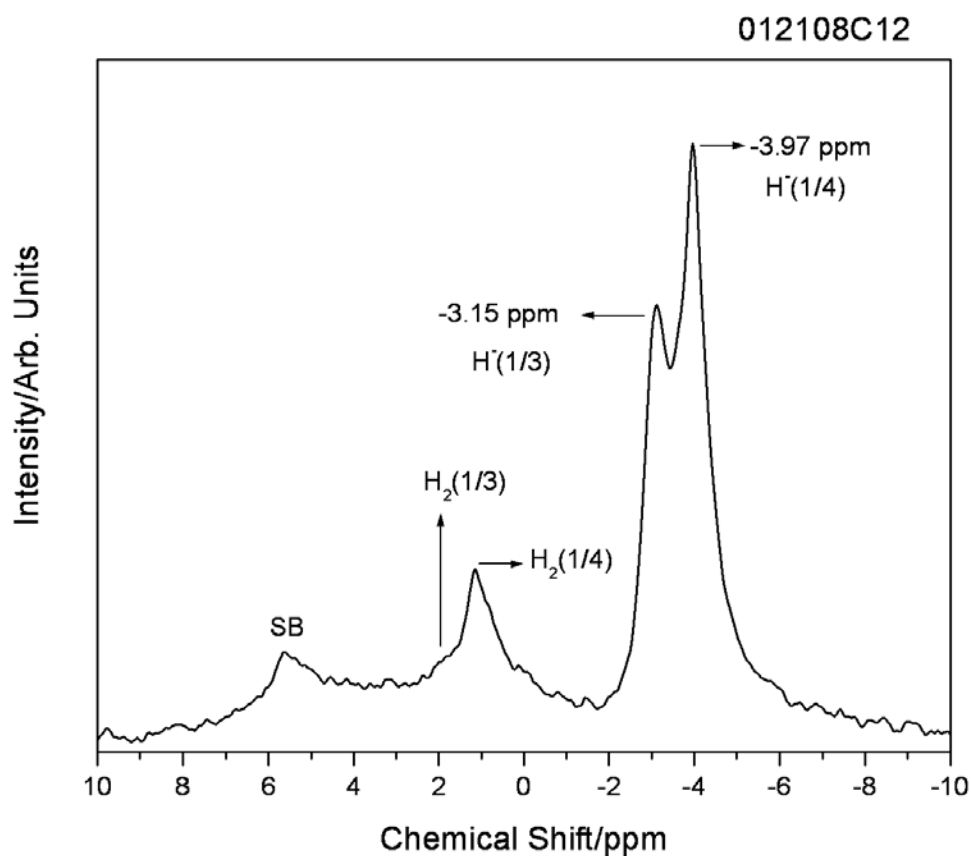


Figure 42. The  $^1\text{H}$  MAS NMR spectrum of  $\text{NaH} * \text{F}$  relative to external TMS showing a matrix-shifted  $\text{H}^- (1/4)$  peak at  $-0.18$  ppm, and unshifted  $\text{H}_2 (1/4)$  and  $\text{H}_2$  peaks at  $1.13$  ppm and  $4.3$  ppm, respectively. The smallest lattice spacing of  $\text{NaF}$  relative to any other sodium halide may give rise to a large matrix effect in  $\text{NaH} * \text{F}$ . (SB=side band).

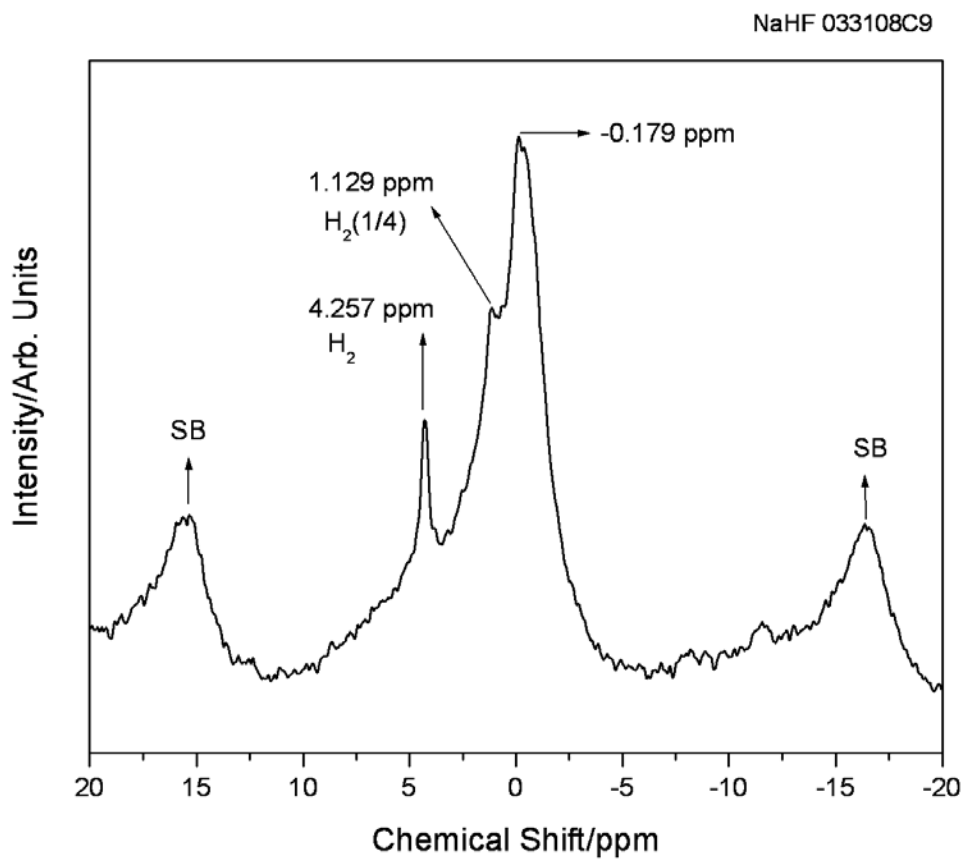


Figure 43.  $^1\text{H}$  solution NMR of  $\text{NaH} * \text{F}$  dissolved in  $\text{DMF-d}_7$  showing isolated  $\text{H}_2(1/4)$  and  $\text{H}^-(1/4)$  at 1.2 ppm and  $-3.86$  ppm, respectively, wherein the absence of any solid matrix effect or the possibility of alternative assignments such as U-centered H or F centers in solid matrix confirm the solid NMR assignments.

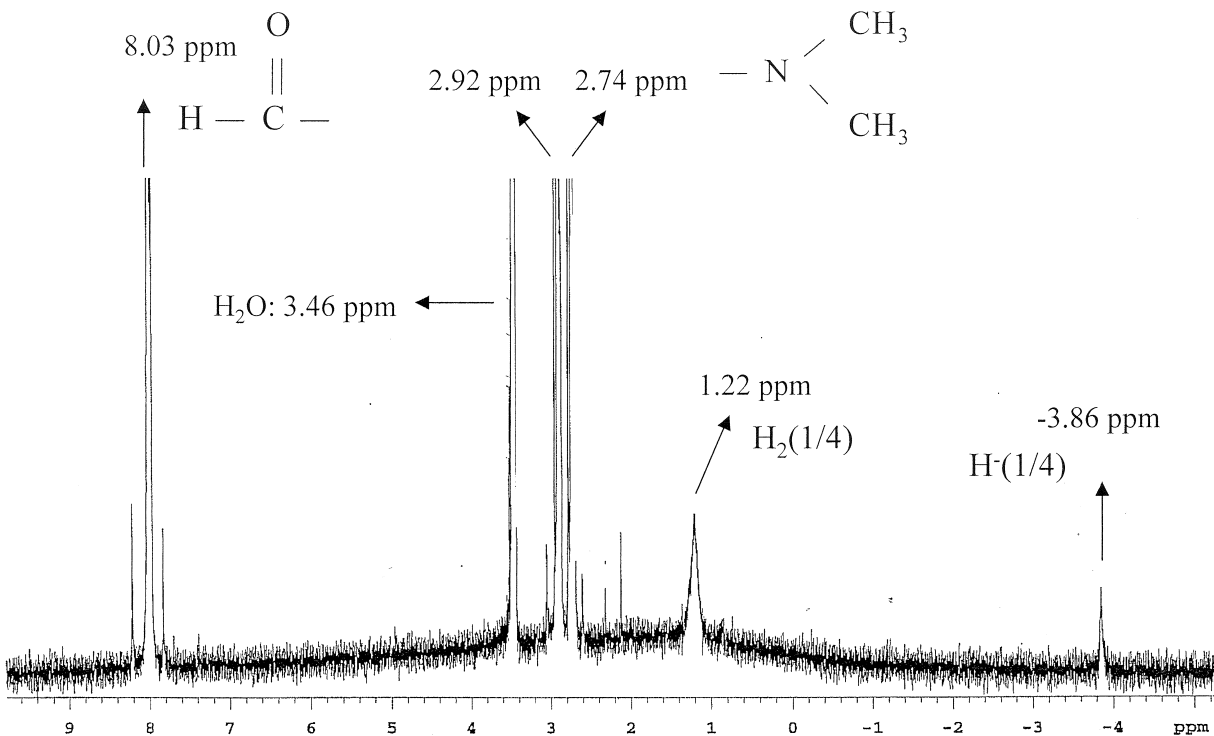


Figure 44.  $^1\text{H}$  solution NMR of  $\text{KH}^*\text{Cl}$  dissolved in  $\text{DMF-d}_7$  showing isolated  $\text{H}_2(1/4)$  and  $\text{H}^-(1/4)$  at 1.2 ppm and  $-3.86$  ppm, respectively, wherein the absence of any solid matrix effect or the possibility of alternative assignments such as U-centered H or F centers in solid matrix confirm the solid NMR assignment of the 1.13 ppm and  $-4.4$  ppm peaks shown in Figure 35A to  $\text{H}_2(1/4)$  and  $\text{H}^-(1/4)$ , respectively.

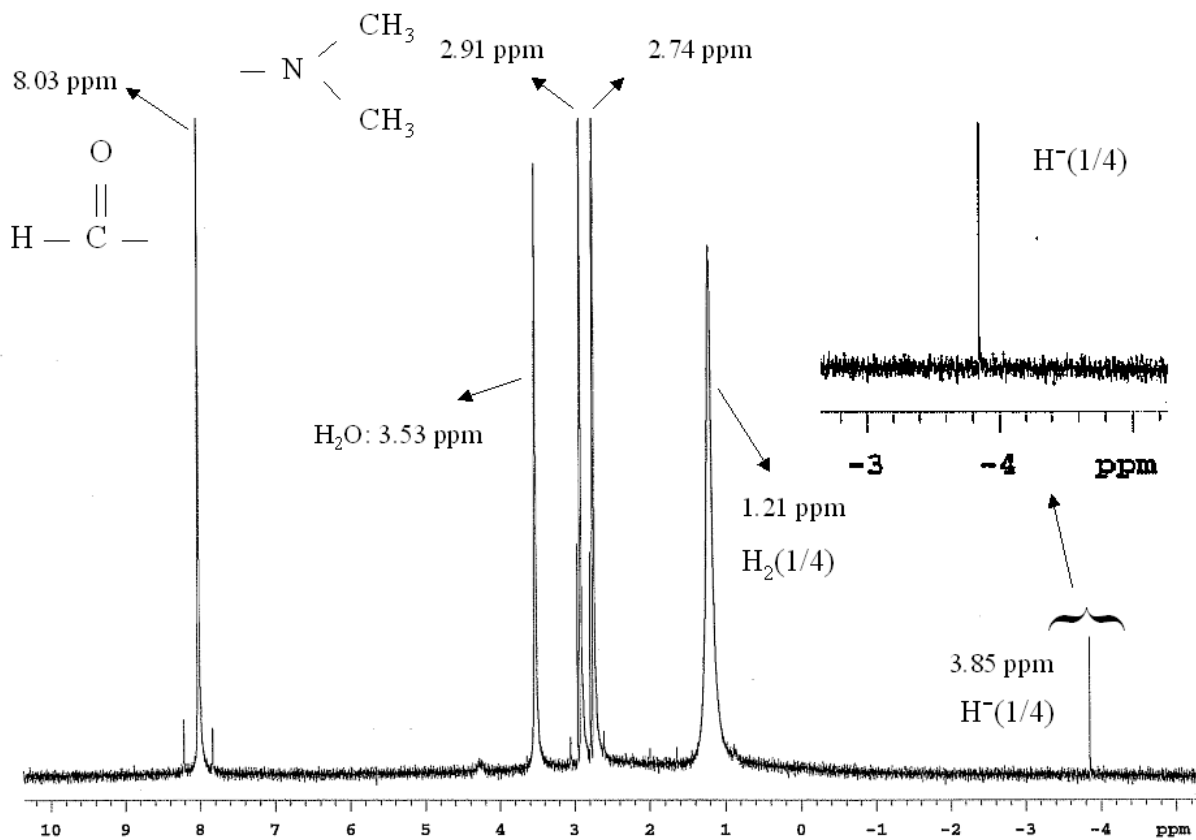


Figure 45.  $^1\text{H}$  solution NMR of  $\text{KH}^*\text{I}$  dissolved to saturation in  $\text{DMF-d}_7$  that showed increasing intensities and slight downfield shifts of the  $\text{H}_2(1/4)$  and  $\text{H}^-(1/4)$  peaks to 1.28 ppm and  $-3.79$  ppm, respectively, as the concentration of  $\text{KH}^*\text{I}$  increased. The concentration-dependent solution matrix effect confirmed the solid matrix effect corresponding to the NMR assignment of  $\text{H}_2(1/4)$  and  $\text{H}^-(1/4)$  to the peaks at 1.13 ppm and  $-2.31$  ppm shown in Figure 35B.

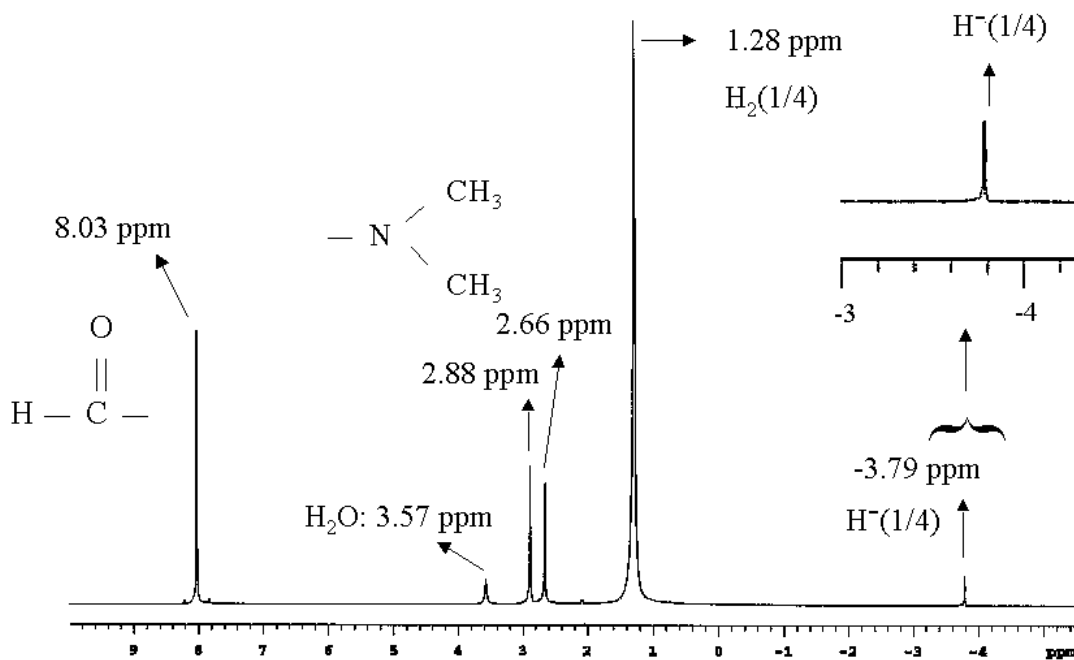
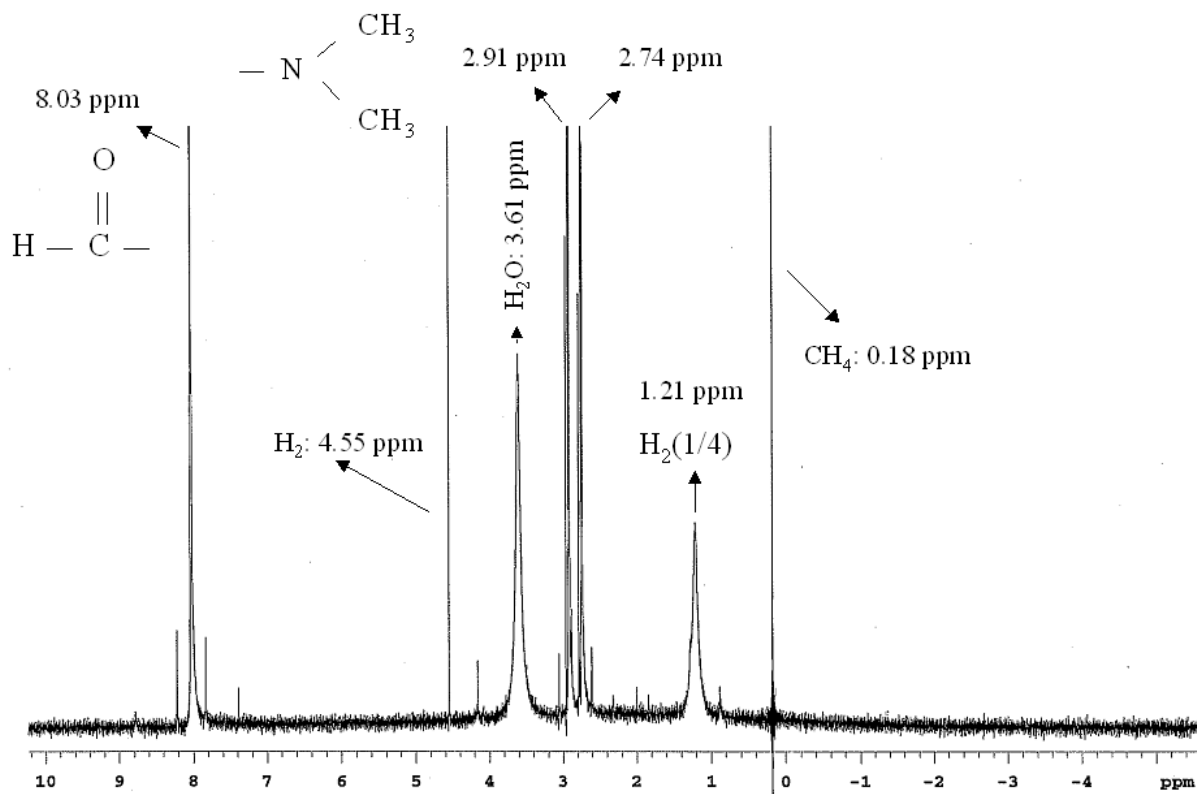


Figure 46.  $^1\text{H}$  solution NMR of  $\text{NaOH}$ -doped R-Ni 2400 product gases collected and dissolved in  $\text{DMF-d}_7$  initially under liquid helium showing the  $\text{H}_2(1/4)$  at 1.2 ppm.



Figures 47A-B. XPS survey spectra ( $E_b = 0 \text{ eV}$  to  $1200 \text{ eV}$ ). (A)  $\text{LiBr}$ . (B)  $\text{LiH}^* \text{Br}$ .

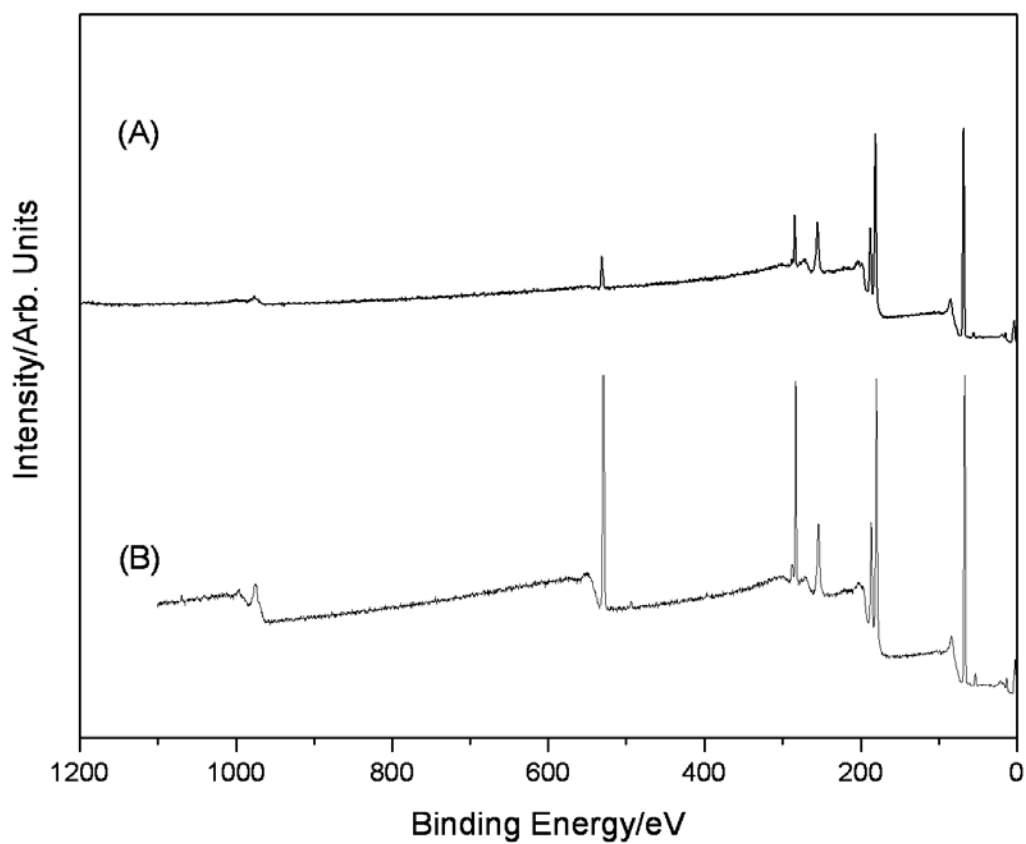


Figure 48. The 0-85 eV binding energy region of a high resolution XPS spectrum of  $LiH^*Br$  and the control  $LiBr$  (dashed). The XPS spectrum of  $LiH^*Br$  differs from that of  $LiBr$  by having additional peaks at 9.5 eV and 12.3 eV that could not be assigned to known elements and do not correspond to any other primary element peak. The peaks match  $H^-(1/4)$  in two different chemical environments.

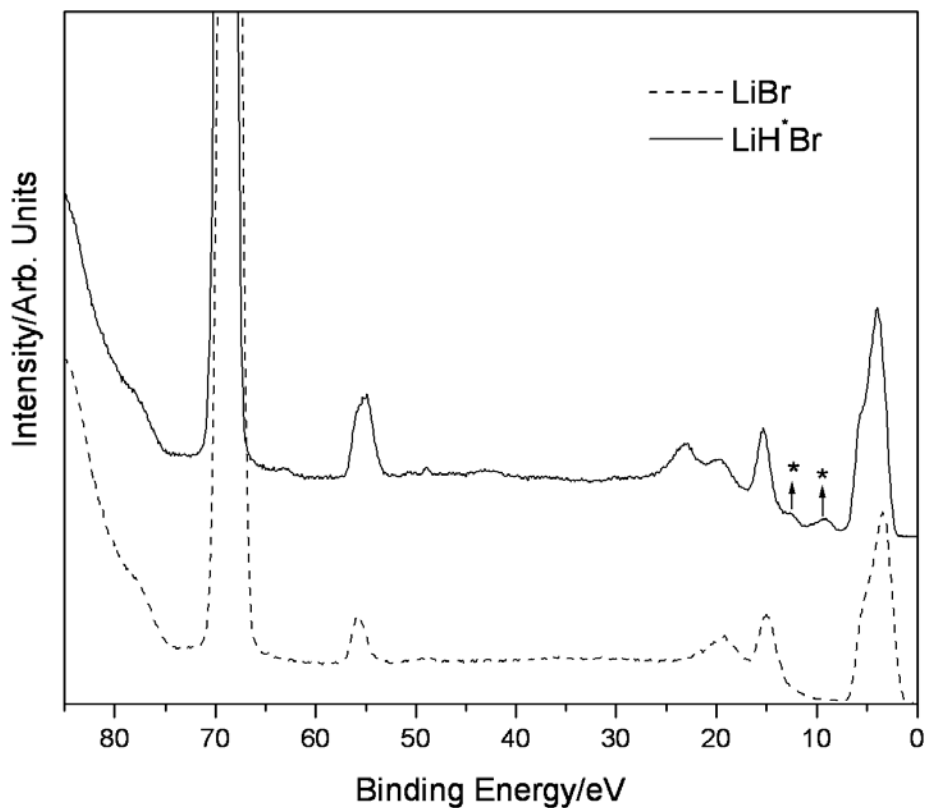
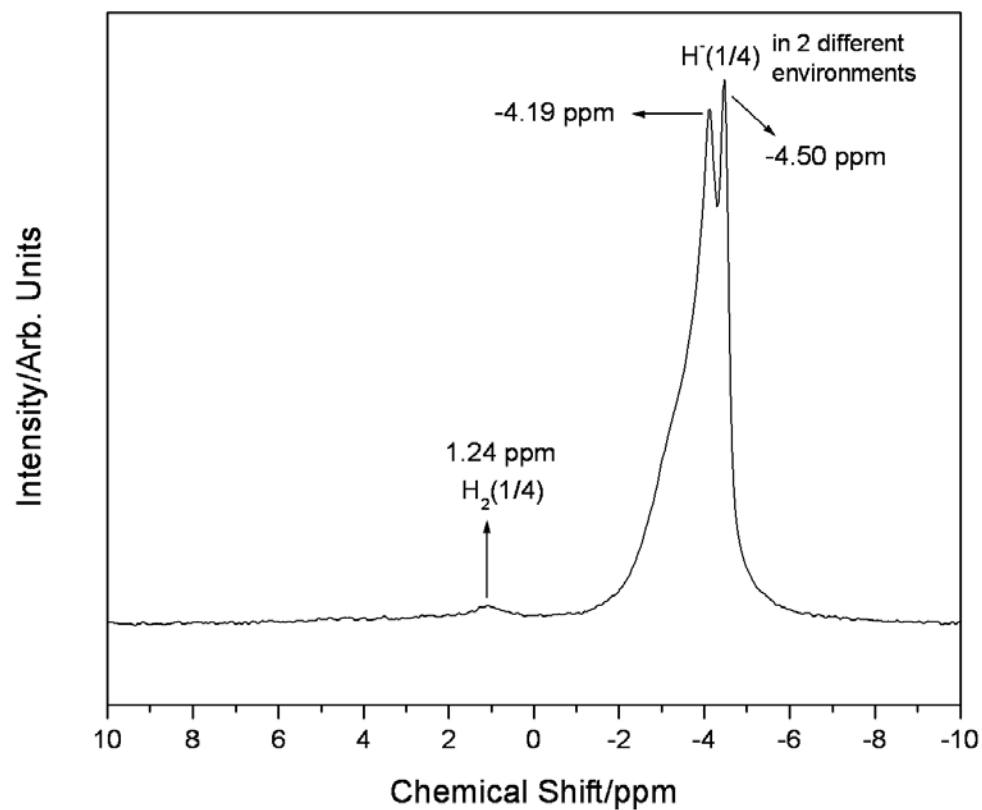


Figure 49.  $^1\text{H}$  MAS NMR spectrum relative to external TMS of  $\text{KH}^*\text{Cl}$  showing  $\text{H}^- (1/4)$  having two peaks at  $-4.19$  ppm and  $-4.50$  ppm corresponding to two different chemical environments compared to the very sharp  $-4.46$  ppm upfield-shifted peak corresponding to an environment that is essentially that of a free ion shown in Figure 35A.



Figures 50A-B. XPS survey spectra ( $E_b = 0$  eV to 1200 eV). (A)  $NaBr$ . (B)  $NaH * Br$ .

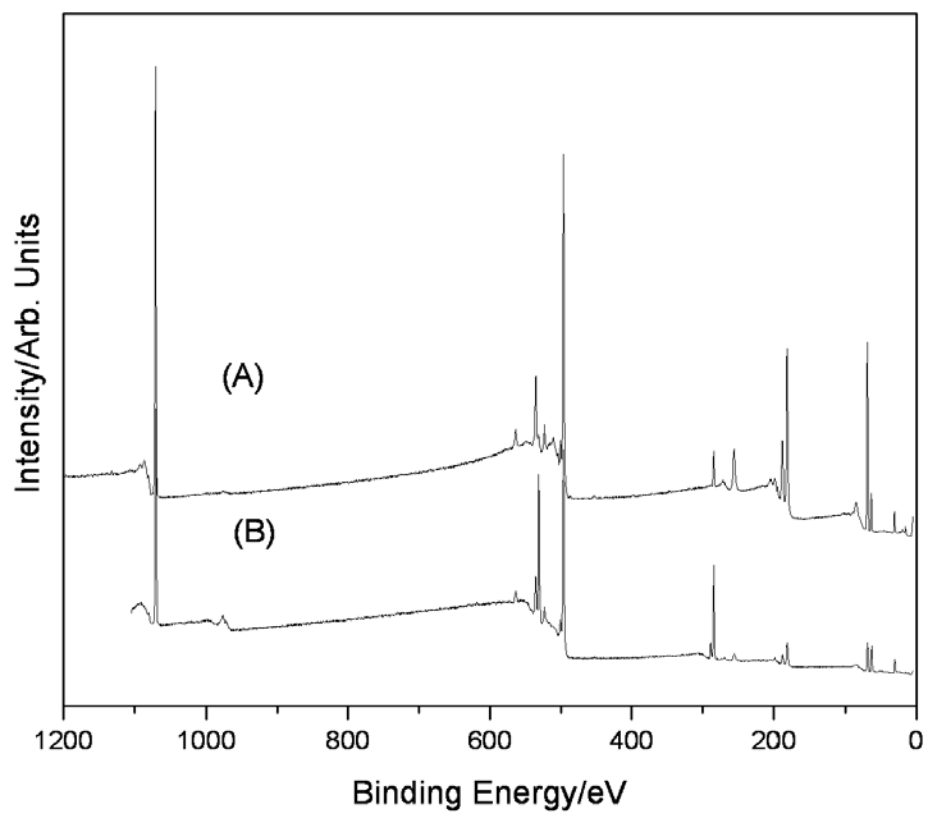
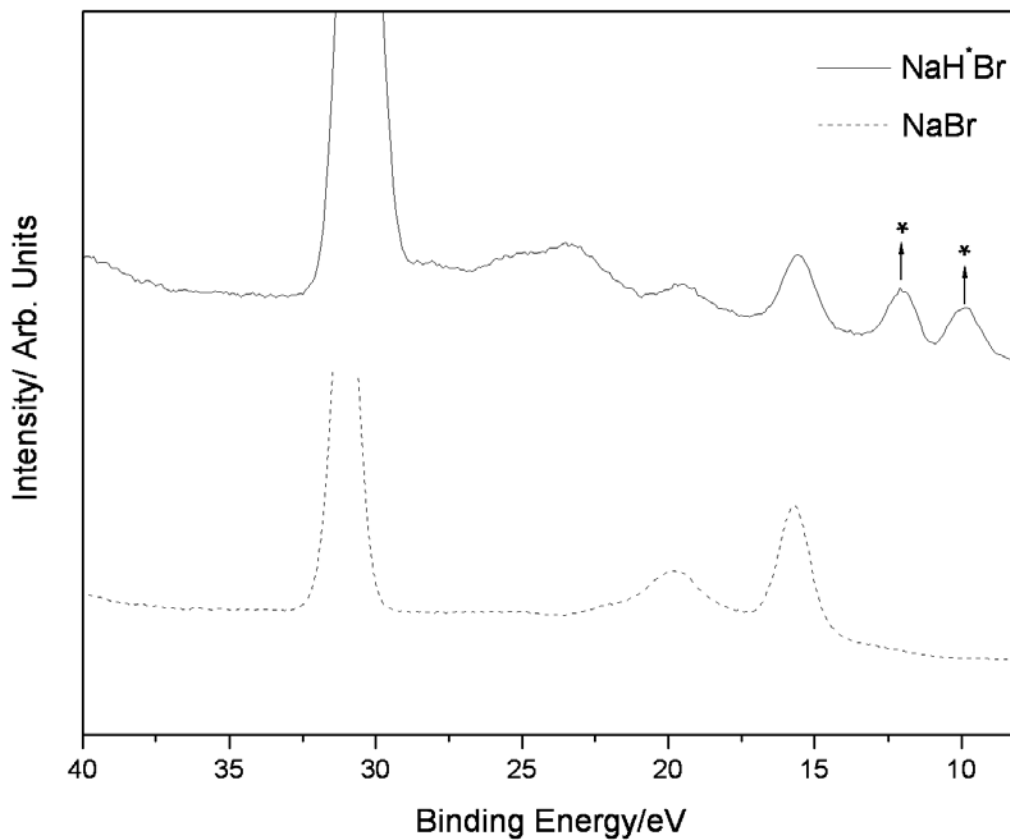
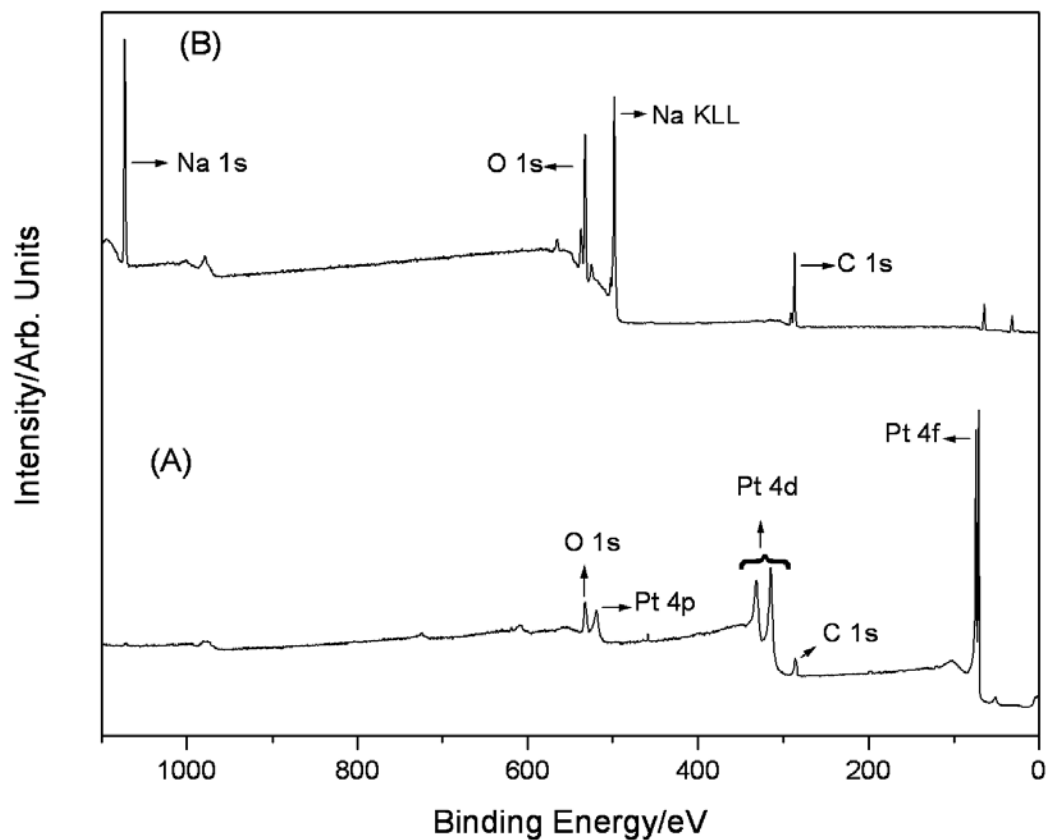


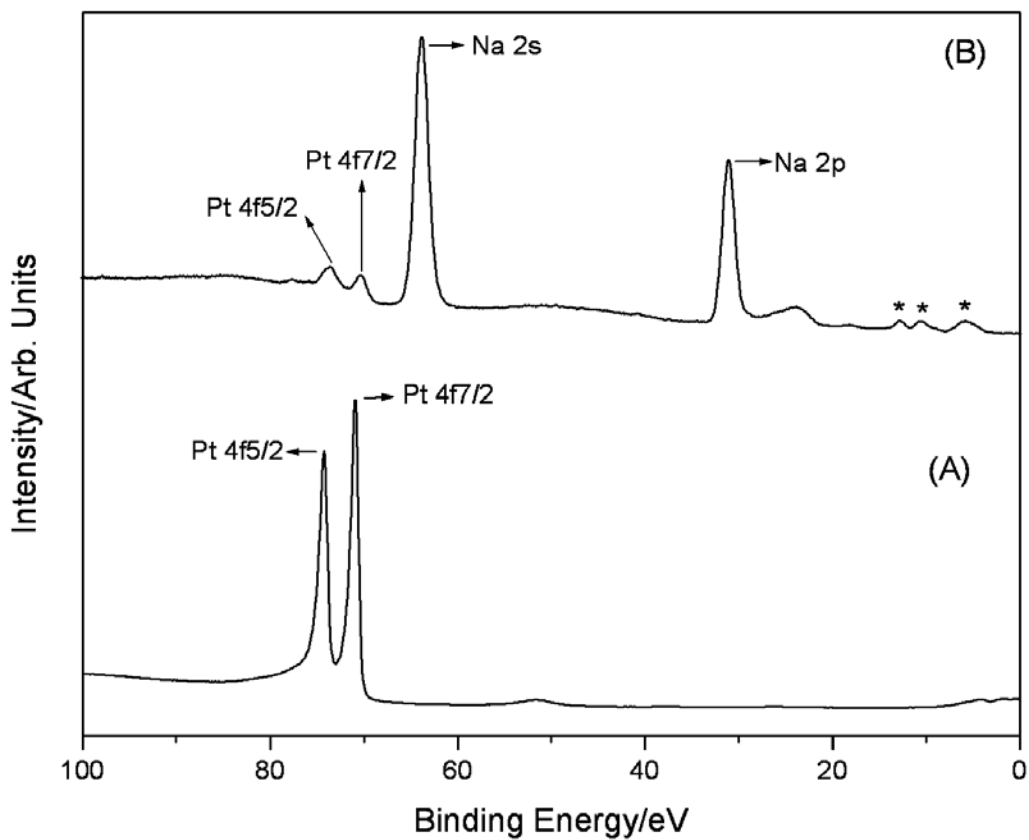
Figure 51. The 0-40 eV binding energy region of a high resolution XPS spectrum of  $NaH \cdot Br$  and the control  $NaBr$  (dashed). The XPS spectrum of  $NaH \cdot Br$  differs from that of  $NaBr$  by having additional peaks at 9.5 eV and 12.3 eV that could not be assigned to known elements and do not correspond to any other primary element peak. The peaks match  $H^-(1/4)$  in two different chemical environments.



Figures 52A-B. XPS survey spectra ( $E_b = 0$  eV to 1200 eV). (A) *Pt/Ti*. (B) *NaH*\*-coated *Pt/Ti* following the production of 15 kJ of excess heat.



Figures 53A-B. High resolution XPS spectra ( $E_b = 0$  eV to 100 eV). (A) *Pt/Ti*. (B) *NaH*\*-coated *Pt/Ti* following the production of 15 kJ of excess heat. The *Pt* 4*f*<sub>7/2</sub>, *Pt* 4*f*<sub>5/2</sub>, and *O* 2*s* peaks were observed at 70.7 eV, 74 eV, and 23 eV, respectively. The *Na* 2*p* and *Na* 2*s* peaks were observed at 31 eV and 64 eV on *NaH*\*-coated *Pt/Ti*, and a valence band was only observed for *Pt/Ti*.



Figures 54A-B. High resolution XPS spectra ( $E_b = 0 \text{ eV}$  to  $50 \text{ eV}$ ). (A) *Pt/Ti*. (B) *NaH*\*-coated *Pt/Ti* following the production of 15 kJ of excess heat. The XPS spectrum of *NaH*\*-coated *Pt/Ti* differs from that of *Pt/Ti* by having additional peaks at 6 eV, 10.8 eV, and 12.8 eV that could not be assigned to known elements and do not correspond to any other primary element peak. The 10.8 eV, and 12.8 eV peaks match  $H^-(1/4)$  in two different chemical environments, and the 6 eV peak matched and was assigned to  $H^-(1/3)$ . Thus, both fractional hydrogen states, 1/3 and 1/4, were present as predicted by Eq. (27).

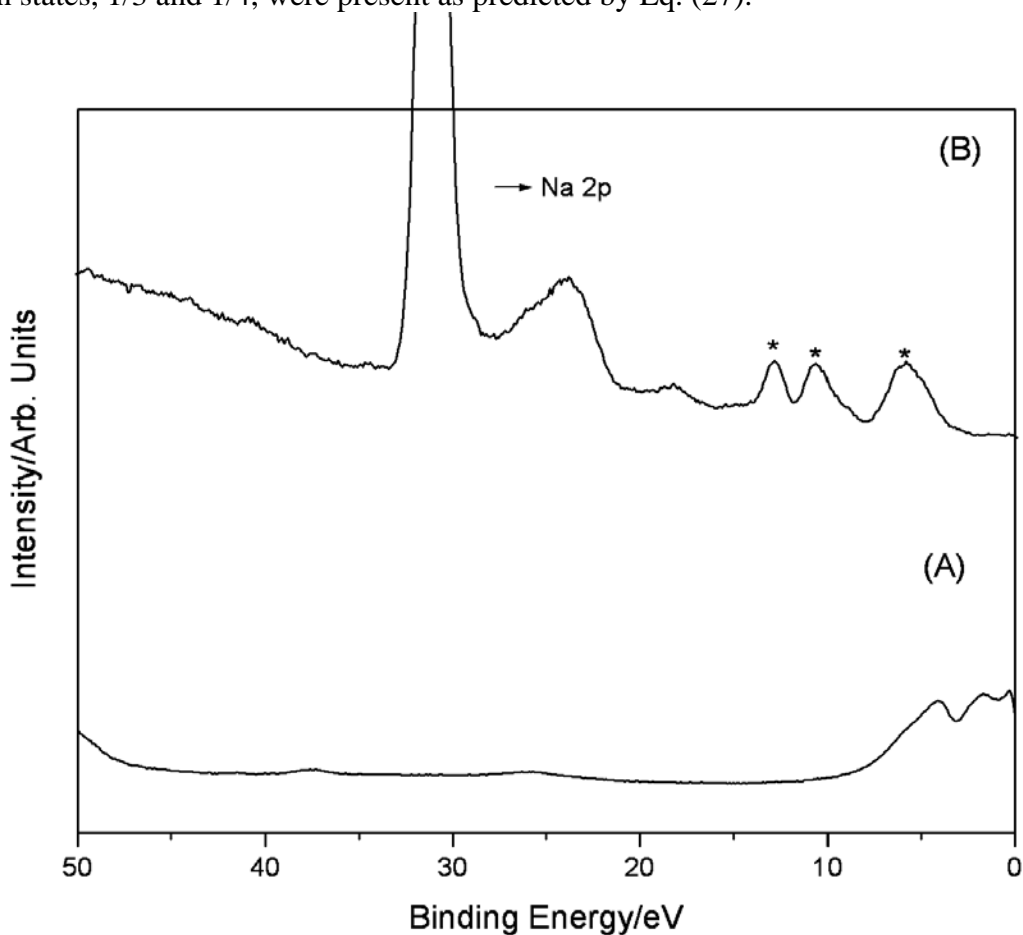


Figure 55. XPS survey spectrum ( $E_b = 0 \text{ eV}$  to  $120 \text{ eV}$ ) of  $\text{NaH}^*$ -coated  $\text{Si}$  with the primary-element peaks identified.

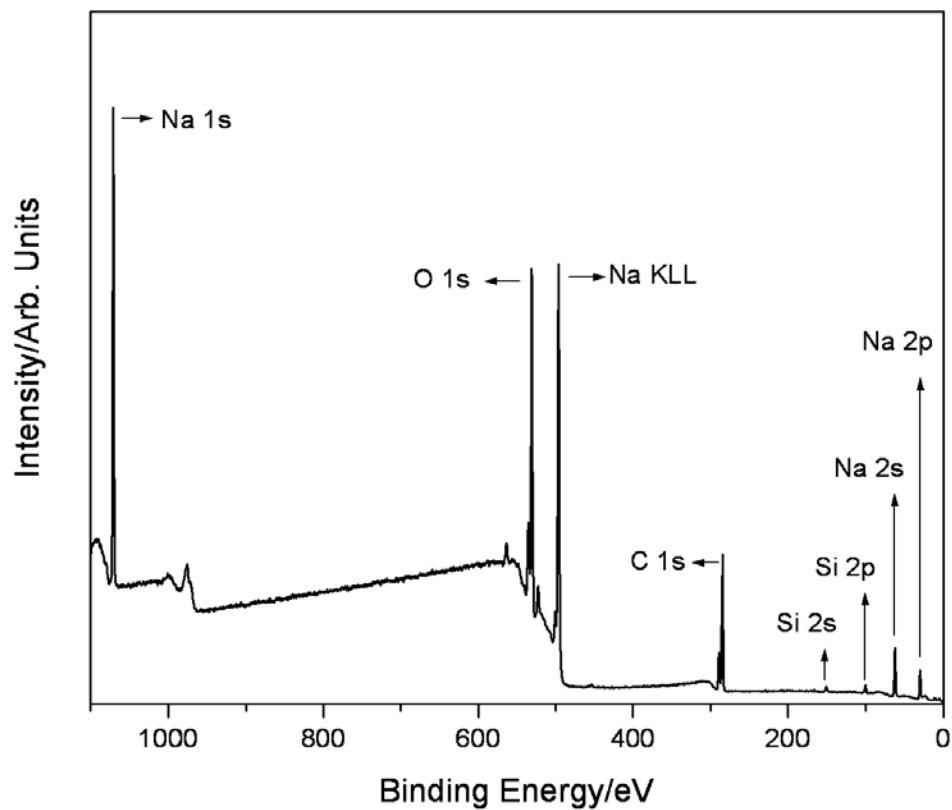
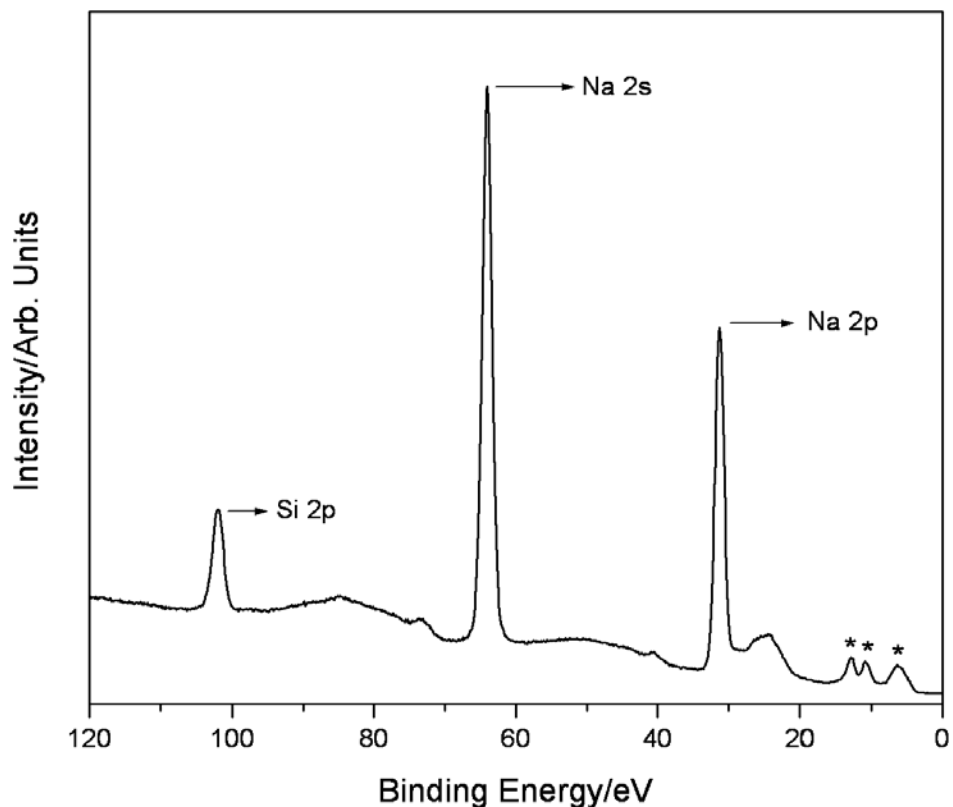


Figure 56. High resolution XPS spectrum ( $E_b = 0 \text{ eV}$  to  $120 \text{ eV}$ ) of  $\text{NaH}^*$ -coated  $\text{Si}$  having peaks at  $6 \text{ eV}$ ,  $10.8 \text{ eV}$ , and  $12.8 \text{ eV}$  that could not be assigned to known elements and do not correspond to any other primary element peak. The  $10.8 \text{ eV}$ , and  $12.8 \text{ eV}$  peaks match  $\text{H}^- (1/4)$  in two different chemical environments, and the  $6 \text{ eV}$  peak matched and was assigned to  $\text{H}^- (1/3)$ . Thus, both fractional hydrogen states,  $1/3$  and  $1/4$ , were present as predicted by Eq. (27) matching the results of  $\text{NaH}^*$ -coated  $\text{Pt/Ti}$  shown in Figure 53B.



Figures 57A-B. High resolution ( $0.5\text{ cm}^{-1}$ ) FTIR spectra ( $490\text{-}4000\text{ cm}^{-1}$ ). (A) *LiBr*. (B) *LiH \* Br* sample having a NMR peak assigned to  $H^-(1/4)$  that was heated to  $>600^\circ\text{C}$  under dynamic vacuum that retained the  $-2.5\text{ ppm}$  NMR peak. The amide peaks at  $3314$ ,  $3259$ ,  $2079$ (broad),  $1567$ , and  $1541\text{ cm}^{-1}$  and the imide peaks at  $3172$  (broad),  $1953$ , and  $1578\text{ cm}^{-1}$  were eliminated; thus, they were not the source of the  $-2.5\text{ ppm}$  NMR peak that remained. The  $-2.5\text{ ppm}$  peak in  $^1\text{H}$  NMR spectrum was assigned to the  $H^-(1/4)$  ion. In addition, the  $1989\text{ cm}^{-1}$  FTIR peak could not be assigned to any know compound, but matched the predicted frequency of para  $H_2(1/4)$ .

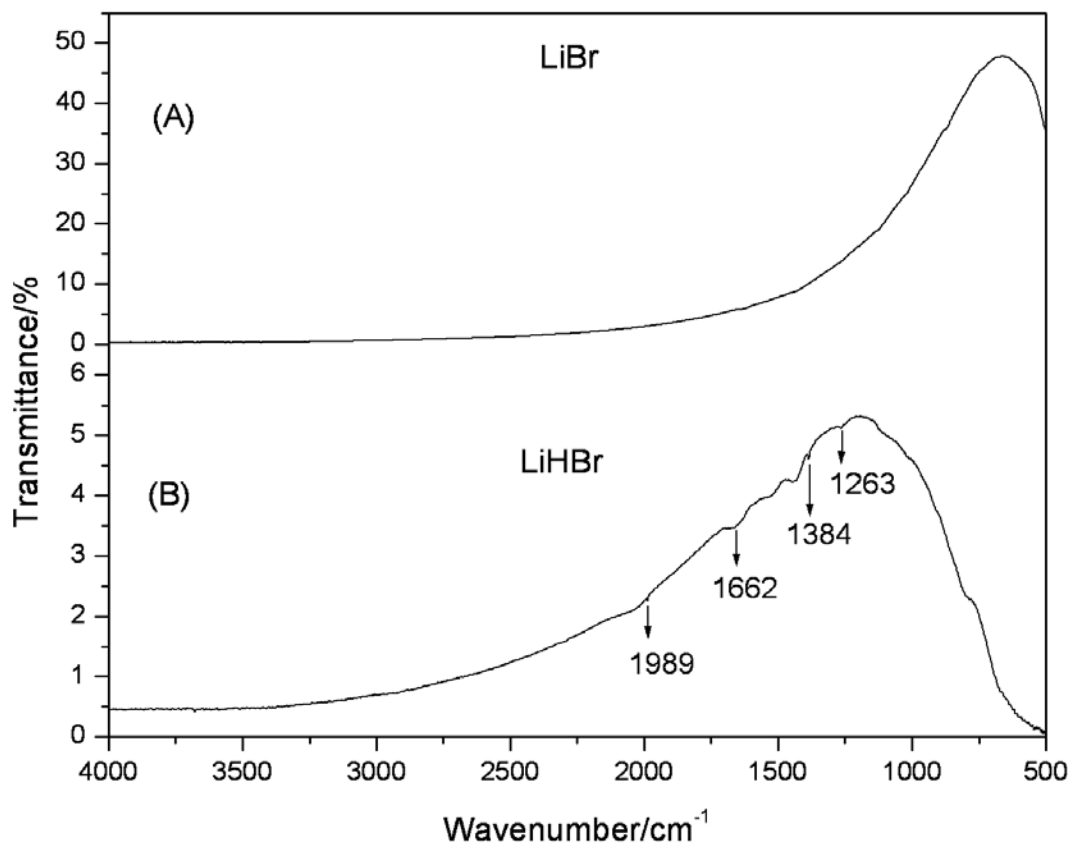


Figure 58. The  $^1\text{H}$  MAS NMR spectra relative to external TMS of  $\text{NaCl}$ ,  $\text{KCl}$ , and  $\text{CsCl}$  showing the expected trend of increasing intensity of  $H_2(1/4)$  at 1.1 ppm relative to the  $H_2$  at 4.3 ppm down the column of the Group I elements.

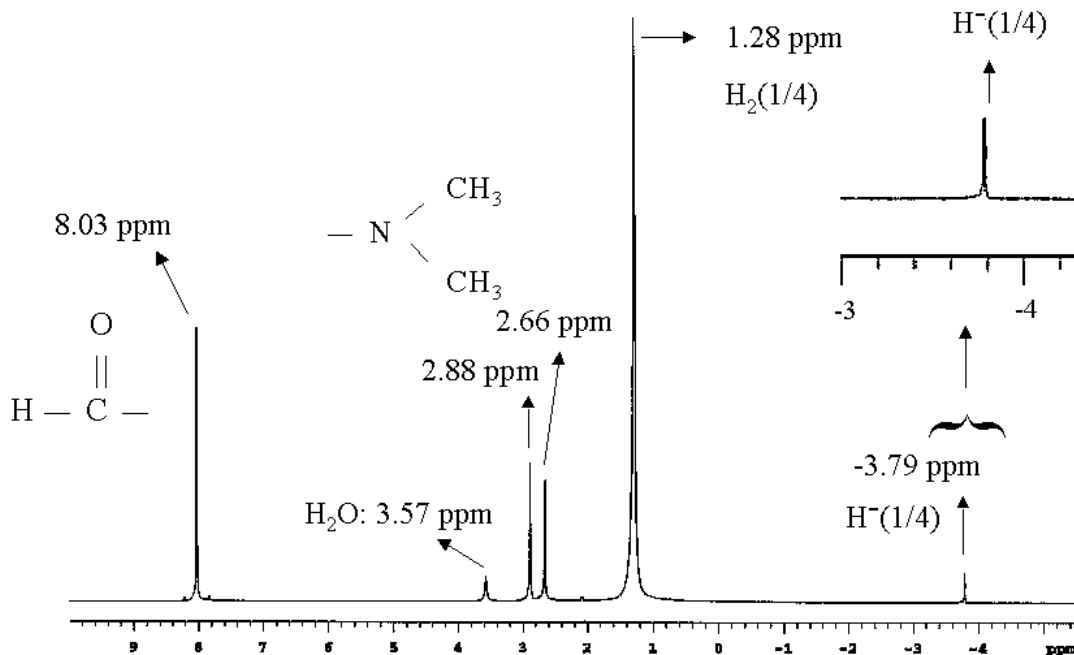


Figure 59. The 180-350 nm spectra of electron-beam excited  $NaCl$ ,  $KCl$ , and  $CsCl$  crystals having trapped  $H_2(1/4)$ . For each, a series of evenly spaced lines was observed in the 220-300 nm region that matched the spacing and intensity profile of the P branch of  $H_2(1/4)$ . The expected trend of increasing intensity of  $H_2(1/4)$  down the column of the Group I elements was observed that matched the intensity trend of the  $H_2(1/4)$  NMR peak at 1.1 ppm relative to the  $H_2$  peak at 4.3 ppm (Figure 57). The band shifted to longer wavelength down the column of the Group I elements due to the vibrational matrix interaction.

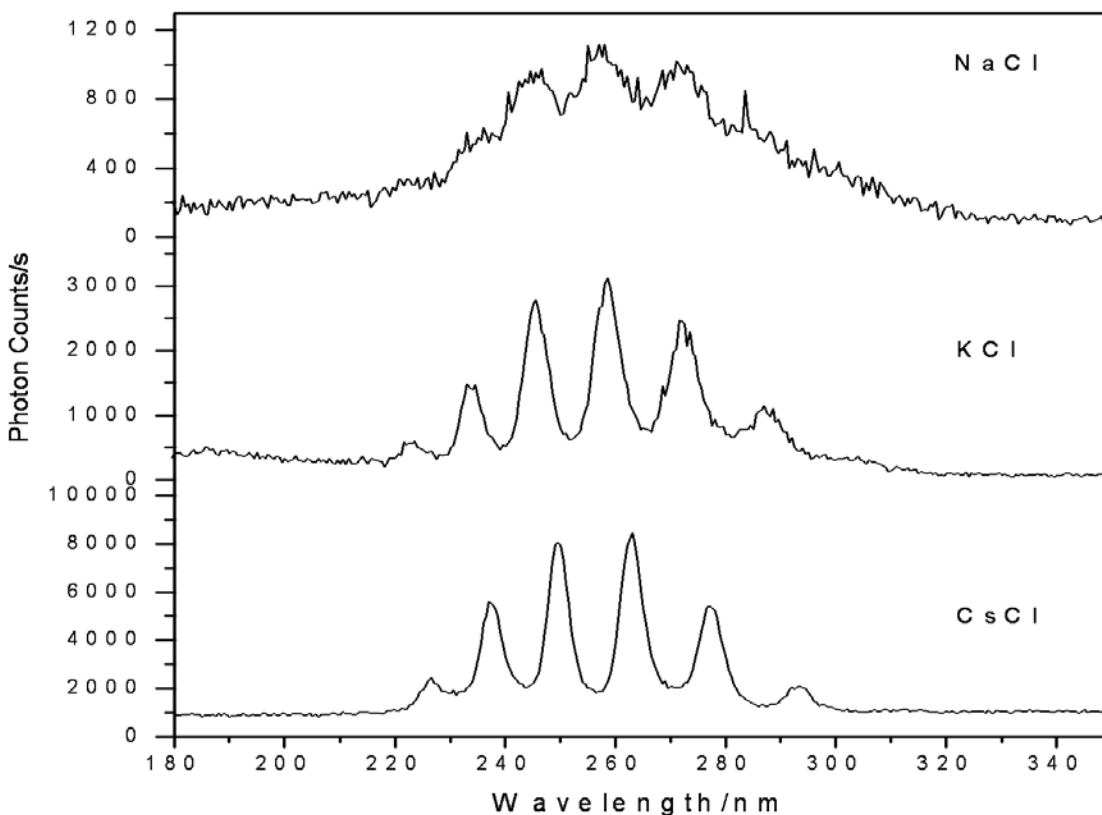


Figure 60. The 150-350 nm spectrum of electron-beam excited  $CsCl$  crystals having trapped  $H_2(1/4)$ . A series of evenly spaced lines was observed in the 220-300 nm region that matched the spacing and intensity profile of the P branch of  $H_2(1/4)$ .

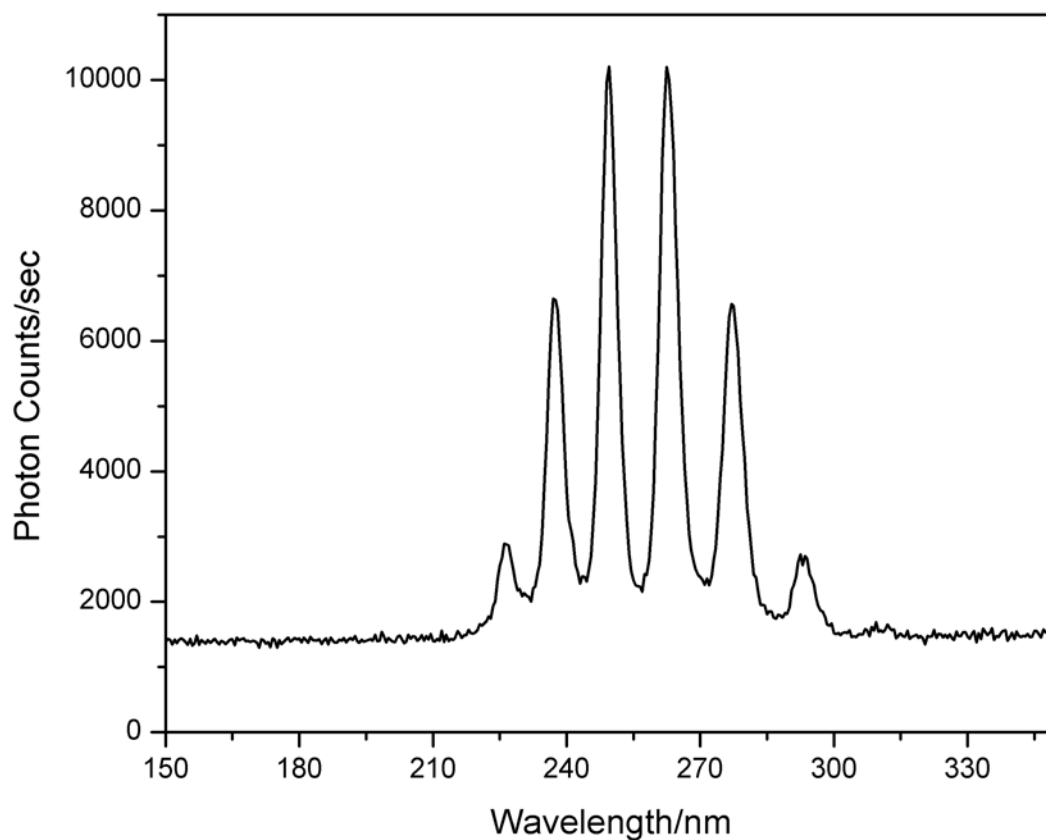


Figure 61. The 100-550 nm spectrum of an electron-beam excited silicon wafer coated with  $NaH \cdot Cl$  having trapped  $H_2(1/4)$ . A series of evenly spaced lines was observed in the 220-300 nm region that matched the spacing and intensity profile of the P branch of  $H_2(1/4)$ .

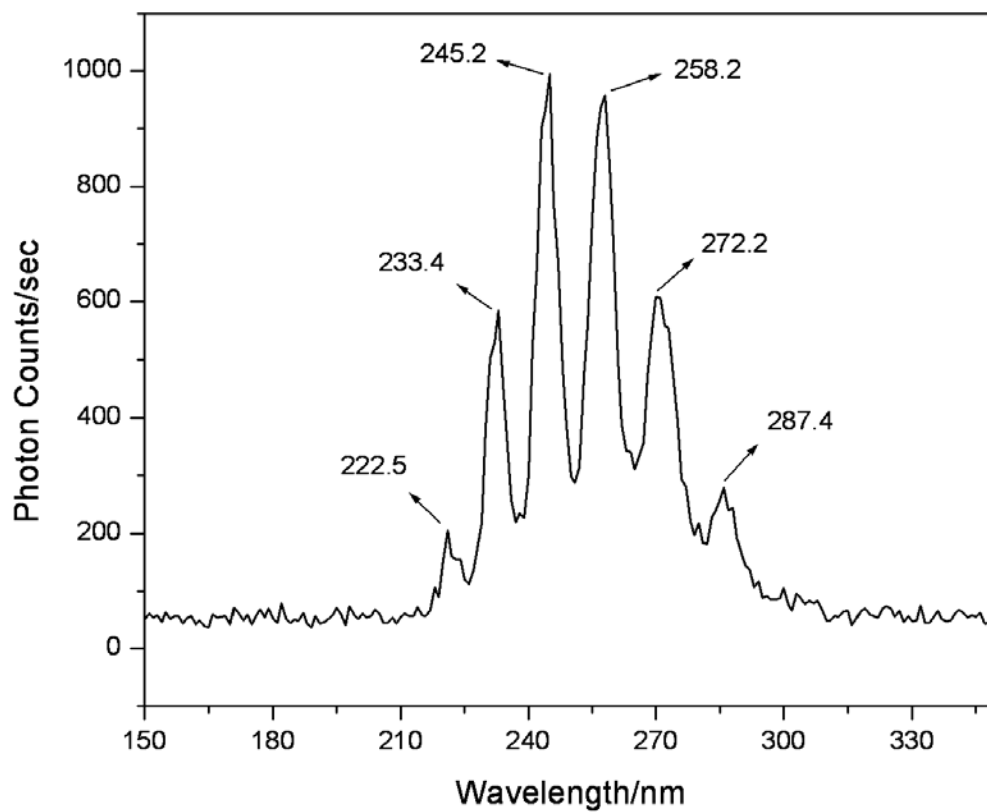


Figure 62. The 100-560 nm spectrum of 750 Torr, 12.5 keV-electron-beam-maintained plasma of argon containing about 1% hydrogen. The slope of the linear curve fit is 0.24 eV with an intercept of 8.24 eV which matches Eqs. (13) and (14) very well for  $p = 4$ . Single peaks were observed to the 3<sup>rd</sup> order.

